Summer 8-4-2011

Synthesis and Characterization of Nanostructures in Porous Anodic Aluminum Oxide Templates

Jin-Hee Lim
University of New Orleans, jlim1@my.uno.edu

Synthesis and Characterization of Nanostructures in Porous Anodic Aluminum Oxide Templates

A Dissertation

Submitted to the Graduate Faculty of the
University of New Orleans
in partial fulfillment of the
requirements for the degree of

Doctor of Philosophy
in
The Department of Chemistry

by

Jin-Hee Lim

B.S. Kangnung National University, 2004
M.S. Kangnung National University, 2006
M.S. University of New Orleans, 2009

August, 2011

To Hyun-Ki Kang

Acknowledgments

I would like to express my deepest appreciation and gratitude to my advisor, Professor John B. Wiley, for providing invaluable guidance and for constantly supporting me for five years. The present research was not complete without his encouragement and helpful advice. I also would like to thank my dissertation committee members, Dr. Weilie Zhou, Dr. Leszek Malkinski, Dr. Ferdinand Poudeu, Dr. Matthew Tarr, and Dr. Ananthakrishnan Sankaranarayanan, for their helpful suggestion and discussion. I especially thank to Dr. Weilie Zhou for providing me with challenges and his help to learn microscopy, and also thank to Dr. Leonard Spinu in Department of Physics for his support and for giving me a chance to learn magnetism and magnetic materials.

I am deeply grateful to advanced materials research institute (AMRI) members and Department of Physics, Dr. Cosmin Radu, Dr. Huy Pham, Dr. Seonggi Min, Ovidiu Trusca for conducting magnetic measurements, Dr. Baobao Cao, Dr. Jiajun Chen, Kai Wang, Renghai Long for helping me microscopy operation and analysis. I also thank all faculty members in AMRI and Department of Chemistry for making possible teaching and research assistantships.

To all our group members, past and present, thanks you for important suggestions, assistance, encouragement of my studies, wonderful friendship, and keeping a nice place to work. Dr. Feng Li, Dr. Xiequn Zhang, Dr. Jonglak Choi, Dr. Kulugammana G Ranmohotti, Dr. Girija S. Chaubey, Jianxia Zhang, Yuan Yao, Debasish Mohanty, Jagnyaseni Tripathy, Elisha Josepha, Dariush Asadi, and Lea Gustin.

I would like to thank Dr. Jin-Seung Jung in Gangneung Wonju National University, Korea, for stimulating my research interests in materials chemistry and encouraging me to finish this work.

I also express my indebtedness to all my friends and church members for their encouragement to complete this work and for their help to accommodate myself in a new environment. Especially, I would like to thank Dr. Heeje Lee and Dr. Haewon Lee for heart warming encouragements in my study.

I would also like to appreciate to my family for their love and support. There are no adequate acknowledgments to express the deepest thanks. Without their support and love I would not have accomplished this work. Finally I am thankful to my husband Hyunki Kang. His continuous encouragement and supports are leading me to conduct all my work.

Support from the National Science Foundation through NSF-0403673 and NSF-1028547 is gratefully acknowledged.

Table of Contents

List of Figures vii
List of Tables xv
Abbreviations xvi
Abstract xviii
Chapter 1 Introduction and Research Background 1
1.1 Nanotechnology 1
1.2 Template-based Electrodeposition 2
1.2.1 Anodic Aluminum Oxide Templates 2
1.2.2 Electrodeposited Nanomaterials 4
1.2.3 Magnetism 6
1.2.4 Hysteresis Loop 8
1.3 References 9
Chapter 2 Synthesis of Porous Anodic Aluminum Oxide (AAO) 12
2.1 Introduction 12
2.2 Experimental 14
2.2.1 Anodization of Conventional AAO Templates 14
2.2.2 Anodization of Modified AAO Templates 16
2.2.3 Microscopic Characterization of AAO Templates 18
2.3 Results and Discussion 18
2.3.1 Conventional AAO Templates 18
2.3.2 Modified AAO Templates 28
2.3.2.1 Increasing voltages: Selectively opened and enlarged pore structures 28
2.3.2.2 Decreasing voltages: Arch-shaped and branched pore structures 32
2.4 Conclusions 41
2.5 References 43
Chapter 3 Magnetic Nanostructures in Conventional AAO Templates 45
3.1 Introduction 45
3.2 Experimental 46
3.2.1 Synthesis of AAO Templates 46
3.2.2 Synthesis of Fe Nanostructures 46
3.2.3 Characterization 47
3.3 Results and Discussion 48
3.4 Conclusions 53
3.5 References 53
Chapter 4 Co and Ni Nanowires in Mild-Hard AAO Templates for Studying Magnetic Interactions between Nanowires 55
4.1 Introduction 55
4.2 Experimental 56
4.2.1 Preparation of Conventional Mild AAO and Mild-Hard AAO Templates 56
4.2.2 Synthesis of Co and Ni Nanowires 57
4.2.3 Characterization 58

4.3 Results 59
4.4 Discussion 68
4.5 Conclusions 71
4.6 References 72
Chapter 5 Electrodeposited Iron Oxide Nanotubes in Porous Alumina Templates 73
5.1 Introduction 73
5.2 Experimental 74
5.2.1 Synthesis of Iron Oxide Nanotubes 74
5.2.2 Characterization 75
5.3 Results 75
5.3.1 α-Fe_2O_3 nanotubes 76
5.3.2 Fe_3O_4 nanotubes 82
5.4 Discussion 87
5.5 Conclusions 89
5.6 References 90
Chapter 6 Metal Nanowire Arrays in Pre-patterned AAO Templates 92
6.1 Introduction 92
6.2 Experimental 93
6.2.1 Nanosphere Lithography 94
6.2.2 E-beam Lithography 95
6.2.3 Characterization 95
6.3 Results and Discussion 96
6.3.1 Patterned Nanowire Arrays by Nanosphere Lithography 96
6.3.2 Patterned Nanowire Arrays by E-beam Lithography 102
6.4 Conclusions 111
6.5 References 112
Appendix A Magnetic Core-Shell Nanowires 114
Appendix B Anodization of Sn Film 121
Vita 129

List of Figures

Figure 1.1 Schematic diagram (left) and FESEM image (right) of cross-section of AAO template.

Figure 1.2 Magnetic hysteresis loop of magnetic nanomaterials with coercivity of 800 Oe.

Figure 2.1 Schematic diagram of anodization processes for conventional AAO templates; (a) etching, (b) second anodization, (c) removal of Al film by using an electrochemical method or $HgCl_2$, (d) removal of Al and barrier layer by using an electrochemical method, and (e) pore opening by using 5 wt% H_3PO_4.

Figure 2.2 Illustration of alumina templates with various pore geometries synthesized under the (a and b) increasing and (c, d, and e) decreasing voltage.

Figure 2.3 Digital photo of (a) unpolished and (b) polished Al films.

Figure 2.4 FESEM images of surface view of unpolished Al film. Images are obtained from the sample in Figure 2.3a.

Figure 2.5 FESEM images of surface view of polished Al film. Images are obtained from the sample in Figure 2.3b.

Figure 2.6 FESEM images of Al surface after etching step in a H_3PO_4-CrO_3 solution at 80 ℃. Al surface was measured at (a) low and (b) high magnification. (c) The tilted image clearly shows the hemispherical Al surface.

Figure 2.7 FESEM images of AAO templates synthesized in (a) 0.3 M H_2SO_4, (b) $H_2C_2O_4$, and (c) H_3PO_4.

Figure 2.8 FESEM images of (a) cross-section view of channel type AAO templates with length of 10 μm synthesized in 0.3 M $H_2C_2O_4$ and its pore channels measured at (b) the top and (c) bottom area. Straight pore channels with 40 nm diameters and 100 nm interpore distances are opened from top to bottom.

Figure 2.9 FESEM image of cross section of AAO templates synthesized in 0.3 M $H_2C_2O_4$ at fluctuate voltage.

Figure 2.10 FESEM images of pore in pore structures after second anodization in 0.3 M H_3PO_4.

Figure 2.11 FESEM images of bottom surface view of (a) cylinder type and (b) channel type AAO synthesized in 0.3 M $H_2C_2O_4$.

Figure 2.12 FESEM images of AAO templates with (a) 40 nm, (b) 60 nm, and (c) 80 nm pore diameters. After second anodization in 0.3 M $H_2C_2O_4$, the templates were immersed in 5 wt% H_3PO_4 for (a) 10 min, (b) 30 min, and (c) 50 min.

Figure 2.13 FESEM images of alumina templates with selectively opened pore structures synthesized under the increasing voltage from 20 V (sulfuric acid) to 80 V (oxalic acid); (a and b) surface view, and (c) cross-sectional view of the template.

Figure 2.14 FESEM images of the alumina template with selectively opened pore structures synthesized under the increasing voltage; (a) 20 V (0.3 M sulfuric acid, 10 ℃) to 40 V (0.3 M oxalic acid, 17 ℃), (b) 40 V (0.3 M oxalic acid, 17 ℃) to 80 V (0.3 M oxalic acid, 17 ℃), and (c) 40 V (0.3 M oxalic acid, 17 ℃) to 160 V (0.3 M phosphoric acid, 5 ℃).

Figure 2.15 (a) FESEM images of Ni nanowires in the alumina template with spherical feature along the straight pore channels. The template was synthesized under the increasing voltage in 0.3 M oxalic acid. (b) Magnified FESEM image corresponding to the white square in (a).

Figure 2.16 FESEM images of cross-sectional view of alumina templates with (a and b) arch-shaped, (c and d) tree-like, and (e and f) branched pore geometries which are synthesized under the decreasing voltage. Capital ‘A’ and ‘B’ marked in image (a, c, and e) are indicating oxide layers which are synthesized at second and third anodization processes. (b, d, and f) Images are magnified from the interface between ‘A’ and ‘B’. D_a is a distance of branched pores.

Figure 2.17 FESEM images of surface and cross-sectional view of alumina templates; (a and b) no acid treatments, (b and c) 20 min acid treatments, (e and f) 40 min acid treatments after second anodization processes at 40 V in 0.3 M oxalic acid.

Figure 2.18 FESEM images of top and bottom surface view of alumina templates with various pore geometries; (a and b) arch-shaped, (c and d) tree-like, and (e and f) branched alumina templates. When we compare the pore diameters in Figures 2.18(a, c, and e) with that in Figure 2.17, the pore diameters in Figure 2.18 were increased because of the additional 20 min acid treatments after a third anodization. The pore diameters of (a), (b), and (c) are 60 nm, 70 nm, and 80 nm, respectively.

Figure 2.19 FESEM images of the alumina template with branched pore structures synthesized under the decreasing voltage from 80 V (second anodization) to

40 V (third anodization) in oxalic acid; (a) top and (b) bottom surface view, and (c) cross-sectional view of the template. (d) Ni nanowires synthesized in the template. Inset shows the magnified image of branched Ni nanowires (scale bar is 1 μm).

Figure 2.20 FESEM images of the 2+2 branched alumina template which is synthesized under the decreasing voltage (60, 42, and 30 V in 0.3 M oxalic acid); (a) top and (b) bottom surface and (c, d, and e) cross-sectional view. 'A', 'B' and 'C' marked in image (e) are indicating oxide layers which are synthesized at 60 V (second), 42 V (third) and 30 V (forth anodization), respectively. (c and d) Images are magnified from the interfaces between two regions; (c) A-B interface and (d) B-C interface. (f) FESEM image of branched Ni nanowires synthesized in the template.

Figure 2.21 (a) Schematic illustration of the relative electric field strength (E) under the different thickness of barrier layer (T_b). (b) Schematic illustration of the third anodization occurred at the reduced voltage. U is an applied voltage.

Figure 3.1 Illustration of electrodeposition system to fabricate nanostructures in AAO.

Figure 3.2 FESEM images of cross-section view of Fe nanostructures in conventional AAO with 60 nm pore diameters and 100 nm interpore distances. (a) nanodots, (b) nanorods, and (c) nanowires.

Figure 3.3 FESEM images of Fe nanostructures without AAO templates; (a) nanodots, (b) nanorods, and (c) nanowires.

Figure 3.4 XRD result of Fe nanowires with the diameter of 60 nm. * indicates Ag peak at the bottom of the pore.

Figure 3.5 Hysteresis loops of Fe nanostructures in AAO; (a) nanodots, (b) nanorods, and (c) nanowires.

Figure 4.1 Schematic diagram of fabrication procedures for AAO templates. (a) First anodization of polished Al film at 40 V and 17 ℃, (b) etching of oxide layer, (c) second anodization at 40 V and 17 ℃ (Mi-AAO), (d) third anodization at 100 V and 5 ℃ (Mi-Ha AAO), and (e) after removal of barrier layer and Al film.

Figure 4.2 FESEM images of surface view of Mi-Ha AAO templates. (a) Top surface of mild side, (b) bottom surface with barrier layer (cylinder type) and (c) without barrier layer (channel type).

Figure 4.3 FESEM images of cross-section view of Mi-Ha AAO templates. (a) mild side, (b) hard side, (c) the boundary of mild (top) and hard side (bottom), and (f) higher magnification view of boundary region of mild (top) and hard side

(bottom); black arrows highlight some selected pores that have been terminated in the hard anodization step.

Figure 4.4 FESEM images of Ni nanowires synthesized in Mi-Ha AAO template. (a) 110 nm diameter wires grown in the hard side of the template. (b) 70 nm nanowires grown on mild side; growth of wires in alternating pores clearly shown. Nanowires grown across mild-hard interface, larger diameter portion of wire from hard side of template: (c) wires still in template, (d) wires shown after removal of template.

Figure 4.5 TEM images and diffraction data for Ni nanowires. (a) TEM image of dispersed Ni nanowires synthesized in mild side of Mi-Ha (a1) and Mi-AAO (a2). Inset shows SAED pattern, indicating polycrystalline structure. (b) XRD data for Ni nanowires in AAO templates; (b1) mild side and (b2) hard side of Mi-Ha AAO, (b3) normal Mi-AAO. (Ag from conducting film on bottom of AAO template.)

Figure 4.6 TEM images and diffraction data for Co nanowires. (a) TEM image of dispersed Co nanowires synthesized in mild side of Mi-Ha (a1) and Mi-AAO (a2). Inset shows SAED pattern, indicating polycrystalline structure. (b) XRD data for Co nanowires in AAO templates: (1) mild side and (2) hard side of Mi-Ha AAO, and (3) normal Mi-AAO. (Ag from conducting film on bottom of AAO template.)

Figure 4.7 Hysteresis loops of Ni nanowires; (a, b) synthesized in Mi-Ha AAO (70 nm diameters, 200~300 nm interwire distances) with the length of (a) 3.3 μm, and (b) 11 μm; (c) synthesized in Mi-AAO (70 nm diameters, 100 nm interwire distances) with 3.4 μm in length; (d) synthesized in hard side of Mi-Ha AAO (110 nm diameters, 265 nm interwire distances) with 3.8 μm length**.**

Figure 4.8 Hysteresis loops of Co nanowires; (a) synthesized in Mi-Ha AAO (70 nm diameters, 200~300 nm interwire distances) with the length of 4.5 μm; (b) synthesized in Mi-AAO (70 nm diameters, 100 nm interwire distances) with 4.7 μm length; (c) synthesized in hard side of Mi-Ha AAO (110 nm diameters, 265 nm interwire distances) with 4.8 μm length.

Figure 5.1 FESEM images of cross-sectional view of nanotubes electrodeposited for (a-c) 5 min and (d-f) 15 min; (a and d) as-synthesized (β-FeOOH), (b and e) after heating in air at 500 ℃ (α-Fe_2O_3), and (c and f) after heating in O_2 flowing at 500 ℃ (α-Fe_2O_3). As-synthesized and oxygen heated nanotubes have plate-like features inside the tubes marked as black arrows in image (a).

Figure 5.2 XRD results of α-Fe_2O_3 nanotubes (a) Fe_2O_3-air and (b) Fe_2O_3-ox. The alumina templates were partly dissolved before the measurement.

Figure 5.3 (a) FESEM and (b) TEM images of Fe_2O_3-air. After heating in air at 500 ℃,

the alumina templates were dissolved in a 0.1 M NaOH solution.

Figure 5.4 FESEM images of (a) side and (b) top surface of α-Fe_2O_3 nanotubes heated in O_2 gas at 500 ℃. Arrows indicate plate-like structures located in the transparent nanotubes. (c) TEM image and (d) SAED pattern of iron oxide nanotubes of Fe_2O_3-ox. The nanotubes consist of nanoparticles with 4~18 nm diameters and show polycrystalline α-Fe_2O_3. (e) The lattice fringe of 0.25 nm corresponds to the hematite iron oxide.

Figure 5.5 Hysteresis loops of α-Fe_2O_3 nanotubes; (a-c) Fe_2O_3-air and (d-f) Fe_2O_3-ox, electrodeposited for (a and d) 5 min, (b and e) 10 min, and (c and f) 15 min. The magnetic field was applied parallel (0 degree, black) and perpendicular (90 degree, red) to the nanotubes. Hematite Fe_2O_3 nanotubes show a superparamagnetic behavior.

Figure 5.6 FC-ZFC magnetization curves of (a) Fe_2O_3-air and (b) Fe_2O_3-ox. The magnetic field of 500 Oe was applied perpendicular (90 degree) to the nanotubes.

Figure 5.7 FESEM images of Fe_3O_4 nanotubes after heating in H_2/N_2 flowing at 600 ℃; (a) Fe_3O_4-air-hy and (b) Fe_3O_4-ox-hy.

Figure 5.8 (a-c) TEM images and (d) SAED pattern of Fe_3O_4-air-hy after heating in H_2/N_2 flowing at 600 ℃, where the samples are from air-heated Fe_2O_3 (Fe_2O_3-air). (b and c) Images are magnified from the white box in (a) image.

Figure 5.9 (a and b) TEM, (c) SAED pattern, and (d) HRTEM images of Fe_3O_4-ox-hy after heating in H_2/N_2 flowing at 600 ℃, where the samples are from O_2-heated α-Fe_2O_3 (Fe_2O_3-ox). (c and d) Images are consistent with magnetite iron oxide structures with the lattice fringe of 0.257 nm.

Figure 5.10 XRD results of Fe_3O_4 nanotubes obtained after heat treatments in H_2/N_2 flowing at 600 ℃; (a) Fe_3O_4-air-hy and (b) Fe_3O_4-ox-hy. Broad peaks at 20~30 and 60~70 degrees are from partly dissolved alumina templates.

Figure 5.11 Hysteresis loops of Fe_3O_4 nanotubes; (a) Fe_3O_4-air-hy and (b) Fe_3O_4-ox-hy. The magnetic field was applied parallel (0 degree, black) and perpendicular (90 degree, red) to the nanotubes. FC-ZFC magnetization curves of Fe_3O_4 nanotubes; (c) Fe_3O_4-air-hy and (d) Fe_3O_4-ox-hy. The magnetic field of 500 Oe was applied perpendicular (90 degree) to the nanotubes. (c) FC-ZFC curve shows the Verwey transition at about 125 K (indicated with arrow).

Figure 5.12 Illustration of synthesis procedures of β-FeOOH nanotubes using alumina templates. (a) The alumina template is soaked in the electrolyte. (b) β-FeOOH tubes are rapidly growing along the pore channels. (c) β-FeOOH is also slowly growing perpendicular to the walls of the nanotubes and thin

plate-like structures are produced within the tubes. (d) Tubular structures with bridging plate components are continually growing during electrodeposition.

Figure 6.1 Schematic diagram of patterning of nanowires and cup-shaped structures; (a) Ag coating on ordered PS spheres, (b) electrodeposition, and (c) removal of spheres and membrane.

Figure 6.2 Schematic diagram of synthetic procedures of patterned nanowire arrays on AAO templates.

Figure 6.3 FESEM images of ordered PS spheres on AAO templates; (a) 100 nm and (b) 950 nm PS spheres. Inset shows how the spheres are ordered on templates. 100 nm PS spheres are closed all pores and 950 nm PS, however, can make open pore channels as shown in (b).

Figure 6.4 (a) FESEM image of porous thin Au film on AAO templates after removal of Au coated PS by ultra-sonication. TEM images of nanometer scale cup-shaped Au on the PS spheres (b) and without PS spheres (c).

Figure 6.5 FESEM images of Ag cups with 1 μm outer diameter on AAO templates.

Figure 6.6 FESEM images of (a) Au nanowires on Ag film after removal of AAO templates and (b) Au nanowires after removal of both Ag film and templates. When 100 nm PS spheres are coated on AAO templates with 100 nm interpore distances, no patterned structures are observed.

Figure 6.7 FESEM image of patterned Au nanowire arrays on Ag cups; (a) cross-section view, (b) illustration of its morphology, (c) tilted image, and (d) top surface view of nanostructures.

Figure 6.8 (a) Original portrait image of former Korean President Moo-Hyun Roh. Optical micrographs of a portrait, Moo-Hyun Roh; (b) e-beam patterning, (c) Ni electrodeposition and removing of PMMA, and (d) free standing Ni nanowires after removing of AAO template. Scale bar is 100 μm.

Figure 6.9 FESEM images of patterned nanowire corresponding to Figure 6.8. (a) Patterned portrait is composed bundle of Ni nanowires with 70 nm diameters. Magnified images (b-d) show detail nanowire structures grown each dots. The length of nanowires is about 15 μm. Some nanowires were over grown and show large particles at the end of the nanowires.

Figure 6.10 FESEM images of patterned nanowire arrays with different designs; (a) Ni nanowire arrays with line width of 9.5 μm in ‘UNO’, (b) Au nanowires with line width of 5 μm in squares, Ni nanowires with line width of (c) 4.2 μm and (d) 6.5 μm in simple line patterns.

Figure 6.11 FESEM images of (a) patterned Au dot arrays on Mi-Ha AAO and (b) Ni nanowires in hard side of Mi-Ha AAO. Inset shows magnified image of Ni nanowires. Scale bar is 200 nm.

Figure 6.12 Optical micrographs of patterned Ni nanowires synthesized in normal AAO templates; (a) after e-beam patterning, (b) Ni electrodeposition, and (c) removal of PMMA and AAO template.

Figure 6.13 (a) FESEM images of patterned Ni nanowires synthesized in normal AAO. (b) High magnification images show that the distance between two patterns is about 7 μm. (c) The diameter and length of nanowires are 70 nm and 2.8 μm, respectively.

Figure 6.14 (a) Optical micrograph and (b) FESEM images of Ni nanowire arrays patterned on mild side of Mi-Ha AAO templates, where the wire diameter is 80 nm. Inset shows that two Ni nanowires were grown on one patterned position. Room temperature hysteresis loops of patterned Ni nanowires with (c) 80 nm and (d) 120 nm diameters.

Figure A.1 Schematic diagram for preparation of metal core-shell nanowire arrays; (a) first electrodeposition, (b) second electrodeposition, and (c) removing of AAO templates.

Figure A.2 FESEM images of (a) cross-section view of Ag film on AAO and (b) surface view of Ag film after removal of AAO. The thickness of Ag film is around 200~300 nm.

Figure A.3 FESEM images of (a) Ni nanotubes synthesized at -0.5 mA, (b) Ni nanotubes synthesized at -0.7 mA, and (c) Co nanotubes synthesized at -0.5 mA.

Figure A.4 FESEM images of (a, b) NiCo, (c) CoNi, and (d) AuNi core-shell nanowire arrays.

Figure A.5 EDS of (a) Ni nanotube, (b) Co nanotube, (c) CoNi, and (d) NiCo core-shell nanowire after removal of the AAO.

Figure A.6 XRD results of (a) NiCo core-shell nanowires, (b) Co nanotubes, and (c) Ni nanotubes (Ag from conducting film on bottom of AAO template).

Figure A.7 TEM images and SAED pattern of NiCo core-shell nanowires.

Figure B.1 FESEM images of (a) top surface view and (b) cross-section view of plate-like SnO.

Figure B.2 FESEM images of porous SnO synthesized in 0.3 M $H_2C_2O_4$; (a) low and (b) high magnification.

Figure B.3 (a and b) TEM and (c) HRTEM images of porous SnO nanostructures. (d) EDS peaks of porous SnO nanostructures. Cu peaks are from TEM grid.

Figure B.4 XRD result of porous SnO nanostructures synthesized by anodization of Sn using 0.3 M $H_2C_2O_4$.

Figure B.5 FESEM images of (a) top and (b) cross-section view of SnO_2 nanostructures. (c) TEM and (d) HRTEM images of SnO_2 nanostructures, where the samples are prepared after heat treatments of SnO in Figure B.2.

Figure B.6 XRD results of SnO_2 nanostructures obtained from the sample in Figure B.5.

Figure B.7 FESEM images of (a and b) SnO and (c and d) SnO_2 nanostructures synthesized by anodization in 0.1 M $H_2C_2O_4$.

Figure B.8 (a and b) FESEM images and (c) XRD result of SnO_2 nanostructures synthesized by anodization in 0.05 M $H_2C_2O_4$, where the oxide layers were not heated at 500 ℃. SnO synthesized in 0.05 M $H_2C_2O_4$ very quickly reacted with water and oxygen in air to produce the mineral cassiterite, SnO_2.

List of Tables

Table 2.1 Various AAO membranes synthesized under different anodization conditions.

Table 2.2 Conventional anodization conditions for synthesis of porous AAO templates with different pore diameters and interpore distances.

Table 2.3 Structural properties of as-synthesized conventional AAO templates.

Table 2.4 Varied pore diameters and interpore distances produced under the increasing voltage conditions.

Table 2.5 Structural properties of alumina templates with various pore geometries. The thickness of barrier layer (T_b) and pore diameters (D_p) observed before a third anodization are corresponding to Figure 2.17.

Table 4.1 Structural properties of normal Mi-AAO and Mi-Ha AAO template.

Table 4.2 Summary of magnetic data for Ni and Co nanowire composite arrays.

Abbreviations

AAO	Anodic aluminum oxide
Mi-AAO	Normal anodic aluminum oxide
Mi-Ha AAO	Mild-hard anodic aluminum oxide
FESEM	Field emission scanning electron microscopy
TEM	Transmission electron microscopy
XRD	X-ray diffraction
EDS	Energy dispersive spectrometry
SQUID	Superconducting quantum interface device
BET	Brunauer-Emmett-Teller
FC-ZFC	Field cooled and zero field cooled
AFM	Atomic force microscopy
VSM	Vibrating sample magnetometer
LED	Light emitting diode
CVD	Chemical vapor deposition
MOCVD	Metal organic chemical vapor deposition
SFC	Supercritical fluid
ALD	Atomic layer deposition
WE	Working electrode
CE	Counter electrode
SW model	Stoner–Wohlfarth model

SAED	Selected area electron diffraction
OM	Optical microscope

Abstract

In this study, template-based methods are used for the fabrication of various nanostructures such as nandots, nanorods, nanowires, nanotubes, and core-shell structures. Porous alumina membranes were employed as templates and metal nanostructures were synthesized in the templates by electrodeposition. By using lithography techniques, controlled patterned nanostructures were also fabricated on alumina templates. The magnetic properties of the various metal nanostructures were investigated. The pore size, interpore distance, and pore geometry highly affect magnetic properties of nanostructures grown in the templates.

Hexagonally ordered porous alumina templates can be fabricated by two-step anodization. The pore diameters and interpore distances were readily controlled by appropriately changing anodization conditions and pore widening time. Alumina templates with various pore geometries were also successfully synthesized by changing applied voltage, increasing and decreasing, during a third anodization step.

To understand magnetic properties of nanostructures with different aspect rations in the form of nanodots, nanorods, or nanowires, Fe nanostructures were fabricated in the templates by controlling of electrodeposition times. The coercivity of nanostructures increased with increasing aspect ratio. The anisotropy of the arrays was governed by the shape anisotropy of the magnetic objects with different aspect ratios.

Electrodeposited Co and Ni nanowires, were also investigated, in the various pore structures of the mild-hard alumina templates. Alumina templates with 200~300 nm interpore distances allows one to probe magnetic interactions between nanowires and compare them to wires grown in conventional alumina templates with 100 nm interpore distances. The magnetic properties of

nanowires in mild-hard alumina and conventional alumina templates showed distinct differences in the squareness of hysteresis loops and coercivity both as a function of pore structure and magnetic component.

Iron oxide nanotubes with a unique inner-surface were also fabricated by an electrodeposition method. β-FeOOH nanotubes were grown in alumina templates and transformed into hematite and magnetite structures during various heating processes. Hematite nanotubes are composed of small nanoparticles less than 20 nm diameters and the hysteresis loops and FC-ZFC curves show superparamagnetic properties without the Morin transition. In the case of magnetite nanotubes, which consist of slightly larger nanoparticles, hysteresis loops show ferromagnetism with weak coercivity at room temperature while FC-ZFC curves exhibit the Verwey transition at 125 K.

For the patterning of nanowires, lithography techniques including nanosphere lithography and e-beam lithography were used. Nanosphere lithography used self-assembled PS spheres as a mask creates holes between spheres and the size of the holes is determined by the size and geometry of ordered PS spheres on the templates. This method can grow patterned nanowires arrays and also produce unique cup-shaped nanostructures with sizes ranging from micrometer down to several nanometers. E-beam lithography was also combined with template-based electrodeposition. Of these two lithographic methods, this one is the most powerful in the fabrication of patterned nanostructures with high aspect ratios. Various features and the sizes of patterned structures can be readily controlled. By the directing the pore diameters and interpore distances of the alumina template, the size and number of patterned nanowires are also adjustable.

Keywords: *nanomaterials, anodization, electrodeposition, magnetism, porous templates, nanowires, nanotubes, e-beam lithography, and nanosphere lithography*

Chapter 1

Introduction and Research Background

1.1 Nanotechnology

Nanotechnology is research conducted at the nanoscale (10^{-9} meters, nm) for development at atomic and molecular levels to create miniaturized devices or systems with better quality. It becomes the most influential force in modern technology and has been used for environmental cleaning up from toxic waste, cancer therapy, display device, recording media, and so on.[1]

For the manufacture of nanomaterials, top-down and bottom-up approaches are often used. Top-down approaches are the method to create nanoscale materials with desired shape and order by starting from larger one. Lithography such as photolithography or electron-beam lithography is a representative top-down fabrication technique where a bulk material is reduced in size to nanoscale pattern. Also, focused ion beam, directly removing materials or even deposit materials when suitable precursor gas is applied, is used routinely to create nanoscale materials. In contrast, bottom-up approaches seek to use small components at the molecular level to build up more complex and nanoscale materials. Various synthetic methods such as self-assembly, sol-gel, and electrodeposition are included in these techniques.[1,2]

The ability to characterize of nanomaterials has played an important role in their development because it is too small to see with the eye or even with microscopes that use visible light. Therefore, the visualization technologies are important to measure or manipulate the nanosize materials. In the early 1930s, scanning electron microscopy (SEM) and transmission electron

microscopy (TEM) were developed. The images obtained by TEM are emphasized morphology features including the size, shape and arrangement of particles. This technique can also give compositional information as well as crystallographic information. SEM can be one of the most versatile instruments to determine morphology, topography, and chemical composition of the specimen. Currently, the electron beam in the SEM system can also be used as a source of electron-beam lithography to create patterned nanostructures at desired locations. In the early 1980s, atomic force microscopy (AFM) was developed by Gerd Binning at IBM in Switzerland. It is a tool not only showing the images that display the configuration of atoms and molecules, but also manipulating or moving atoms into artificial configurations.[1,3-5]

1.2 Template-based Electrodeposition

According to the development of nanotechnology, many kinds of nanomaterials with various shapes, sizes, and crystalline structures have been synthesized. The fabrication of nanostructures such as nanoparticles, nanorods, nanowires, nanotubes and core-shell nanowires have received considerable attention because of their potential applications in fields as diverse as electronics, magnetics, optical devices, and catalysts.[6-10] Among the various methods for fabrication of nanostructures, the template-assisted electrodeposition technique has been extremely prolific in the preparation of a wide range of metallic, semiconductor, and polymeric nanowires because it is a simple and inexpensive technique.[11] Furthermore, with this method it is easy to control the size, shape, and structural properties of nanostructures through the modification of templates and electrodeposition conditions.

1.2.1 Anodic Aluminum Oxide Templates

Commercially available anodic alumina and polycarbonate track etch membranes are commonly used as templates. Such templates can however have disadvantages over homemade membranes due to branched pore structures and randomly distributed pores. Advances in the synthetic techniques in membrane production have lead to almost perfectly ordered porous alumina structures with controlled pore diameters (D_p), interpore distances (D_i), and thicknesses. Since Masuda and co-workers reported the two-step oxidation process for the synthesis of anodized aluminum oxide (AAO) templates with highly ordered hexagonal nanopores, many researchers have studied these materials.[5,12,13] Conventional AAO templates are typically synthesized under the well-known 'mild' anodizing conditions. Variations in reaction conditions allow one to control pore sizes and interpore distances. Examples include (1) 0.3 M H_2SO_4 at 25 V for 20 nm pore sizes with 60 nm interpore distances, (2) 0.3 M $H_2C_2O_4$ at 40 V for 40 nm pore sizes with 100 nm interpore distances, and (3) 0.1 M H_3PO_4 at 195 V for 400 nm pore sizes with 500 nm interpore distances.[12,13]

The templates synthesized by anodization consist of two layer structures including porous and barrier layers as shown in Figure 1.1. An alumina barrier layer contacts with the aluminum film with hemispherical geometry and a porous layer containing straight pore channels is above the barrier layer.[14] For the growing of nanostructures in porous templates by electrodeposition, the barrier layer and Al are first dissolved before a thin metal layer that is coated on one side to act as a working electrode. In addition, another metal component is needed to act as a counter electrode. The positive ions in the electrolyte will move toward the cathode (working electrode) and the negatively charged ions toward the anode (counter electrode) and the metal atoms will be deposited within the pore channels of AAO templates.

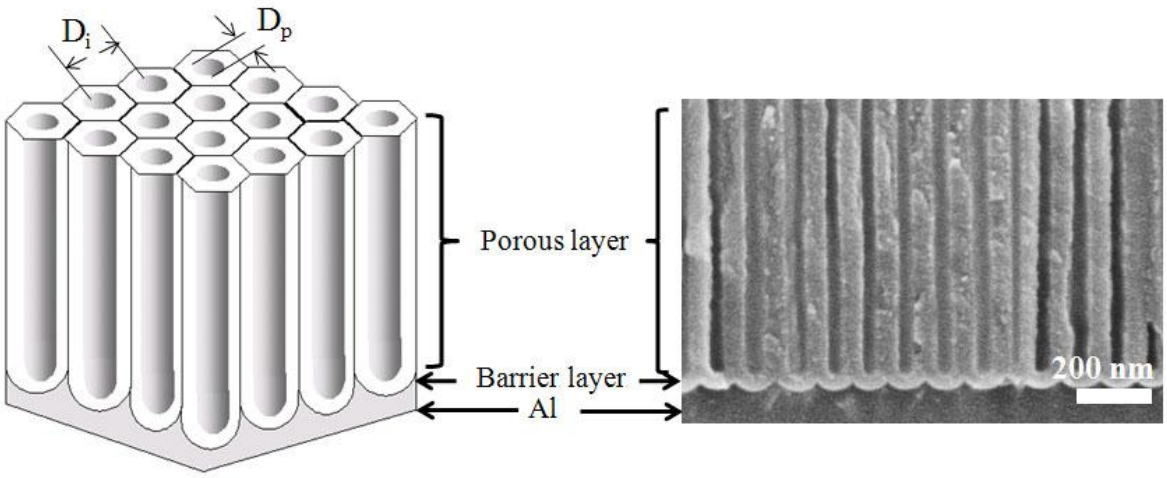

Figure 1.1 Schematic diagram (left) and FESEM image (right) of cross-section of AAO template.

1.2.2 Electrodeposited Nanomaterials

Previously various nanomaterials including semiconductor, polymer, thermoelectric, and magnetic have been synthesized by template-based electrodeposition. Semiconductor nanowires can be used as chemical gas sensors, light emitting diodes (LEDs), and transistors because of their large surface-to-volume ratios as well as their tunable optical and electrical properties.[15] Semiconductor nanomaterials including ZnO, SnO_2, TiO_2, HfO_2 and WO_3 were produced by various physical and chemical methods such as chemical vapor deposition (CVD), thermal evaporation, conventional metal organic chemical vapor deposition (MOCVD), sol-gel approach, and template-based electrochemical method.[15-19] Even though several approaches can be used to prepare a nanostructure with uniform size and morphology, relatively little work related to the electrochemically synthesized one-dimensional ZnO and SnO_2 nanostructures has been reported.[15-22] Further, for the fabrication of TiO_2, HfO_2, and WO_3 nanomaterials, it is very hard to find stable conditions in template-based electrodeposition so that several research groups had to

develop anodization techniques using pure metal films.[23-25]

Conducting polymers such as poly(3,4-ethylenedioxythiophene) (PEDOT), polypyrrole (PPY), polyaniline (PANI), polythiophene (PT) and poly(3-methythiophene) (P3MT) are emerging as promising materials for applications pertinent to displays, energy storage devices, actuators, sensors, etc.[26-29] Conducting polymers exhibit electrical, electronic, magnetic and optical properties similar to metals or semiconductors.[30-32] Many of the applications of conducting polymers rely on the redox properties. Conducting polymers can be reversibly reduced and oxidized using chemical or electrochemical methods.[33] The reversible interchange between the redox states gives a possibility to control their properties such as polymer conformation, doping level, conductivity, and color.[32]

In recent research for thermoelectric materials, theoretical predictions suggest that the thermoelectric properties of nanostructures will be significantly enhanced compared with bulk materials.[34,35] However, a single nanowire does not carry a high enough current for thermoelectric materials applications.[36] To collect dense nanowire arrays, researchers need to find new approaches like template-assisted electrodeposition. However, most of the nanowires synthesized by template-assisted electrodeposition have a disadvantage in that it is hard to measure thermoelectric properties because the final structure is contained in the polycrystalline structure in porous templates.[37,38] Further, the preparation of single crystalline nanowires is still a challenge.

One-dimensional magnetic nanomaterials are of great interest in magnetic recording media, giant magnetoresistance and spintronics.[39] Most of the previous work in ferromagnetic nanowire arrays has focused on the magnetization reversal mechanism and high-density magnetic recording media.[40] For magnetic recording media applications, the wire diameter and the

interwire distance should be as small as possible to increase the recording density. Thus, most magnetic studies concentrate on sub-100 nm wires.[41] The development of magnetic recording media is restricted by the superparamagnetic limit. To overcome this limitation either the effective anisotropy of the material or the thickness of the nanostructures can be increased.[42] Magnetic properties of nanomaterials are determined by magnetostatic interaction among nanowires and magnetic anisotropy such as magnetocrystalline and shape anisotropy.[43] The parameters such as length, diameter, and interwire distance of nanowires, which influence the anisotropy and magnetostatic interaction, can be tuned by adjusting templates and electrodeposition conditions.[44]

1.2.3 Magnetism

In my research, most of the nanostructures are based on the magnetic materials synthesized by template-based electrodeposition. Before discussing the research project details, this section provides a brief description of the basic concepts of magnetism which are the properties of materials that respond to an applied magnetic field, an attraction, repulsive forces to one another or influence on other materials.

Magnetic field strength is designated by H. Here the magnetic flux density (B) represents the magnitude of the internal field strength within a substance that is subjected to a magnetic field.[45,46] Hence the relationship between magnetic field strength and flux density is a characteristic property of the materials itself according to

$$B=\mu H$$

The parameter μ is called the permeability, which is a property of the specific medium through which the H field passes and in which the B is measured. The magnitude of magnetization (M)

which is defined as the total magnetic moment per volume unit is proportional to the applied field as follows:

$$M=\chi_m H$$

here χ_m is called the magnetic susceptibility and is the ratio between M and H.[45,46]

When a material is placed within magnetic field, the magnetic forces will be affected. Most materials can be classified as diamagnetic, paramagnetic, ferromagnetic, antiferromagnetic, or ferrimagnetic. [45-49]

Diamagnetism is a property of all materials although it is usually very weak. Diamagnetic materials have a negative susceptibility to magnetic fields. It composed no net magnetic moment in the absence of an external field because all the orbitals are filled and there are no unpaired electrons. When the field is applied to the materials, dipoles are aligned opposite to the field direction.

Paramagnetic materials have a net magnetic moment due to the presence of some unpaired electrons. In the absence of a magnetic field, there is no net magnetism because the orientations of magnetic moments are random. However, under the magnetic field, the realignment of the electron paths was caused. Paramagnetic materials have relatively small but positive susceptibility to magnetic fields. Susceptibilities for paramagnetic materials range from about 10^{-5} to 10^{-2}.

Some metallic (Fe, Co, or Ni) materials have a permanent magnetic moment in the absence of a magnetic field. It exhibits a strong attraction to magnetic fields and is possible to retain their magnetic properties even in the absence of a magnetic field. These materials are called ferromagnetic materials and the strong magnetic properties are observed due to the presence of magnetic domains, where a lot of spin moments are aligned parallel over relatively large volume

regions.

Antiferromagnetism refer to the phenomenon occurs in some materials which have magnetic moment coupling between adjacent atoms or ions, where the coupling results in an antiparallel alingnment of the spins. Therefore, there is no net magnetic moment.

Ferrimagnetism have a permanent magnetization and ferrimagnets are similar to the ferromagnets, except that the moments of adjacent atoms or ions are in an antiparallel alignment, but they do not cancel out each other. The representative material is magnetite (Fe_3O_4) which can be written as $(Fe^{3+})_A(Fe^{2+}, Fe^{3+})_BO_4$ and have inverse spinel structures. The O^{2-} ions are magnetically neutral and the Fe ions in A and B sites result in a net spin moment. In other words, the Fe^{3+} ions located in A and B sites are opposite and cancel each other, but Fe^{2+} ions occupied the B site can produce a net spin moment. There are antiparallel spin coupling interactions between the Fe ions, so the net moment arises from the incomplete cancellation of spin moments.

1.2.4 Hysteresis Loop

Magnetic properties of materials can be characterized by studying its hysteresis loop which is a plot of magnetic flux density, B, (or magnetization, M) against applied magnetic field as shown in Figure 1.2. When the material is initially unmagnetized, M and H are zero. As a function of H, M begins to increase slowly, finally leveling off and becoming independent of H. Initially, the moments of the constituent domains are randomly oriented. After the field is applied, the domains are oriented in directions to the applied field and this process continues with increasing field until the magnetization has reached its maximum where all the spins are aligned and called saturation magnetization (M_S). When H reduced to zero, a residual M exists and is called the remanant magnetization (M_R). The field that needs to be applied in the reverse direction to

reduce the M to zero is called coercivity (H_C). Upon continuation of the applied field in the reverse direction, saturation is achieved in the opposite sense. The ratio of M_R/M_S is generally used as the squarness of hysteresis loops. The magnetic hysteresis loops are dependent on the material, size, shape of samples, and orientation of applied magnetic field. [44,46-48,50]

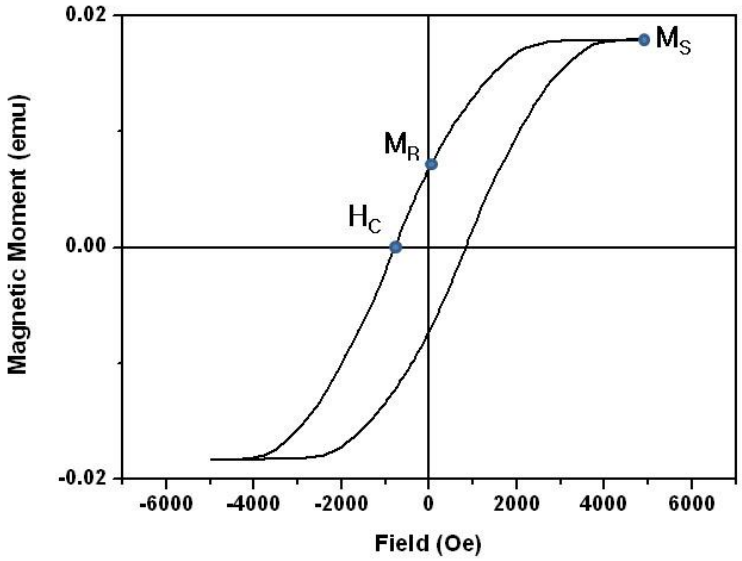

Figure 1.2 Magnetic hysteresis loop of magnetic nanomaterials with coercivity of 800 Oe.

1.3 References

1. 'The ethics and politics of nanotechnology' published in 2006 by the United Nations Educational, Scientific and Cultural Organization.
2. Geoffrey A Ozin and André C Arsenault, 'Nanotechnology' published in 2005 by the Royal Society of Chemistry Publishing, pp 1~44.
3. David B. Williams and C. Barry Carter, 'Transmission electron microscopy' published in 1996, Plenum Press, New York and London.
4. Weilie Zhou and Zhong Lin Wang, 'Scanning electron microscopy' published in 2007 by Springer.
5. Ampere A Tseng, 'Nanofabrication' published in 2008 by the World Scientific Publishing

Co. Pte. Ltd.
6. Y. Ren, Q. F. Liu, S. L. Li, J. B. Wang and X. H. Han, *J. Magn. Magn. Mater.*, **2009**, *321*, 226.
7. Y. Berdichevsky and Y.-H. Lo, *Adv. Mater.*, **2006**, *18*, 122.
8. D. H. Park, B. H. Kim, M. K. Jang, K. Y. Bae, S. J. Lee and J. Joo, *Synthetic Metals*, **2005**, *153*, 341.
9. J. Joo, D. Hyuk Park, M.-Y. Jeong, Y. B. Lee, H. S. Kim, W. J. Choi, Q.-H. Park, H.-J. Kim, D.-C. Kim and J. Kim, *Adv. Mater.*, **2007**, *19*, 2824.
10. V. Zielasek, B. Jurgens, C. Schulz, J. Biener, M. M. Biener, A. V. Hamza and M. Baumer, *Angew. Chem. Int. Ed.*, **2006**, *45*, 8241.
11. J. Qin, J. Nogués, M. Mikhaylova, A. Roig, J. S. Muñoz and M. Muhammed, *Chem. Mater*., **2005**, *17*, 1829.
12. G. Meng, A. Cao, J.-Y. Cheng, A. Vijayaraghavan, Y. J. Jung, M. Shima, and P. M. Ajayan, *J. Appl. Phys*., **2005**, *97*, 064303.
13. Feiyue Li, Lan Zhang, and Robert M. Metzger, *Chem. Mater*., **1998**, *10*, 2470.
14. Woo Lee, Jae-Cheon Kim, and Ulrich Gsöele, *Adv. Func. Mater*., **2010**, *20*, 21.
15. J. S. Wright, W. Lim, D. P. Norton, S. J. Pearton, F. Ren, J. L. Johnson and A. Ural, *Semicond. Sci. Technol.*, **2010**, *25*, 024002.
16. M. Lai, J.-H. Lim, S. Mubeen, Y. Rheem, A. Mulchandani, M. A. Deshusses and N. V. Myung, *Nanotechnology*, **2009**, *20*, 185602.
17. S. Mathur, S. Barth, H. Shen, J.-C. Pyun and U. Werner, *Small*, **2005**, *1*, 173.
18. Y. Liu and M. Liu, *Adv. Funct. Mater.*, **2005**, *15*, 57.
19. Z. R. Dai, J. L. Gole, J. D. Stout and Z. L. Wang, *J. Phys. Chem. B* **2002**,*106*, 1274.
20. M. Zheng, G. Li, X. Zhang, S. Huang, Y. Lei and L. Zhang, *Chem. Mater.*, **2001**, *13*, 3859.
21. X. Y. Kong and Z. L. Wang, *Appl. Phys. Lett.*, **2004**, *84*, 975.
22. L. Li, S. Pan, X. Dou, Y. Zhu, X. Huang, Y. Yang, G. Li and L. Zhang, *J. Phys. Chem. C* **2007**, *111*, 7288.
23. D. Gong, C. A. Grimes, O. K. Varghese, W. C. Hu, R. S. Singh, Z. Chen and E. C. Dickey, *J. Mater. Res*., **2001**, *16*, 3331.
24. S. Berger, H. Tsuchiya, A. Ghicov and P. Schmuki, *Appl. Phys. Lett*., **2006**, 88 203119.
25. X. Qiu, J. Y. Howe, M. B. Cardoso, O. Polat, W. T. Heller and M. P. Paranthaman, *Nanotechnology*, **2009**, *20*, 455601.
26. Y. Berdichevsky and Y.-H. Lo, *Adv. Mater.*, **2006**, *18*, 122.
27. A. Kros, R. J. M. Nolte and N. A. J. M. Sommerdijk, *Adv. Mater.*, **2002**, *14*, 1779.
28. J. C. W. Chien and J. B. Schlenoff, *Nature*, **1984**, *311*, 362.
29. F. Roussel, R. Chan-Yu-King and J.-M. Buisine, *Eur. Phys. J. E*., **2003**, *11*, 293.
30. K. Ramanathan, M. A. Bangar, M. Yun, W. Chen, A. Mulchandani and N. V. Myung, *Nano Lett*., **2004**, *4*, 1237.
31. K. Ramanathan, M. A. Bangar, M. Yun, W. Chen, N. V. Myung and A. Mulchandani, *J. Am. Chem. Soc.*, **2004**, *127*, 496.
32. S. I. Cho and S. B. Lee, *Acc. Chem. Res*., **2008**, *41*, 699.
33. P. N. Bartlett, P. R. Birkin, M. A. Ghanem and C.-S. Toh, *J. Mater. Chem*., **2001**, *11*, 849.
34. A. L. Prieto, M. Martin-González, J. Keyani, R. Gronsky, T. Sands and A. M. Stacy, *J. Am. Chem. Soc*., **2003**, *125*, 2388.
35. A. L. Prieto, M. S. Sander, M. S. Martin-González, R. Gronsky, T. Sands and A. M. Stacy, *J. Am. Chem. Soc*., **2001**, *123*, 7160.

36. C. R. Martin, *Science*, **1994**, *266*, 1961.
37. M. S. Sander, R. Gronsky, T. Sands and A. M. Stacy, *Chem. Mater*., **2003**, *15*, 335.
38. Y. Zhang, L. Li and G. H. Li, *Nanotechnology,* **2005**, *16*, 2096.
39. H. Pan, B. Liu, J. Yi, C. Poh, S. Lim, J. Ding, Y. Feng, C. H. A. Huan and J. Lin, *J. Phys. Chem. B* **2005**, *109*, 3094.
40. Y. Ren, Q. F. Liu, S. L. Li, J. B. Wang and X. H. Han, *J. Magn. Magn. Mater.*, **2009**, *321*, 226.
41. J. Qin, J. Nogués, M. Mikhaylova, A. Roig, J. S. Muñoz and M. Muhammed, *Chem. Mater*., **2005**, *17*, 1829.
42. X.-F. Han, S. Shamaila, R. Sharif, J.-Y. Chen, H.-R. Liu and D.-P. Liu, *Adv. Mater*., **2009**, *21*, 1.
43. M. Darques, J. Spiegel, J. De la Torre Medina, I. Huynen, and L. Piraux, *J. Mag. Mag. Mater*., **2009**, *321*, 2055.
44. Yi Liu, D.J. Sellmyer, and Daisuke Shindo, 'Handbook of advanced magnetic materials', published in 2006 by Springer, pp 229-236.
45. http://www.ndt-ed.org/EducationResources/CommunityCollege/MagParticle/Physics/Quantifying.htm.
46. Lesley Smart and Elaine Moore, 'Solid state Chemistry', published in 1998 by Stanley Thornes Ltd, pp 294-313.
47. Mathias Getzlaff, 'Fundamentals of magnetism', published in 1998 by Springer, pp1-68.
48. William D. Callister, Jr. and David G. Rethwisch, 'Fundamentals of materials science and engineering: An intergrated approach, 3rd editon', published in 2008 by Wiley pp S-263-S292.
49. http://www.ndt-ed.org/EducationResources/CommunityCollege/MagParticle/Physics/MagneticMatls.htm
50. http://www.ndt-ed.org/EducationResources/CommunityCollege/MagParticle/Physics/HysteresisLoop.htm

Chapter 2

Synthesis of Porous Anodic Aluminum Oxide (AAO)

2.1 Introduction

Since Masuda and co-workers reported the two-step anodization process for the synthesis of AAO (anodic aluminum oxide) templates with highly ordered hexagonal nanopores in 1995, porous alumina templates have been attracted much attention.[1] AAO templates are very useful for the fabrication of various nanostructures such as nanodots, nanowires, nanotubes, and core-shell structures.[2-6] Recently, the template-based methods combined with other approaches (e.g. sol-gel, electrodeposition, atomic layer deposition, filtering, etc.) have become one of the most powerful techniques in nanotechnology.[7-10]

In general, alumina templates with well-ordered hexagonal pore structures were produced by two-step anodization in acid solutions.[11] The templates consist of two layer structures including porous and barrier layers. Pore sizes and interpore distances of templates rely heavily on anodization conditions. The growth of alumina (Al_2O_3), due to its low conductivity, takes place at the interface of metal-metal oxide layers. When the barrier layer is thin enough for the anions including O^{2-}, OH^-, and $C_2O_4^{2-}$ generated from the electrolyte can penetrate into the metal-metal oxide interface. These ions can interact with the Al^{3+} ions, yielding a growth of alumina. However, the oxide formation will only continue if the barrier layer remains electrically transparent to the anions. The barrier layer thickness cannot increase any further because of the concentrated electric field occurred at the concaved metal-metal oxide interface and the alumina layers are simultaneously dissolved.[12]

Conventional alumina templates can be produced with a certain number of pore size and interpore distance. For example, 20 nm, 40 nm, and 400 nm pore diameters (D_p) and 60 nm, 100 nm, and 500 nm interpore distances (D_i), respectively, were produced with definite voltage and acid sources, e.g., sulfuric, oxalic, and phosphoric acids.[13,14] Sulfuric-anodized oxide membranes give the smallest pore diameters, therefore yielding the largest pore density. In conventional anodization processes, self ordering of pores requires a porosity of 10% which is independent of anodization conditions; this is called the 10% porosity rule.[15]

There are some limitations with respect to alumna templates. Limited value of pore sizes and interpore distances restrict their application areas, even though the pores can be enlarged by an acid treatment, so-called 'pore widening' process. Also, thin porous alumina templates are easily broken during synthesis processes owing to the fragility of membranes. Therefore, researchers have tried to solve these problems by other approaches instead of simple two-step anodization. First, pre-textured Al films, synthesized by an imprinting technique, created various pore shapes and cell configurations as well as varied interpore distances.[14,16] Second, a hard anodization process, carried out at high electric fields and low temperatures, can produce enlarged interpore distances while maintaining standard pore diameters.[17-19] Third, to improve handling of porous membranes, several researchers prepared anodic alumina templates on hard and thick substrates such as silicon, glass, or indium tin oxide (ITO).[20-22] This was very helpful for the fabrication of stable nanostructures inside the template. In addition, the nanostructures directly formed on a silicon wafer require no additional processes for fabrication of silicon-based electronic devices.

In recent years, researchers have expanded on these techniques by altering the anodization conditions, by a preprocessing of the anode via lithography, or by an imprinting method so as to prepare a variety of structures including AAO membranes with Y-branching,[23,24] six-membered

rings,[25] and triangular and rectangular shapes[14]. Additionally, a hard anodization process, which has a fast film growth rate and a range of interpore distances, has been reported by several research teams to minimize the limitations in processing seen in the production of conventional AAO templates. Li et al.[26] fabricated AAO templates with 70~140 nm or 225~400 nm interpore distances in a H_2SO_4-C_2H_5OH or $H_2C_2O_4$-C_2H_5OH solutions, respectively. Lee et al.[18,27] used $H_2C_2O_4$ solution in the synthesis of hard anodized AAO templates with 200~300 nm interpore distances or used H_2SO_4 solution for synthesis of alumina nanotubes based on a pulsed technique involving a combination of mild and hard (Mi-Ha) anodization steps. Table 2.1 summarizes the various AAO membranes synthesized by different anodization conditions.

In this chapter, we discuss the synthesis and microscopic characterization of conventional porous alumina and modified alumina templates by controlling anodization conditions. The modified alumina templates exhibit unique pore structures, from only small changes in anodization conditions.

2.2 Experimental

2.2.1 Anodization of Conventional AAO Templates

Aluminum film (Sigma-Aldrich, 99.999%) was annealed at 450 ℃ for 5 h in Ar gas. Al surface was electrochemically polished at 25 V in a 1:4 mixture solution of $HClO_4$ and CH_3CH_2OH (10 ℃) to remove naturally oxidized layers.

Conventional AAO templates were synthesized by the well-known two-step anodization processes as summarized in Table 2.2. Figure 2.1 shows schematic diagram of anodization processes. The Al film was anodized in an acid solution at constant voltage for 12 h. After first anodization, the oxide layer was completely etched away at 80 ℃ in a solution of 1.8 wt%

chromic acid-5 wt% phosphoric acid. A second anodization was then carried out under the same conditions as the first anodization. Two carbon bars were employed as a counter electrode and a Kepco power supply (KLP 300-8-1200) was used to control current and voltage. During the anodization, the solution was maintained at constant temperature by using controlled temperature circulator with vigorous stirring. All of the samples were thoroughly washed with distilled water and acetone after each step.

Table 2.1 Various AAO membranes synthesized under different anodization conditions.

Author	Electrolyte	Voltage or Current density	Structure	Note
Shuoshuo et al.[24]	0.3 M $H_2C_2O_4$	50 V~50√n V	Round	Voltage decreasing : branched channels
	0.3 M $H_2C_2O_4$	50√n V~50 V	Round	Voltage increasing : terminated channels
Zhao et al.[25]	0.8 M H_2SO_4 + 0.1 M $Al_2(SO_4)_3$	160 mA/cm^2	Six-membered rings	Interpore distance : 50 nm
Masuda et al.[16]	0.3M $H_2C_2O_4$	40 V	Rectangular	Interpore distance : 100~200 nm
	0.5 M H_3PO_4	80 V	Triangular	
Li et al.[17]	$H_2C_2O_4$ + C_2H_5OH+H_2O	100~180 V	Round	Interpore distance : 225~450 nm
	H_2SO_4 + $H_2C_2O_4$ + C_2H_5OH+H_2O	30~80 V	Round	Interpore distance : 70~140 nm
Lee et al.[18]	0.3 M $H_2C_2O_4$	100~160 V	Round	Interpore distance : 200~300 nm

After the second anodization, templates were detached from the Al film by an electrochemical treatment in perchloric acid-ethanol at 45 V at 10 ℃ or by using a $HgCl_2$ solution at room temperature. To completely remove the barrier layers, samples were then immersed in a 5 wt% phosphoric acid solution for several minutes. The samples were then rinsed with distilled water and acetone.

Table 2.2 Conventional anodization conditions for synthesis of porous AAO templates with different pore diameters and interpore distances.

Electrolyte	Concentration (M)	Voltage (V)	Temperature (℃)	Time (H)
H_2SO_4	0.3	25	10	6~12
$H_2C_2O_4$	0.3	40	17	6~12
H_3PO_4	0.3	160	2	10~12

2.2.2 Anodization of Modified AAO Templates

By the conventional anodization process, hexagonally ordered and straight pore channels are produced. In order to change the morphology, pore size, and interpore distances, we adjusted anodization conditions. We followed two-step anodization in 0.3 M H_2SO_4 or 0.3 M $H_2C_2O_4$ as described above in 2.2.1. After the first anodization, the samples were placed in a mixture solution of 5 wt% H_3PO_4 and 1.8 wt% CrO_3 at 80 ℃. A second anodization was conducted under the same conditions as the first for several hours. Subsequently, a third anodization was carried out 2~4 times increasing or decreasing voltage in various acid electrolytes. In some cases the samples were immersed in 5 wt% H_3PO_4 for 20, 40, or 60 min after the second anodization. Both

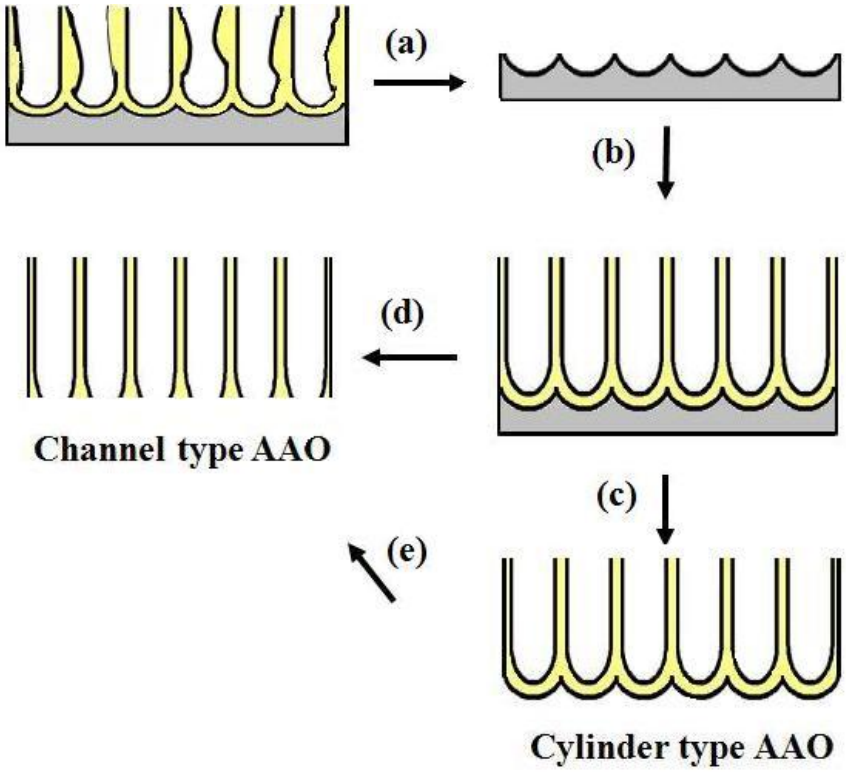

Figure 2.1 Schematic diagram of anodization processes for conventional AAO templates; (a) etching, (b) second anodization, (c) removal of Al film by using an electrochemical method or $HgCl_2$, (d) removal of Al and barrier layer by using an electrochemical method, and (e) pore opening by using 5 wt% H_3PO_4.

Al substrate and barrier layer were then removed by electrochemically in a mixture solution of $HClO_4$ and CH_3CH_2OH at 5 V higher than that the final anodization. To completely dissolve a barrier layer, the templates were immersed in 5 wt% H_3PO_4 for 20 min. All of the samples were thoroughly washed with distilled water and acetone after each step. The various morphologies of obtained pore structures are illustrated in Figure 2.2.

To confirm the structure of pore channels, metal nanowires were synthesized in alumina templates by an electrodeposition method. A thin Ag film was coated on one side of alumina templates with a Denton Desk 2 sputtering system. Electrodeposition was carried out at -0.9 mA

on a Princeton Applied Research VMP2. Ni (Nickel sulfamate-RTU) solution was commercially available from Technics Inc. A platinum wire was used as the counter electrode. More detailed electrodeposition processes will be discussed in Chapters 3 and 4.

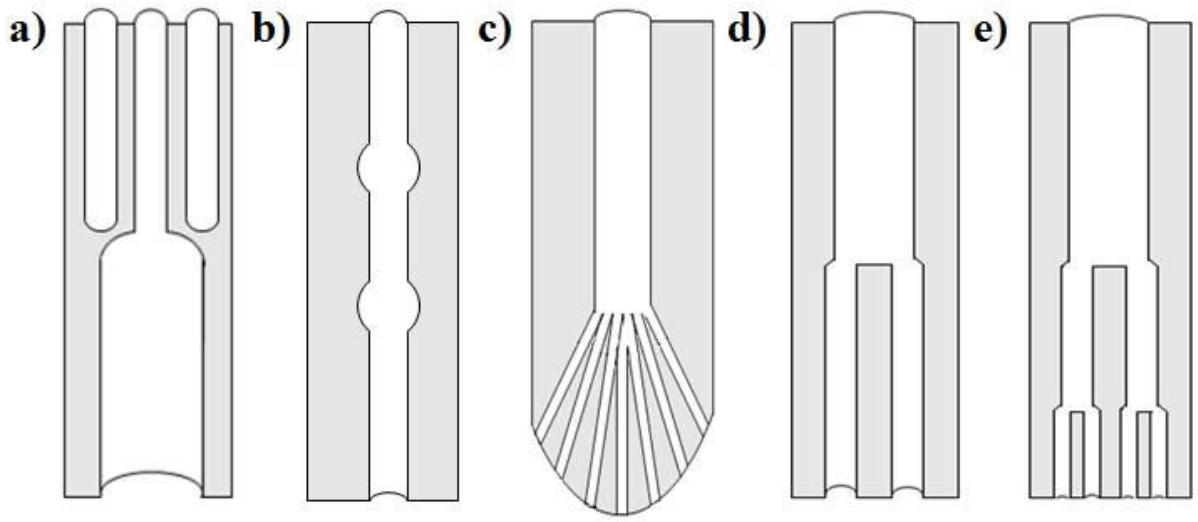

Figure 2.2 Illustration of alumina templates with various pore geometries synthesized under (a and b) the increasing and (c, d, and e) decreasing voltage.

2.2.3 Microscopic Characterization of AAO Templates

A field-emission scanning electron microscopy (FESEM, LEO 1530 VP) was employed for morphological characterization of alumina templates and metal nanowire arrays. In some cases, alumina templates were removed with a 0.1 M NaOH solution prior to analysis.

2.3 Results and Discussion

2.3.1 Conventional AAO Templates

Highly ordered porous anodic alumina templates were synthesized by conventional two-step

anodization. It should be emphasized that each step was very important to produce hexagonally ordered structures. The digital photos of Al films clearly show the differences between before and after polishing in Figure 2.3. The mirror-finished Al surface was observed after polishing process. Before the electropolishing, Al film has rough and irregular surface with thin oxide layers as shown in Figures 2.3a and 2.4. The rough surface cannot produce hexagonally ordered porous structures because the electric field is randomly distributed on the irregular pits and grooves of rough surface. However, through the electropolishing, Al film can have almost flat surface with small pits without oxide layers (Figures 2.3b and 2.5). Small pits could be seeds for pore nucleation during first anodization.

In case of first anodization, the resistivity is slowly increased with time and becomes constant after 2~3 min. At this time, the barrier layers are growing and the surface has many small parallel grooves. Al is continuously anodized and produces Al^{3+} ions at the film/electrolyte interface. Oxygen ions are also generated through dissociation of water. At the same time, Al^{3+} ions at the interface dissolve into solution and form Al_2O_3. In contrast, the oxide layers can be locally dissolved by the H^+ ions, which must occur preferentially at the pore bottom and keep the

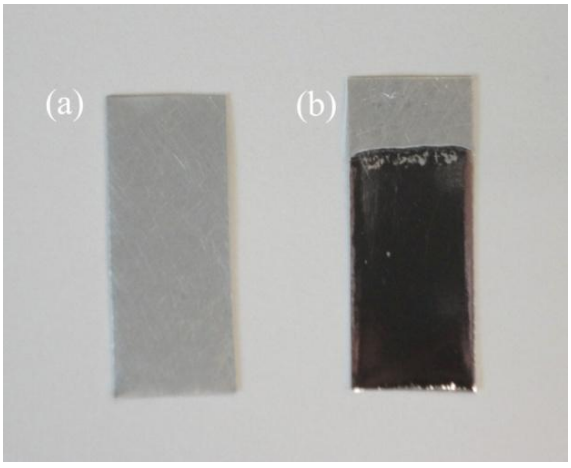

Figure 2.3 Digital photo of (a) unpolished and (b) polished Al films.

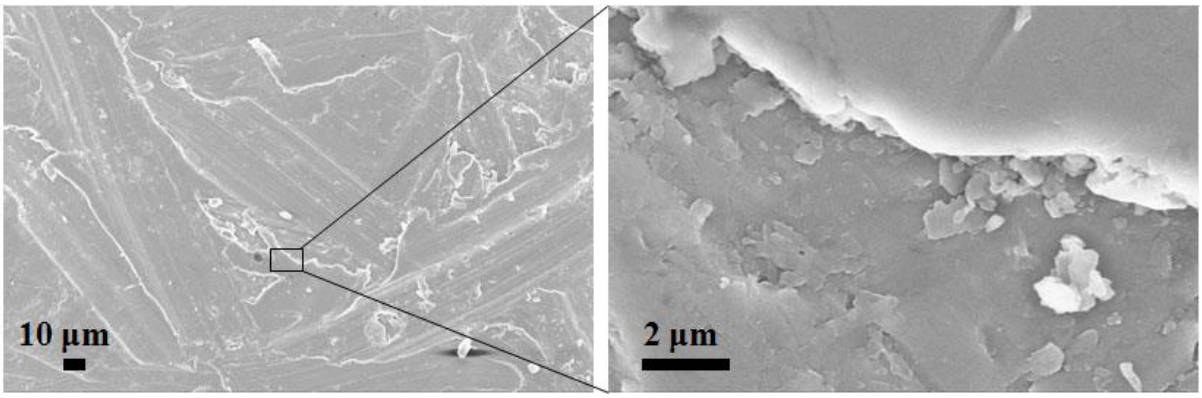

Figure 2.4 FESEM images of surface view of unpolished Al film. Images are obtained from the sample in Figure 2.3a.

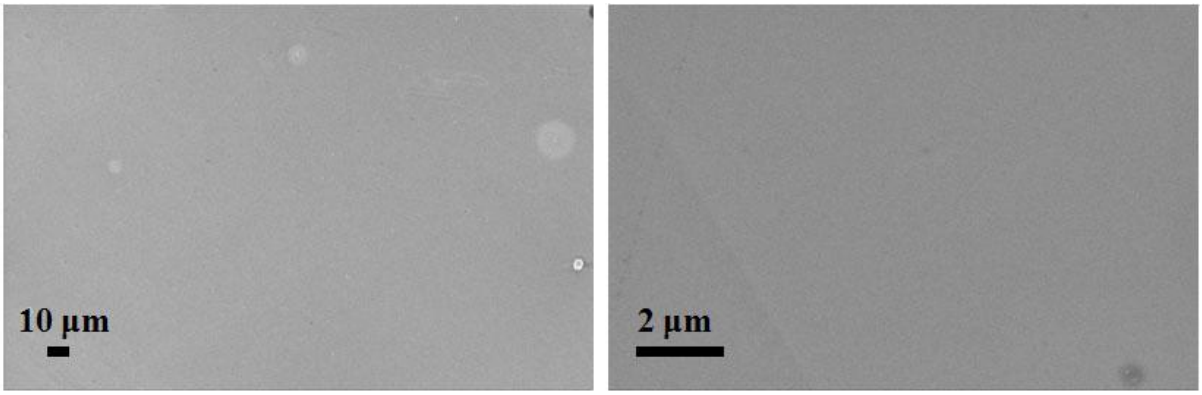

Figure 2.5 FESEM images of surface view of polished Al film. Images are obtained from the sample in Figure 2.3b.

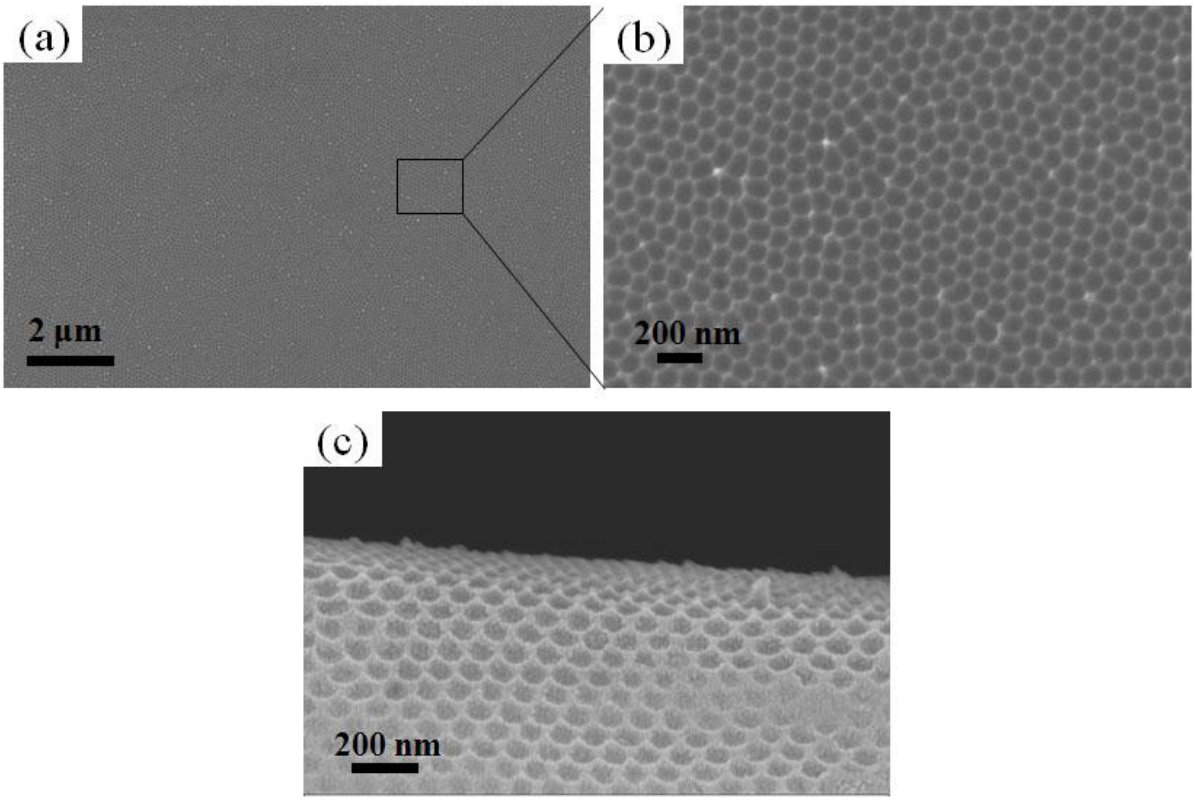

Figure 2.6 FESEM images of Al surface after etching step in a H_3PO_4-CrO_3 solution at 80 ℃. Al surface was measured at (a) low and (b) high magnification. (c) The tilted image clearly shows the hemispherical Al surface.

barrier layer thin. It occurs at the position where the electric field is highest, i.e., at the center or close to the center of the pore bottom.[11] The pore walls are uniform through their length, the barrier layers should be thin enough for the anions to penetrate into the metal/oxide interface. In other words, the local dissolution affects the surface features.

After the first anodization, the hemispherical Al surface was observed, but disordered pore arrangement was founded at the initially oxidized area. By the etching process, first oxidized layer was removed and only the hemispherical Al remained as shown in Figure 2.6.

A second anodization was carried out under the same conditions as the first anodization. At the initial stage of second anodization, the electric field can be easily and homogeneously nucleated at the center of hemispherical surface as shown in Figure 2.6. It is the reason that the resistivity was stabilized in several seconds at the initial stage of second anodization. The morphology of AAO consists of hexagonal arrays of straight long cylindrical nanopores as shown in Figures 2.7 and 2.8. The membranes synthesized in 0.3 M H_2SO_4, $H_2C_2O_4$, and H_3PO_4 show 25 nm, 40 nm, 160 nm pore diameters and 55 nm, 100 nm, and 440 nm interpore distances, respectively.

In general pore diameters and interpore distances in AAO membranes highly rely on the anodization conditions including the electrolytes, applied voltage, and current density. As we can see in Table 2.3, the pore size and interpore distance were increased with increasing voltage. Corresponding to the increasing pore sizes, the pore density is decreased from 10^{10} to 10^{8}. The growth rate of oxide layers was kept constant during anodization. In order to obtain a highly ordered cell arrangement on both the top and bottom surfaces, constant current/voltage and temperature were important. Under unstable currents or voltages, irregular pore channels with several branches were observed as shown in Figure 2.9. In addition, if the etching processes after first anodization dose not completely dissolve the oxide layers, the barrier layers still remain on the top surface of the AAO after second anodization (Figure 2.10). Especially, it happened when the barrier layer was thick, i.e. phosphoric-anodized AAO.

AAO membranes can be grown from several nanometers to over 100 μm and the thickness is dependent on the anodization time. However, AAO with nanometer scale length is hard to control and is easily broken after removal of Al film. In our system, AAO can be grown as small as 5 μm to use as a template for synthesis of nanomaterials by template-based electrodeposition. The highest thickness of membranes is about 130 μm.

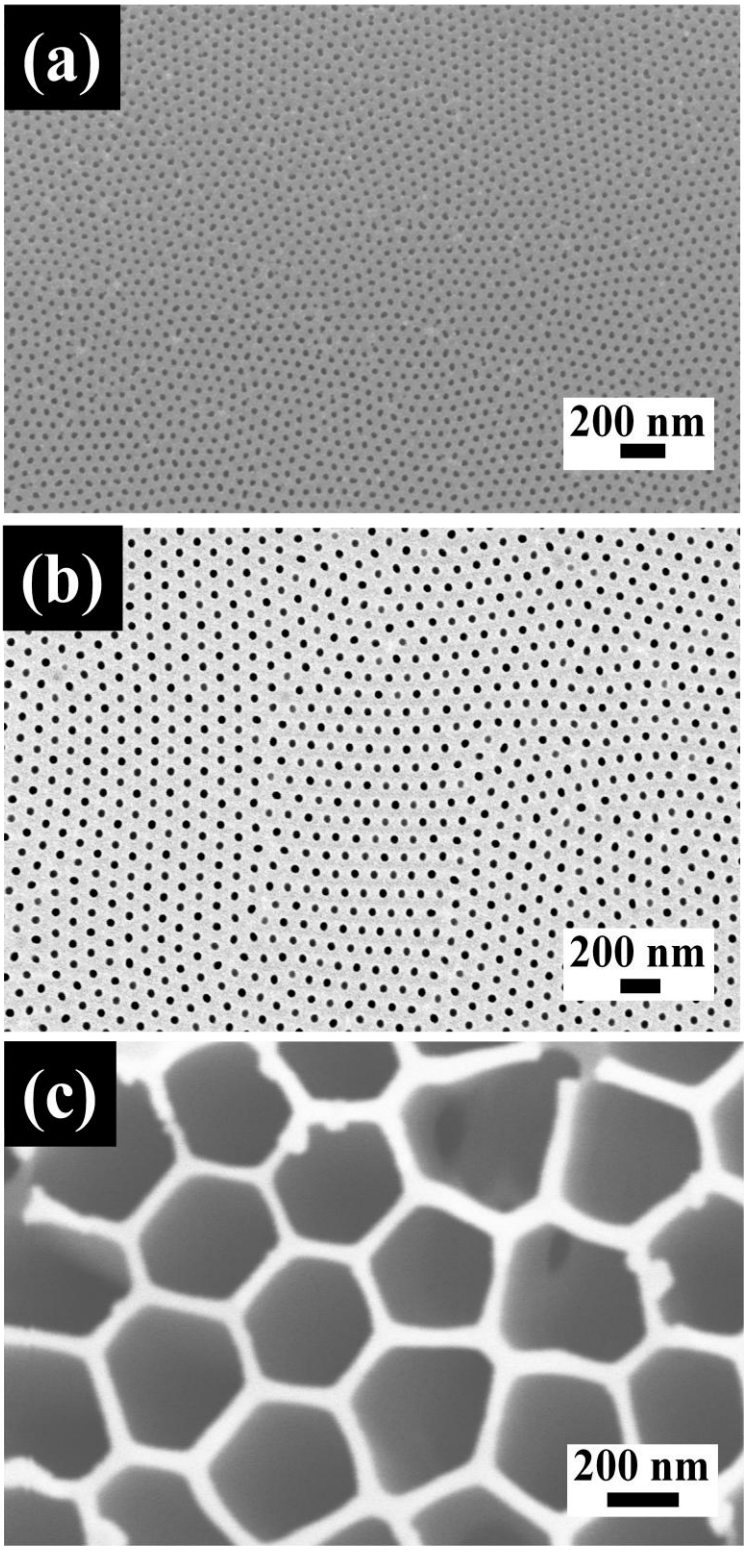

Figure 2.7 FESEM images of AAO templates synthesized in (a) 0.3 M H_2SO_4, (b) $H_2C_2O_4$, and (c) H_3PO_4.

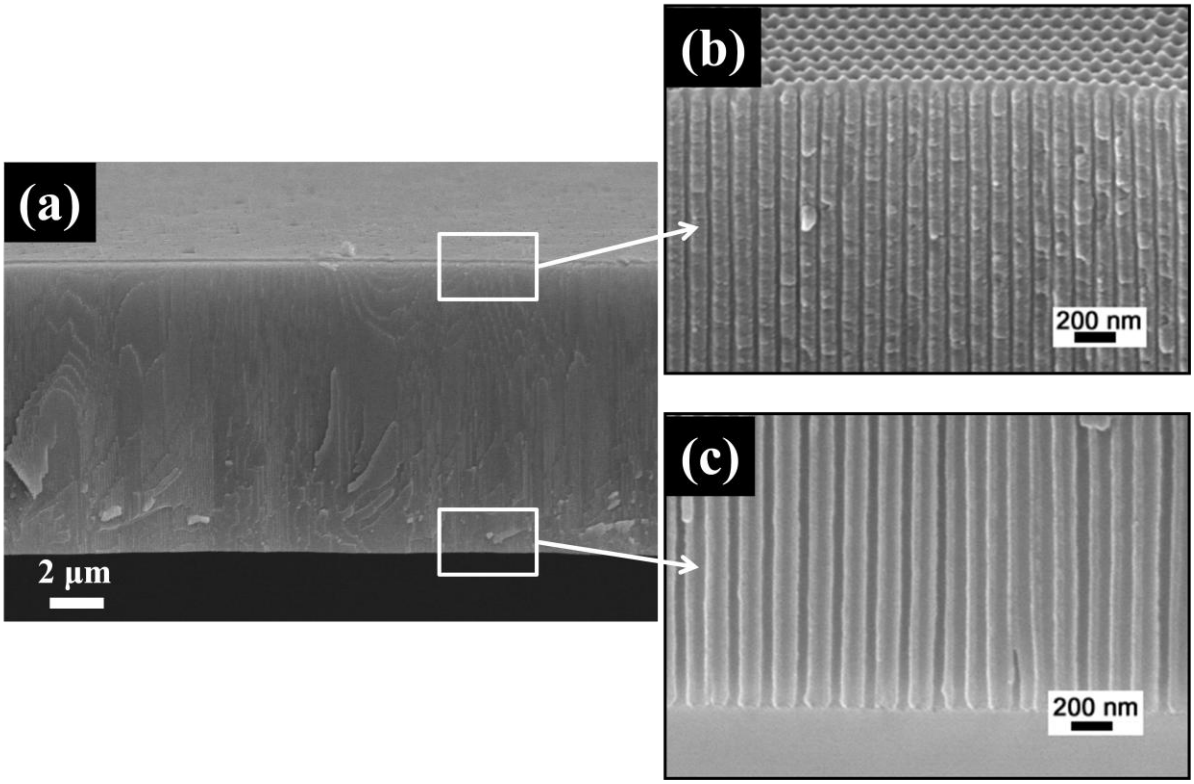

Figure 2.8 FESEM images of cross-section view of (a) channel type AAO templates with length of 10 µm synthesized in 0.3 M $H_2C_2O_4$ and its pore channels measured at (b) the top and (c) bottom area. Straight pore channels with 40 nm diameters and 100 nm interpore distances are opened from top to bottom.

Table 2.3 Structural properties of as-synthesized conventional AAO templates.

	H_2SO_4	$H_2C_2O_4$	H_3PO_4
Voltage (V)	25	40	160
Pore diameter, D_p (nm)	20	35	360
Interpore distance, D_i (nm)	55	100	440
Pore density (pore/cm^2)	4.6×10^{10}	1.15×10^{10}	5.96×10^{8}
Growth rate (µm/h)	8.3	7.5	7

From ref. 18, pore density: $(2/\sqrt{3}(D_i)^2) \times 10^{14}$

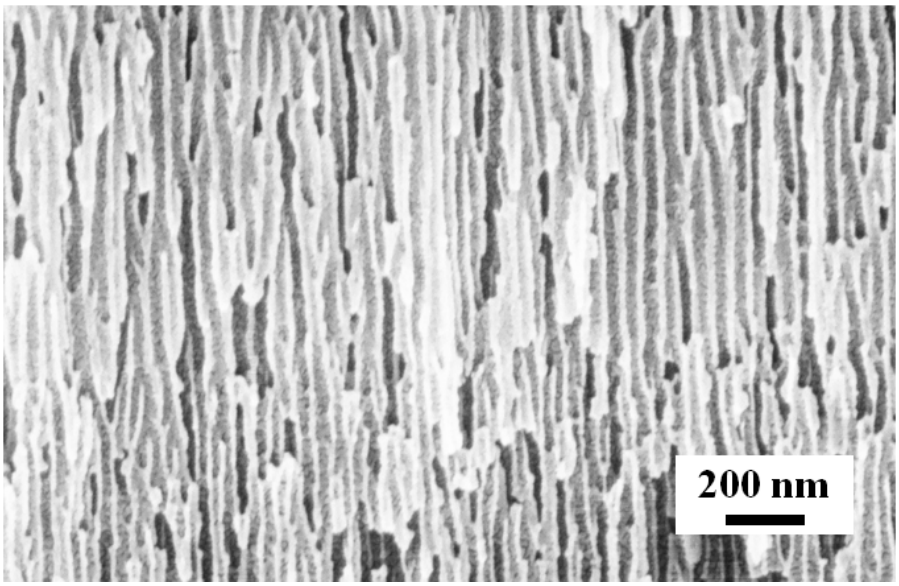

Figure 2.9 FESEM image of cross-section of AAO templates synthesized in 0.3 M $H_2C_2O_4$ at fluctuate voltage.

Figure 2.11 images represent cylinder type and channel type AAO membranes synthesized in 0.3 M $H_2C_2O_4$ at 40 V. The cylinder type AAO shows hexagonal cell structures (Figure 2.11a), where the cell size has a good linear relationship with the applied voltage. The closed pore channels also can be opened by an acid treatment using a 5 wt% H_3PO_4 solution and form channel type AAO (Figure 2.11b). The channel type AAO has no barrier layer and open pore structure from top to bottom, so it can be using as a template for electrodeposition.

The pore size can be tailored by a pore widening process using a 5 wt% H_3PO_4 solution. Figure 2.12 shows the effect of this pore widening process. The membranes synthesized in 0.3 M $H_2C_2O_4$ at 40 V for 8h was immersed in a 5 wt% H_3PO_4 solution for several minutes and shows enlarged pore structures with 40 nm, 60 nm, 80 nm, where the as-synthesized template has pore diameter of 35 nm as shown in Figure 2.7 and Table 2.3.

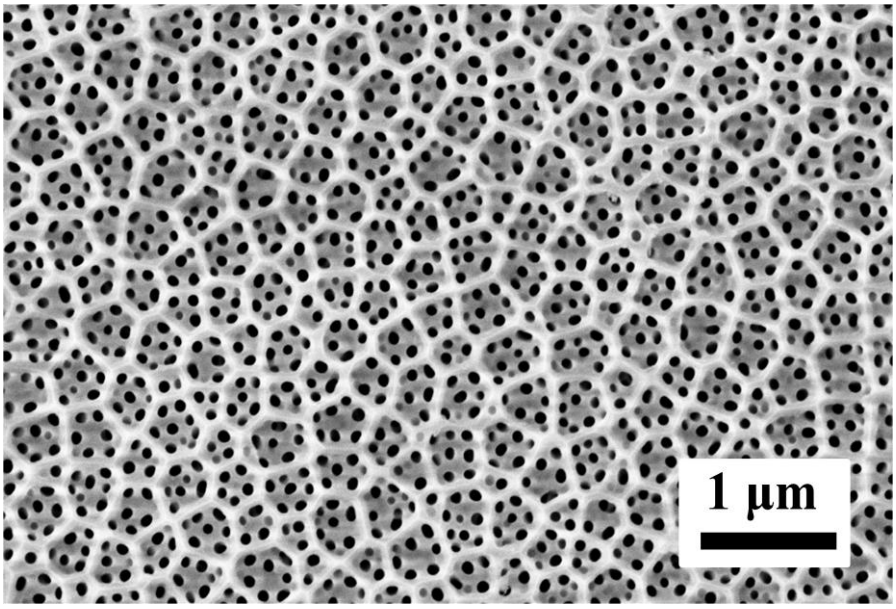

Figure 2.10 FESEM images of pore in pore structures after second anodization in 0.3 M H_3PO_4.

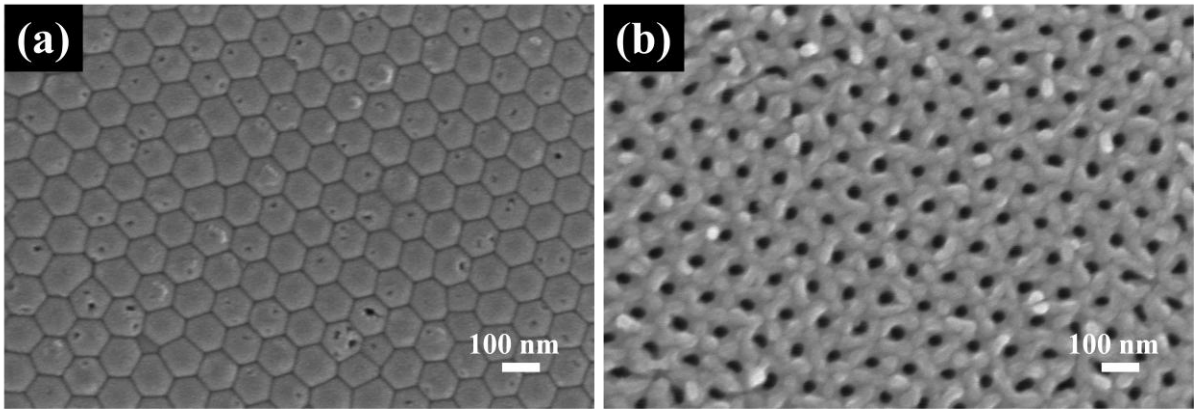

Figure 2.11 FESEM images of bottom surface view of (a) cylinder type and (b) channel type AAO synthesized in 0.3 M $H_2C_2O_4$.

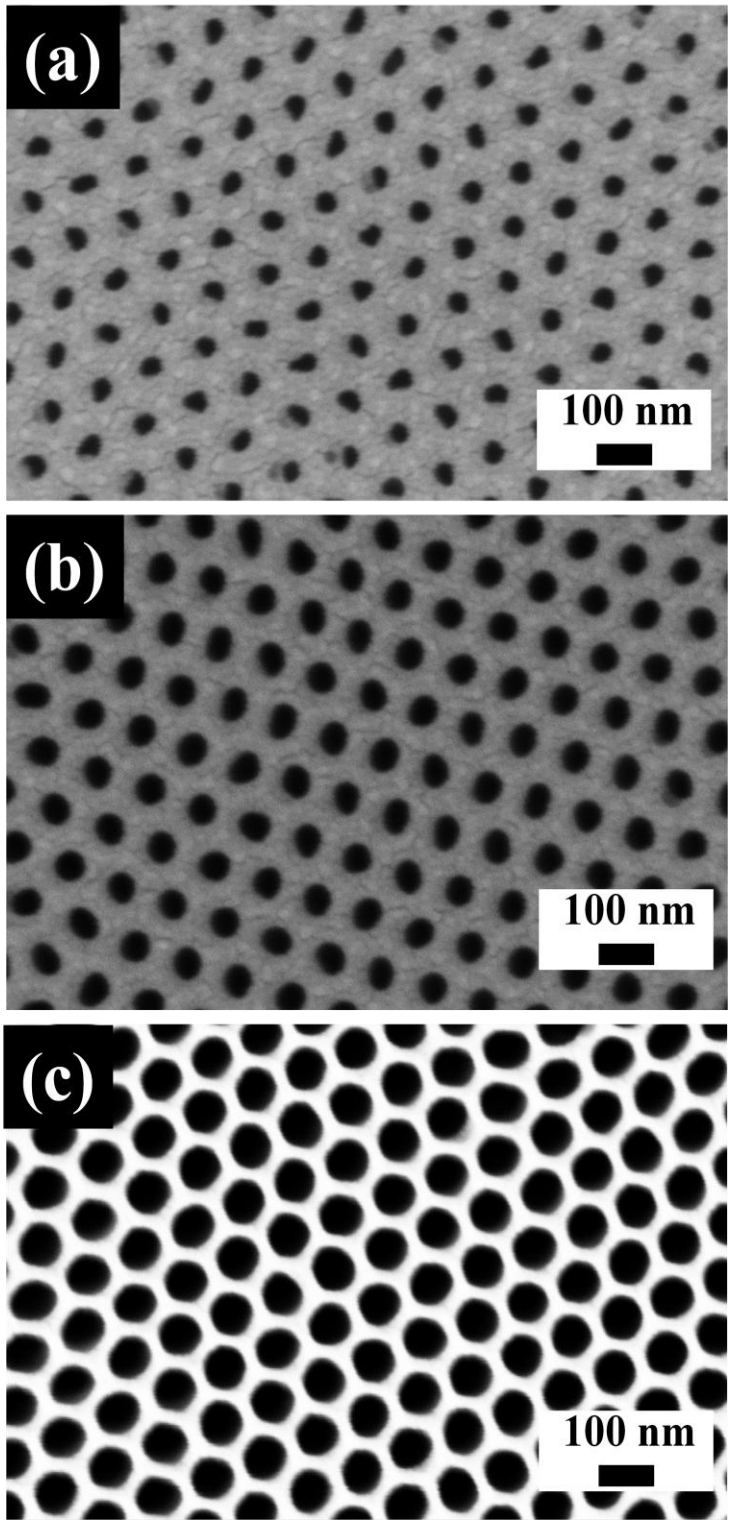

Figure 2.12 FESEM images of AAO templates with (a) 40 nm, (b) 60 nm, and (c) 80 nm pore diameters. After second anodization in 0.3 M $H_2C_2O_4$, the templates were immersed in 5 wt% H_3PO_4 for (a) 10 min, (b) 30 min, and (c) 50 min.

2.3.2 Modified AAO Templates

2.3.2.1 Increasing voltages: Selectively opened and enlarged pore structures

In order to fabricate modified pore channels, first, we increased the voltage 2 and 4 times at the third anodization step in varied electrolytes. Figure 2.13 shows alumina membranes synthesized in 0.3 M H_2SO_4 (second anodizing, 20 V) and 0.3 M $H_2C_2O_4$ (third anodizing, 80 V). The differences of pore diameter on the top (30 nm pore diameters) and bottom surfaces (90 nm pore diameters) are observed in Figure 2.13a and 2.13b. At the interface of second and third anodization, some of the pores with small diameters are terminated or continuously connected with the pores with larger diameters as seen in Figure 2.13c; pore geometry for this alumina template is corresponding to Figure 2.2a. The continuously open pores in the sulfuric-anodized region have increased their interpore distances with keeping small pore sizes. In comparison to alumina membranes synthesized by a simple two-step anodization (60 nm interpore distances), these membranes have much larger interpore distances of 220 nm. Similar results were also observed in various anodizing conditions as summarized in Table 2.4 and Figure 2.14. Especially, the alumina fabricated in oxalic-phosphoric acid provides 80 nm pore diameters and the largest interpore distances of 500 nm. Most of the templates consist of 2~4 terminated pores per one continuous pores.

The structure that contains spherical features along the straight pore channel, as described in Figure 2.2b, was created with a dramatic voltage change at 100 V in oxalic acid. The anodization that occurred at high voltage was very sensitive to small changes in stirring, temperature, current density, or voltage.[17,28,29] The abrupt increase of voltage was accompanied by a high current density. Subsequently, it affects the morphology of nanopores in templates. In general, when the applied voltages are quickly increased, an extremely high current is observed and causes cracks

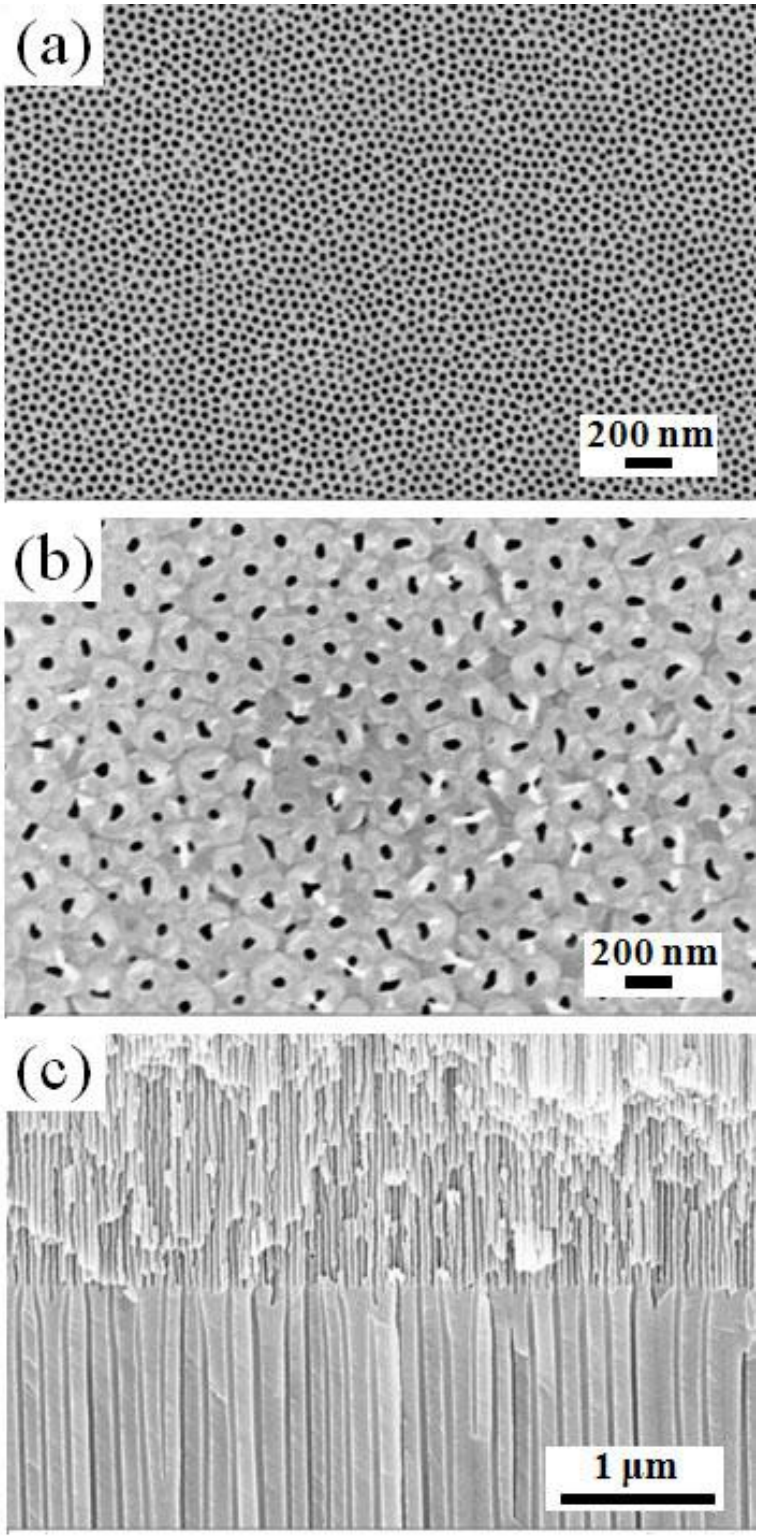

Figure 2.13 FESEM images of alumina templates with selectively opened pore structures synthesized under the increasing voltage from 20 V (sulfuric acid) to 80 V (oxalic acid); (a and b) surface view, and (c) cross-sectional view of the template.

Table 2.4 Varied pore diameters and interpore distances produced under the increasing voltage conditions.

Electrolytes (2^{nd}/3^{rd} anodizing)	Voltage (V) (2^{nd}/3^{rd} anodizing)	Pore Diameter (nm)		Interpore Distance (nm)
		Top	Bottom	
H_2SO_4 / $H_2C_2O_4$	20 / 40	30	50	55~110
H_2SO_4 / $H_2C_2O_4$	20 / 80	30	90	165~220
$H_2C_2O_4$ / $H_2C_2O_4$	40 / 80	50	90	200~300
$H_2C_2O_4$ / H_3PO_4	40 / 160	80	170	400~500

or local thickening in alumina templates due to the intense gas evolution; this is called 'burning'.[30] To produce spherical features along the channels without 'burning', high voltage (108 V) were kept only for 2 seconds, and then returned to initial state by vigorous stirring. Figure 2.15 images are obtained after Ni electrodeposition in those templates and clearly show the pore feature. Sphere feature indicated as black arrows in Figure 2.15a demonstrates the moment of voltage change. The distance between spheres can be adjusted by varying the intervals between voltage changes. The diameters of the linear and nonlinear (spherical) regions of Ni nanowires are 110 nm and 175 nm, respectively.

The physical properties of materials can be altered by modifying their shape, size, or ordering. The template-based method offers a cost effective method to control size and ordering by changing pore structures in templates. The development of anodization of metal films can further expand the range of uses of porous templates in the preparation of technologically significant nanomaterials.

As seen in Figures 2.13 and 2.15, we have produced modified alumina templates by changing the anodizing voltage. Both the pore diameters and the interpore distances were strongly

influenced by the applied voltage used for anodization. When an anodizing voltage is increased by sequential anodization, the electric field is redistributed on the barrier layer and metal surface. To reduce stress on the surface, the field is concentrated on selected pore channels, which have a thinner barrier layer relative to neighboring pores. The thinner barrier layer supports continued development of the selected pores. However, the neighboring pores which have comparably thicker barrier layers are prevented from further anodization. The number of terminated pores is increased with increasing voltage because the range of nucleated area becomes larger.

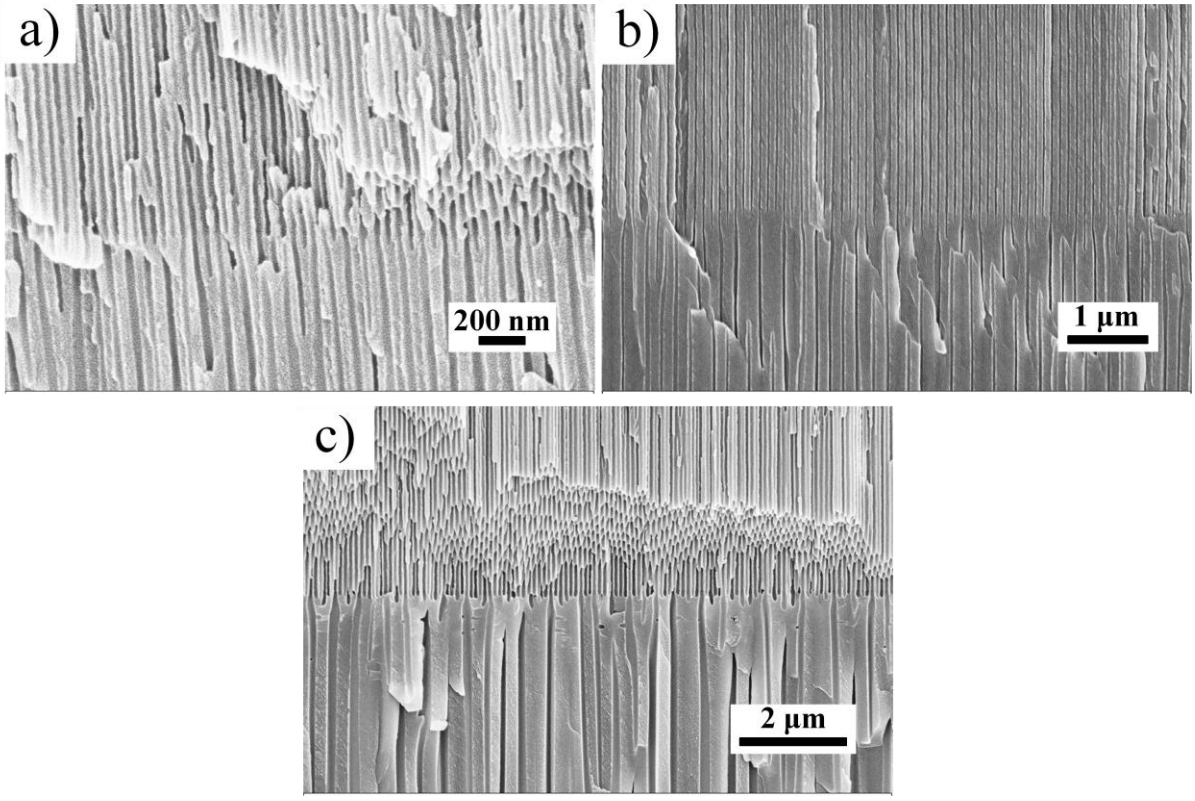

Figure 2.14 FESEM images of the alumina template with selectively opened pore structures synthesized under the increasing voltage; (a) 20 V (0.3 M sulfuric acid, 10 ℃) to 40 V (0.3 M oxalic acid, 17 ℃), (b) 40 V (0.3 M oxalic acid, 17 ℃) to 80 V (0.3 M oxalic acid, 17 ℃), and (c) 40 V (0.3 M oxalic acid, 17 ℃) to 160 V (0.3 M phosphoric acid, 5 ℃).

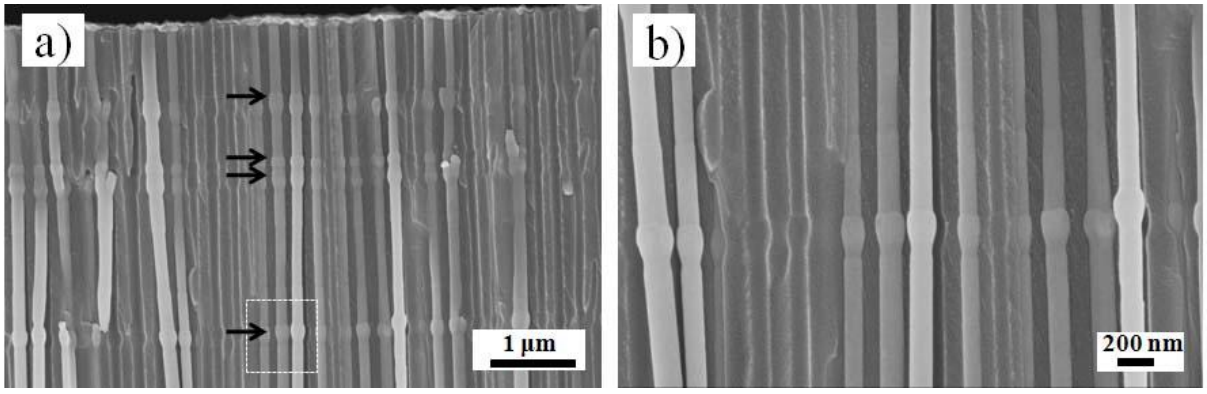

Figure 2.15 (a) FESEM images of Ni nanowires in the alumina template with spherical feature along the straight pore channels. The template was synthesized under the increasing voltage in 0.3 M oxalic acid. (b) Magnified FESEM image corresponding to the white square in (a).

2.3.2.2 Decreasing voltages: Arch-shaped and branched pore structures

In contrast, when the voltage is decreased after second anodization, one pore channel is multiplied into a number of small pore channels as shown in Figures 2.2c-d. Additionally, the alumina templates show various pore geometries such as arch-shaped, tree-like, and branched pores. Figure 2.16 images show the cross-section view of alumina templates with arch-shaped (a, b), tree-like (c, d), and branched (e, f) pores. Even though the templates were synthesized under the equal anodization conditions; 0.3 M oxalic acid at 40 V (second anodizing) for 2 h and 20 V (third anodizing) for 3 h, three samples provide different pore geometries because of varied time of acid treatment after a second anodization. In general, researchers used phosphoric acid to enlarge the pore diameters of alumina membranes or to remove barrier layer after detaching process. In our case, a 5 wt % phosphoric acid solution was employed to decrease the thickness of barrier layers after a second anodization. The thickness of barrier layers was reduced as a function of the acid treatments (Figure 2.17) and it was strongly influenced in the third anodization as described below.

A directly processed third anodization without the acid treatment (A_t=0 min) produces an arch-shaped pore geometry as seen in Figures 2.16a and 2.16b. Tree-like and branched pores were synthesized after acid treatments for 20 min, 40 min, respectively. The oxide layers synthesized by second and third anodization were marked as capital 'A' and 'B' in Figures 2.16a, 2.16c, and 2.16e. 'A' regions of three samples in Figure 2.16 show 15 μm length and a smooth surface with enlarged pore diameters due to the acid treatment. However, as seen in Figure 2.16, 'B' regions synthesized at the third anodization show different length (L_b) and varied distances of branches (D_a) in Table 2.5. Furthermore, the differences of 'B' regions are observed in the surface morphology (Figure 2.18). The irregular and rough surfaces were measured at 'B' regions of the arch-shaped alumina. After the acid treatments, however, the surface of the 'B' region becomes smooth. Table 2.5 is the comparison of structural properties of three alumina membranes corresponding to the Figures 2.16 and 2.17. The thickness of barrier layer (T_b) was reduced about 10 nm and the pore diameter (D_p) was enlarged from 38 nm to 62 nm after 40 min acid treatments. When the barrier layer is thick, the distance of branches becomes longer and the oxide layer grows slowly during the third anodization. However, the alumina with thinner barrier layers shows the fastest growth rate (G_r) of 2 μm/h, where the growth rate of branched alumina is 4 times faster than arch-shaped alumina templates.

The pore diameter of branched nanopores can be controlled by adjusting the voltage. Figure 2.19 shows the top and cross-sectional view of alumina synthesized with decreasing voltage; 80 V (second anodization) for 30 min and 40 V (third anodization) for 2 h in 0.3 M oxalic acid. The samples were also immersed in a phosphoric acid solution for 60 min after the second anodization. The branched pores consist of different pore diameters of 90 nm and 50 nm on the top and bottom, respectively (Figures 2.19a and 2.19b). Several branches are starting from one

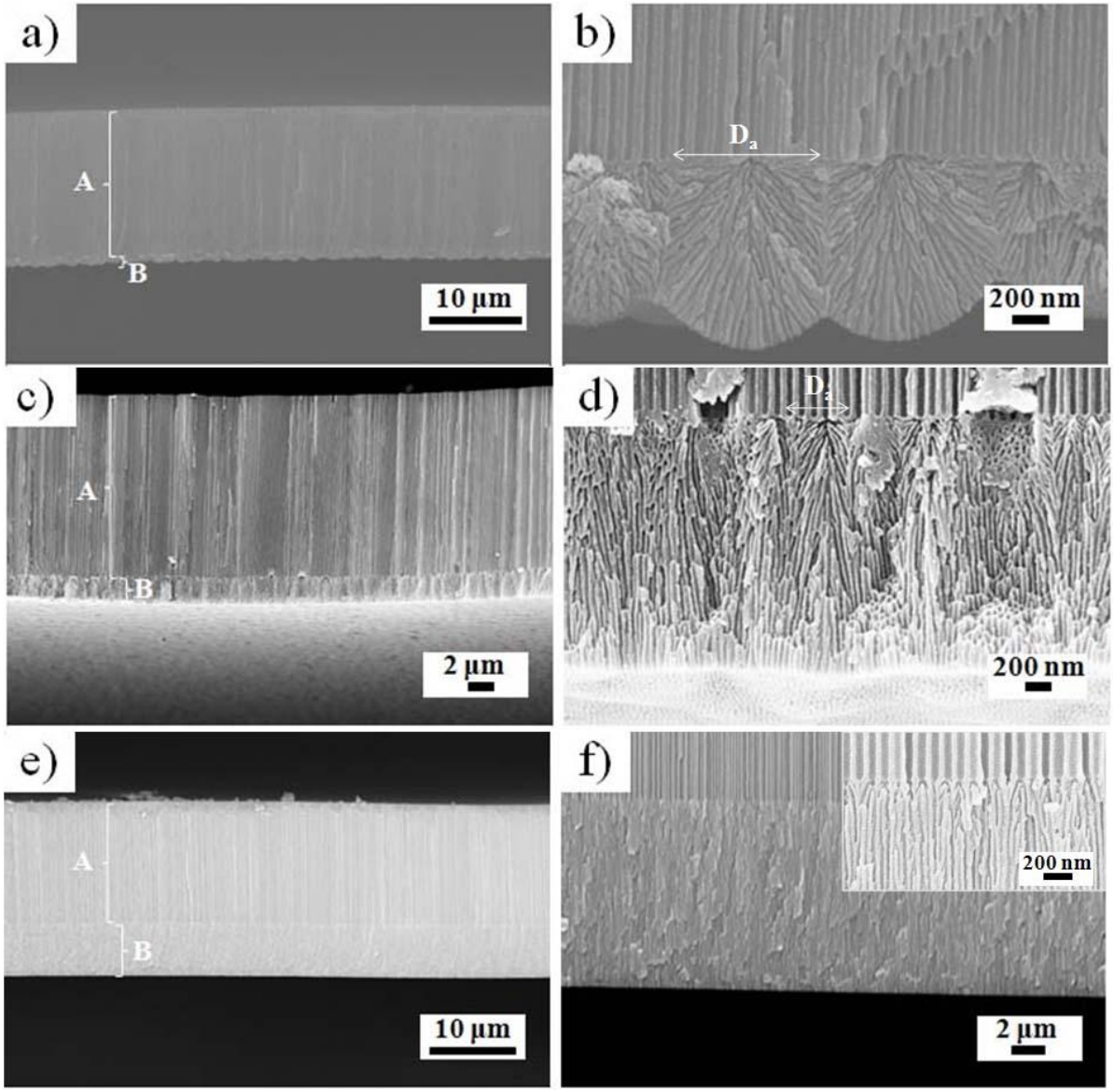

Figure 2.16 FESEM images of cross-sectional view of alumina templates with (a and b) arch-shaped, (c and d) tree-like, and (e and f) branched pore geometries which are synthesized under the decreasing voltage. Capital 'A' and 'B' marked in image (a, c, and e) are indicating oxide layers which are synthesized at second and third anodization processes. (b, d, and f) Images are magnified from the interface between 'A' and 'B'. D_a is a distance of branched pores.

Table 2.5 Structural properties of alumina templates with various pore geometries. The thickness of barrier layer (T_b) and pore diameters (D_p) observed before a third anodization are corresponding to Figure 2.17.

	Arch-shaped	Tree-like	Branched
A_t (min)	0	20	40
T_b (nm)	52	48	43
D_p (nm)	38	53	62
D_a (nm)	890	400	70
L_b (μm)	1.5	2.1	6.0
G_r (μm/h)	0.5	0.7	2

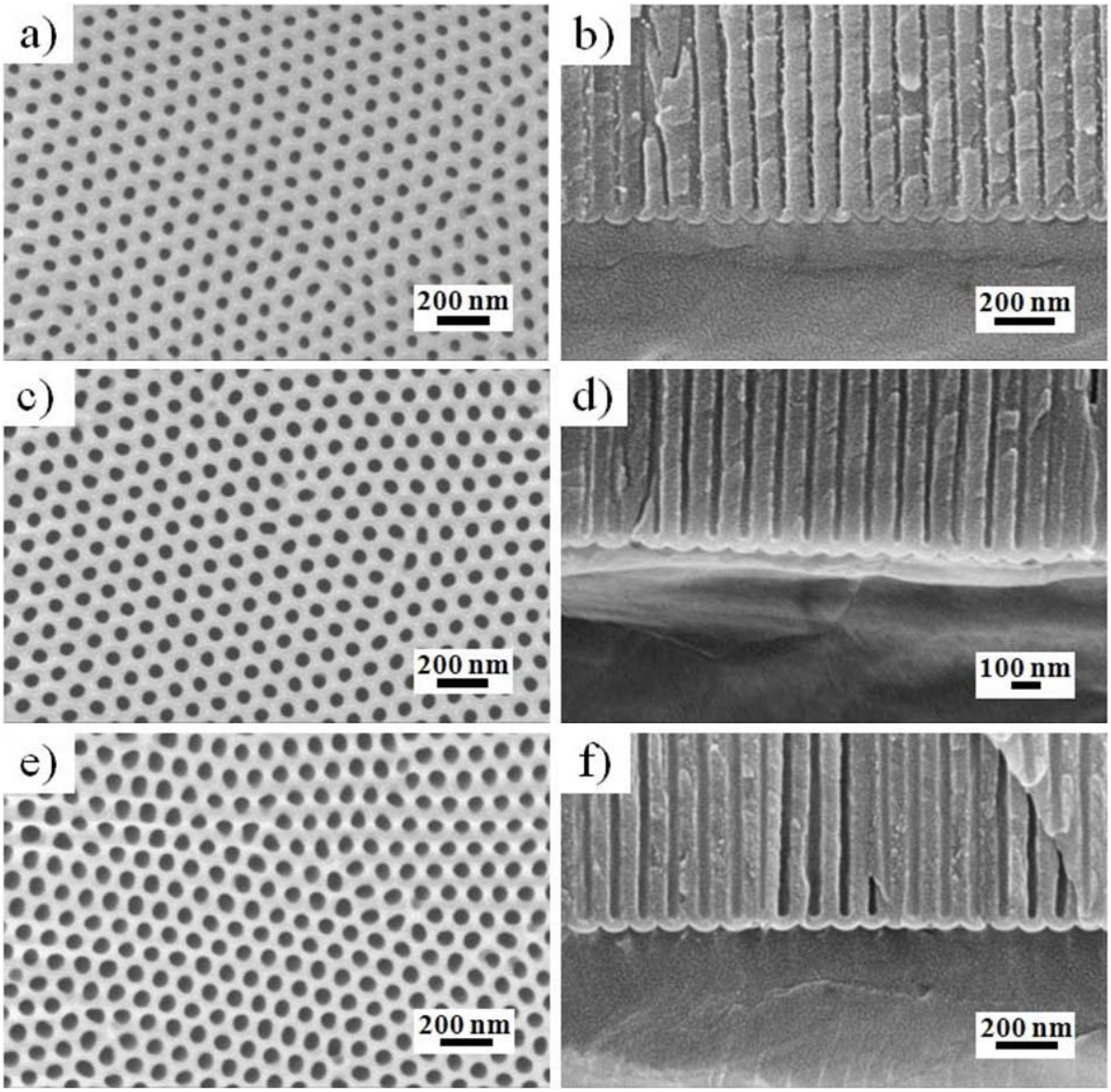

Figure 2.17 FESEM images of surface and cross-sectional view of alumina templates; (a and b) no acid treatments, (b and c) 20 min acid treatments, (e and f) 40 min acid treatments after second anodization processes at 40 V in 0.3 M oxalic acid.

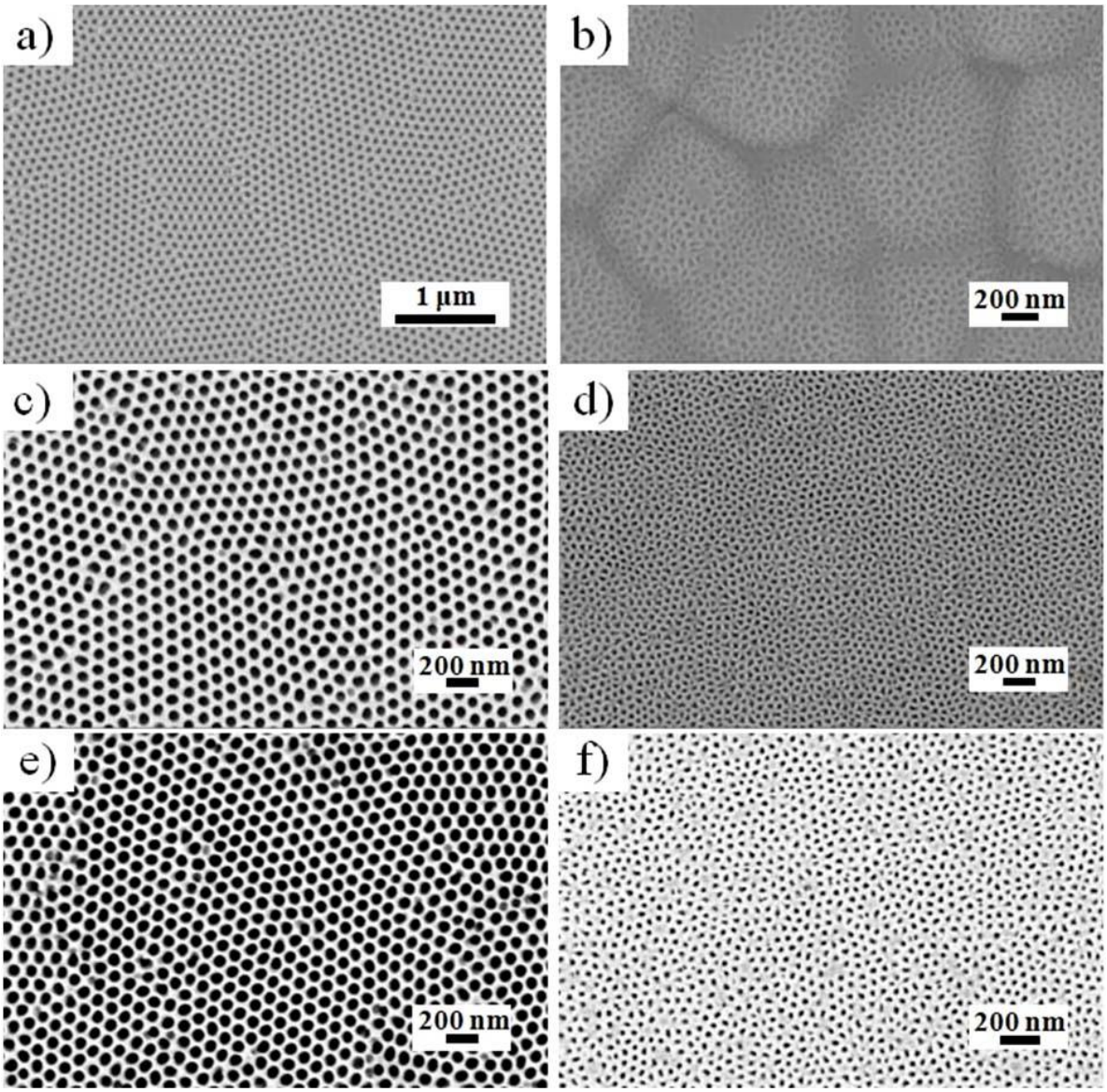

Figure 2.18 FESEM images of top and bottom surface view of alumina templates with various pore geometries; (a and b) arch-shaped, (c and d) tree-like, and (e and f) branched alumina templates. When we compare the pore diameters in Figures 2.18 (a, c, and e) with that in Figure 2.17, the pore diameters in Figure 2.18 were increased because of the additional 20 min acid treatments after a third anodization. The pore diameters of (a), (b), and (c) are 60 nm, 70 nm, and 80 nm, respectively.

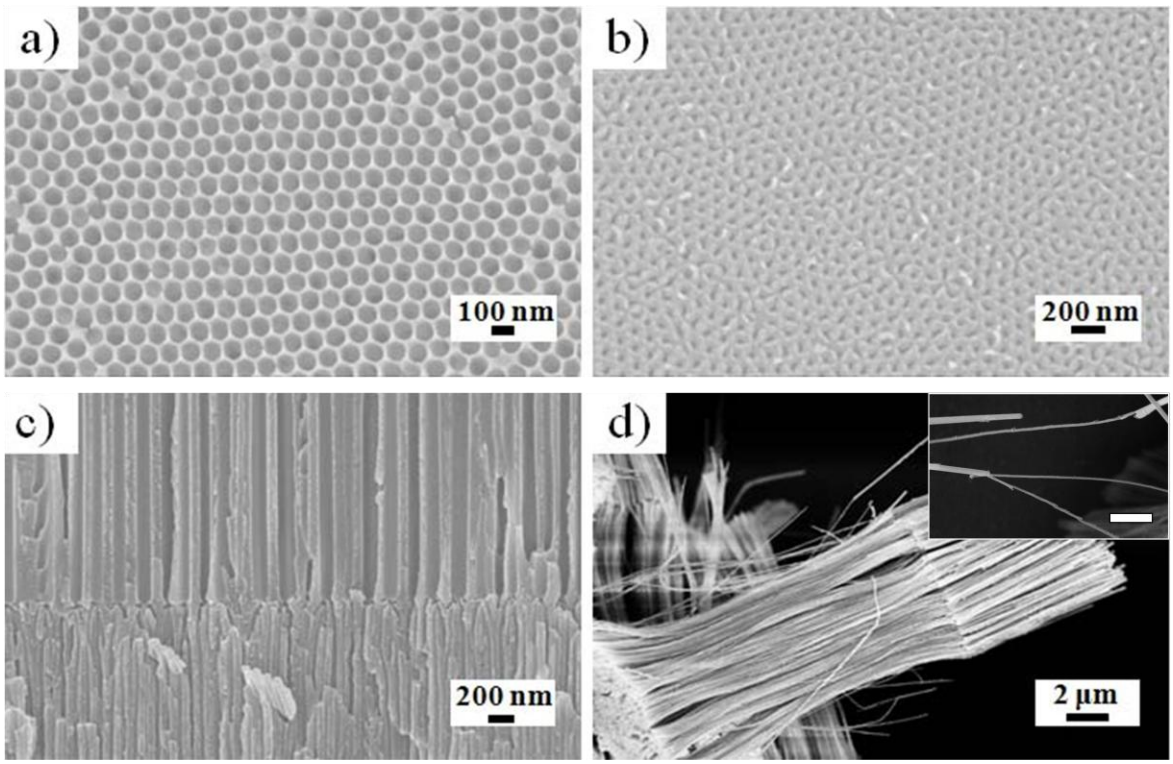

Figure 2.19 FESEM images of the alumina template with branched pore structures synthesized under the decreasing voltage from 80 V (second anodization) to 40 V (third anodization) in oxalic acid; (a) top and (b) bottom surface view, and (c) cross-sectional view of the template. (d) Ni nanowires synthesized in the template. Inset shows the magnified image of branched Ni nanowires (scale bar is 1 μm).

stem, but only 1 or 2 branches were active when the pores were used for growing nanowires by an electrodeposition technique as shown in Figures 2.19c and 2.19d.

Figure 2.20 images show a 2+2 branched pore structure as illustrated in Figure 2.2e. The two branches arising from the pores synthesized during a previous anodization were successfully fabricated under the reducing voltage; capital ‘A, B, and C’ regions in Figure 2.20e were synthesized at 60 V, 42 V, and 30 V in 0.3 M oxalic acid, separately. The sample was also immersed in a phosphoric acid solution for 20 min after each anodization process. Surface view of ‘A’ and ‘C’ regions demonstrates well-ordered hexagonal pore structures and distinct pore

diameters. The pore diameter of alumina templates has a good relationship with the applied voltages, so the top surface (Figure 2.20a) shows larger diameter than the bottom surface (Figure 2.20b). Also, the interfaces between ‘A’ and ‘B’ (Figure 2.20c), or ‘B’ and ‘C’ (Figure 2.20d) clearly confirm their branched pore structures. In order to see detailed pore structures, the metal nanowires with two branches were synthesized in ‘A’ and ‘B’ regions of the templates. Figure 2.20f image was obtained after dissolving of alumina templates using a NaOH solution.

Unlike the anodization that occurred on the increasing voltage (Figure 2.13), the thickness of barrier layer predominantly influenced the anodization of the reducing voltage. Figure 2.21a illustrates the relative electric field strength under the different thicknesses of barrier layer. The reduced anodization voltage is difficult to penetrate an electric field under the thick barrier layer to grow continuous oxide layers. According to theory, the electric field strength (E) is inversely proportional to the thickness of barrier layer.[28] When the barrier layer is thicker, the electric field strength becomes smaller even though we applied the same voltage. Therefore, the pores with a thinner barrier layer than their neighboring pores may nucleate and grow oxide layers more rapidly. On the other hand, the pore size and interpore distance are decreased due to the reduced voltages (Figure 2.21b). It produced multiplied pore channels with various pore geometries. The other possible influences on the various pore structures include defected areas or domain structures. Although hexagonally ordered pores are growing affectively on the Al surface, domain structures are still observed in alumina membranes, where the defected pores concentrated on the boundary of domains. The electric field strength then will not always be identical.

When the barrier layer is thick as shown in Figure 2.17a, an electric field can only be nucleated at the pore that has the thinner barrier layer and longer pore channel in comparison

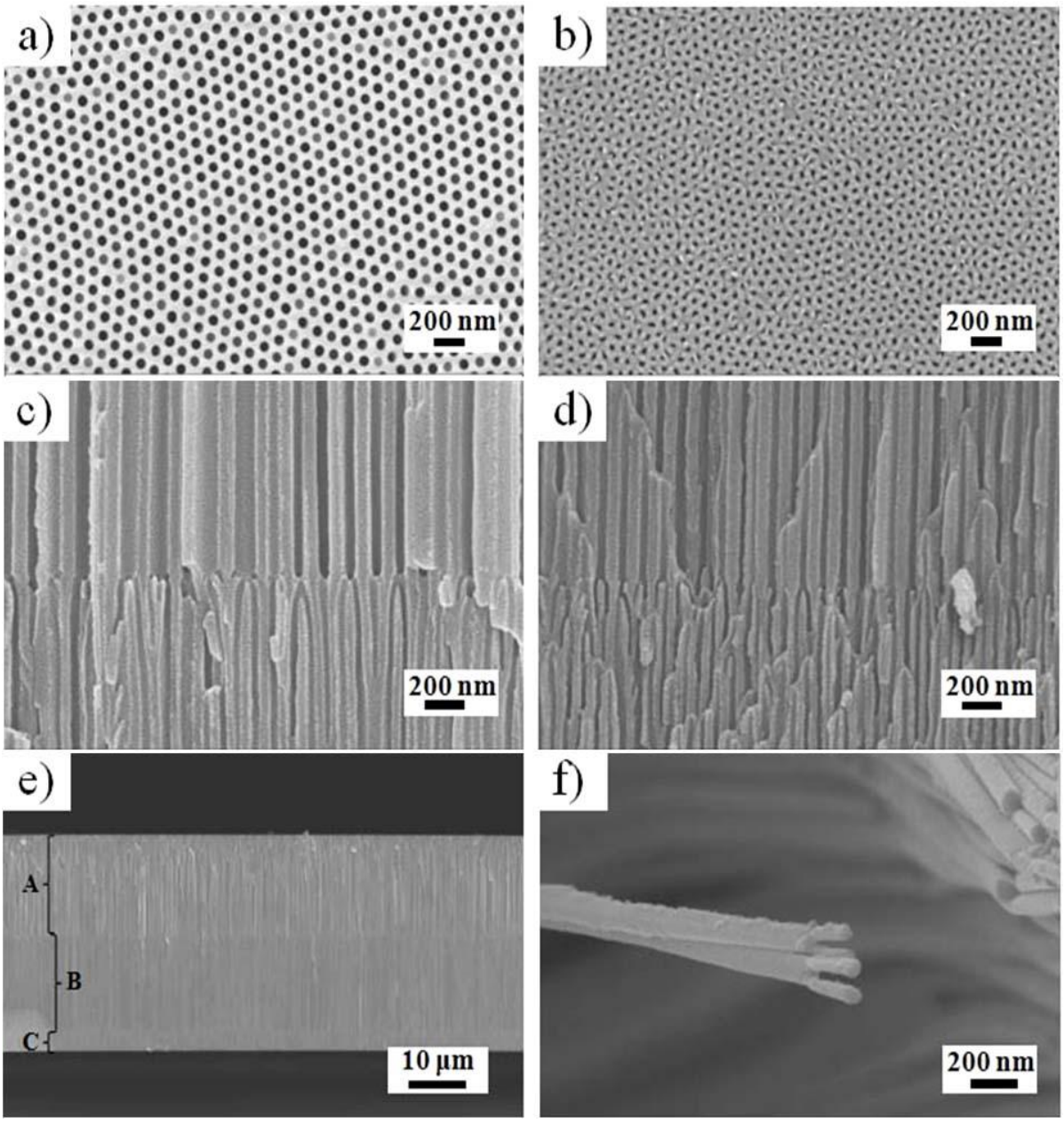

Figure 2.20 FESEM images of the 2+2 branched alumina template which is synthesized under the decreasing voltage (60, 42, and 30 V in 0.3 M oxalic acid); (a) top and (b) bottom surface and (c, d, and e) cross-sectional view. 'A', 'B' and 'C' marked in image (e) are indicating oxide layers which are synthesized at 60 V (second), 42 V (third) and 30 V (forth anodization), respectively. (c and d) Images are magnified from the interfaces between two regions; (c) A-B interface and (d) B-C interface. (f) FESEM image of branched Ni nanowires synthesized in the template.

to neighboring pores. In an initial anodization state, the nucleated pores can grow in all directions, even parallel to the Al surface. This is because other pores are prevented in the third anodization and so no more competitive growth occurs. The pores grown in a parallel direction finally meet other pores of neighboring arch-shaped pore arrays, as the Al was completely exhausted by a continuing anodization.

If the barrier layer is thin enough to penetrate the electric field, similar electric field will occur in all pore channels, and then the anodization can happen simultaneously. Because of a strong repulsive force between pores during oxide layer growth, all of the pores will grow perpendicular to the aluminum surface.[31] The growth rate of alumina templates is dependent on the migration of Al^{3+} and O^{2-} ions at the interface between the aluminum and electrolytes. When the nanopores are growing straight (perpendicular to the aluminum surface), the resistance of the migration of ion species is minimized.[32] This is the reason that the growth rate of the branched membrane is much higher than that of arch-shaped or tree-like alumina membranes.

2.4 Conclusions

In this chapter, we describe the synthesis of porous anodic aluminum oxide templates with hexagonal arrays of straight long cylinder nanopores by a conventional two-step anodization. In addition the pore diameters and interpore distances are readily controlled by appropriately changing the anodization conditions and pore widening time. We also successfully synthesized alumina templates with various pore geometries under adjusted anodization conditions such as increasing or decreasing voltage. The anodization conducted under the increasing voltage created selectively opened pore structures with enlarged pore diameters, where the interpore distances increased with varying the increased voltage. Also, pore sizes and interpore distances were well

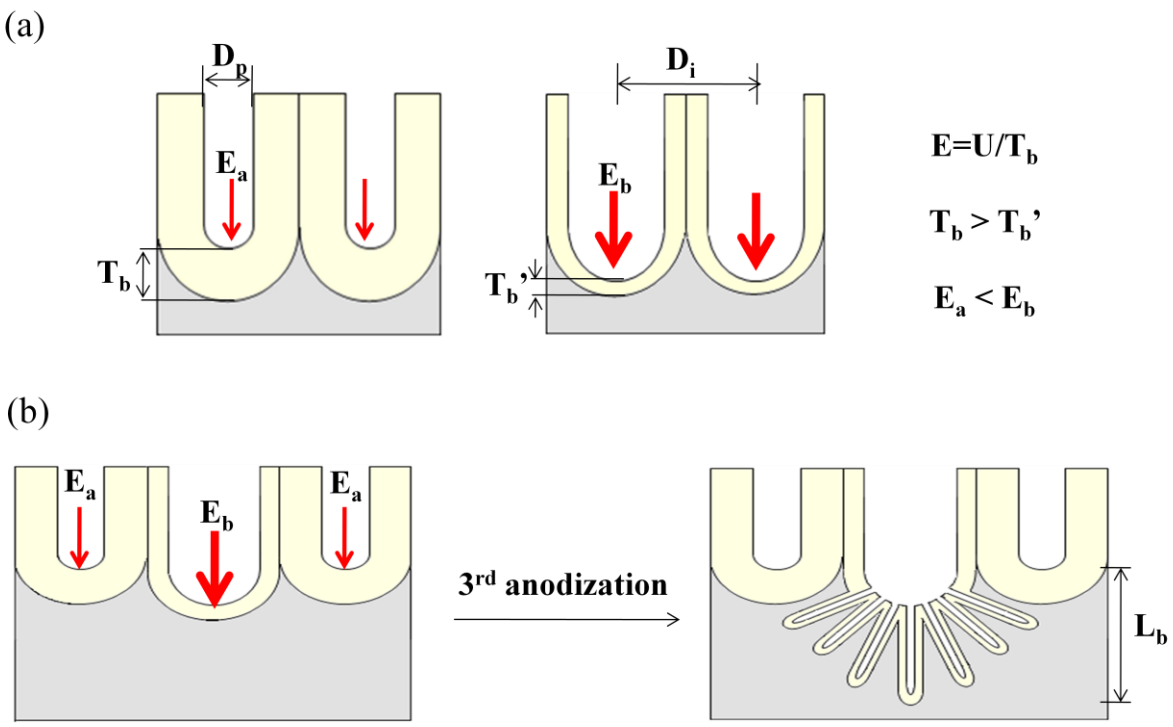

Figure 2.21 (a) Schematic illustration of the relative electric field strength (E) under the different thickness of barrier layer (T_b). (b) Schematic illustration of the third anodization occurred at the reduced voltage. U is an applied voltage.

controlled by third anodization conditions. However, branched pore structures with smaller pore diameters and reduced interpore distances were fabricated after an additional anodization process under the decreasing voltage condition. From our results we know that the applied voltage highly affects the growth of pore structures such as pore diameters, interpore distances, and pore geometries as well. In the case of decreasing voltage, the electric field strength was adjustable by changing a thickness of the barrier layer. We expect that nanomaterials with various morphologies can be synthesized by using these templates and their physical and chemical properties can be controllable for future applications in magnetic systems, catalysts, sensor devices, etc.

2.5 References

1. H. Masuda and K. Fukuda, *Science*, **1995**, *268*, 1466.
2. Xiaohu Huang, Liang Li, Xuan Luo, Xiaoguang Zhu and Guanghai Li, *J. Phys. Chem. C* **2008**, *112*, 1468.
3. Jin-Hee Lim, Weon-Sik Chae, Hee-Ok Lee, Leszek Malkinski, Seong-Gi Min, John B. Wiley, Jong-Ho Jun, Sung-Kyung Ham and Jin-Seung Jung, *J. Appl. Phys.*, **2010**, *107*, 09A334.
4. Liang Li, Shusheng Pan, Xincun Dou, Yonggang Zhu, Xiaohu Huang, Youwen Yang, Guanghai Li and Lide Zhang, *J. Phys. Chem. C* **2007**, *111*, 7288.
5. Jin-Hee Lim and John B. Wiley, *Mater. Res. Soc. Symp. Proc*., **2009**, *1142*, JJ0531.
6. Michal Lahav, Emily A. Weiss, Qiaobing Xu, and George M. Whitesides, *Nano Lett*., **2006**, *6*, 2166.
7. Brinda B. Lakshmi, Peter K. Dorhout, and Charles R. Martin, *Chem. Mater*., **1997**, *9*, 857.
8. Joon-rak Choi, Sang Jun Oh, Honglyoul Ju, and Jinwoo Cheon, *Nano Lett*., **2005**, *5*, 2179.
9. Kristina Pitzschel, Josep M. Montero Moreno, Juan Escrig, Ole Albrecht, Kornelius Niel sch, and Julien Bachmann, *ACS Nano*, **2009**, *3*, 3463.
10. Feng Li, Jibao He, Weilie L. Zhou, and John B. Wiley, *J. Am. Chem. Soc.*, **2003**, *125*, 16166.
11. Feiyue Li, Lan Zhang, and Robert M. Metzger, *Chem. Mater*., **1998**, *10*, 2470.
12. Ampere A Tseng, 'Nanofabrication' published in 2008 by the World Scientific Publishing Co. Pte. Ltd.
13. Jerrod E. Houser, and Kurt R. Hebert, *Nat. Mater*., **2009**, *8*, 415.
14. Hidetaka Asoh, Kazuyuki Nishio, Masashi Nakao, Toshiaki Tamamura, and Hideki Masuda, *J. Electrochem. Soc*., **2001**, *148*, B152.
15. Kornelius Nielsch, Jinsub Choi, Kathrin Schwirn, Ralf B. Wehrspohn, and Ulrich Gösele, *Nano Lett*., **2002**, *2*, 677.
16. Hideki Masuda, Hidetaka Asoh, Mitsuo Watanabe, Kazuyuki Nishio, Masashi Nakao, and Toshiaki Tamamura, *Adv. Mater*., **2001**, *13*, 189.
17. Y. Li, Z. Y. Ling, S. S. Chen, and J. C. Wang, *Nanotechnology*, **2008**, *19*, 225604.
18. Woo Lee, Ran Ji, Ulrich Gösele, and Kornelius Nielsch, *Nat. Mater*., **2006**, *5*, 741.
19. Jin-Seung Jung, Eun-Mee Kim, Weon-Sik Chae, Leszek M. Malkinski, Jin-Hee Lim, Charles O'Connor and Jong-Ho Jun, *Bull. Korean Chem. Soc*., **2008**, *29*, 2169.
20. Thelese R. B. Foong, Alan Sellinger and Xiao Hu, *ACS Nano*, **2008**, *2*, 2250.
21. S. Z. Chu, K. Wada, S. Inoue, and S. Todoroki, *J. Electrochem. Soc*., **2002**, *149*, B321.
22. Tanu Suryadi Kustandi, Victory Donald Samper, Wan Sing Ng, Ai Shing Chong, and Han Gao, *J. Micromech. Microeng*., **2007**, *17*, N75.
23. T. Gao, G. Meng, J. Zhang, S. Sun and L. Zhang, *Appl. Phys. A* **2002**, *74*, 403.
24. C. Shuoshuo, L. Zhiyuan, H. Xing and L. Yi, *J. Mater. Chem*., **2009**, *19*, 5717.
25. S. Zhao, K. Chan, A. Yelon and T. Veres, *Adv. Mater*., **2007**, *19*, 3004.
26. Y. B. Li, M. J. Zhang, and L. Ma, *Appl. Phys. Lett.*, **2007**, *91*, 073109.
27. W. Lee, R. Scholz and U. Gösele, *Nano Lett*., **2008**, *8*, 2155.
28. Woo Lee, Jae-Cheon Kim, and Ulrich Gösele, *Adv. Funct. Mater*., **2010**, *20*, 21
29. Jin-Hee Lim, Aurelian Rotaru, Seong-Gi Min, Leszek Malkinski, and John B. Wiley, *J. Mater. Chem*., **2010**, *20*, 9246.
30. Sachiko Ono, Makiko Saito, Miyuki Ishiquro, and Hidetaka Asoh, *J. Electrochem.Soc*., **2004**, *151*, B473.

31. O.Jessensky, F. Müller, and U. Gösele, *Appl. Phys. Lett*., **1998**, *72*, 1173.
32. Rashid Zakeri, Clay Watts, Haibo Wang, and Punit Kohli, *Chem. Mater*., **2007**, *19*, 1954.

Chapter 3

Magnetic Nanostructures in Conventional AAO Templates*

3.1 Introduction

The fabrication of nanostructured materials such as nanodots, nanorods, and nanowires, is of considerable interest due to their various potential applications in information technology, biotechnology, medicine, or environmental engineering.[1-4] One-dimensional materials have been synthesized by electron-beam lithography,[5] self-organization-based methods,[6] or template-assisted electrodeposition.[7] Among them, electrodeposition of nanostructures in self-assembled porous membrane due to the highly ordered pores, density, and the controllable pore diameter, is a simple, low cost and high throughout technique to fabricate arrays of nanomaterials.[8] The size of the nanostructures depends on deposition conditions and selected porous templates. A commonly used template is the anodic aluminum oxide (AAO), which is a highly ordered nanoporous template synthesized by anodization of Al foil.[9-13]

The morphology of various nanostructures can greatly influence their properties. Magnetic materials, including Fe, Co and Ni, are one important example where magnetic response is quite sensitive to variability in the sizes, shapes, and spacing of the nanostructured materials.[14-16] Magnetic properties of nanostructures in AAO depend on the magnetocrystalline anisotropy and shape anisotropy.[17] The magnetocrystalline anisotropy is the dependence of the internal energy of a ferromagnet on the direction of its magnetization. The disposition of the magnetic moments in

*Much of the results from this study are described Jin-Hee Lim et al., *J. Appl. Phys*., **2010**, *107*, 09A334.

a magnetic crystal reflects the symmetry of the lattice. The symmetry of the crystal influences the interactions of the magnetic moments. Due to the magnetocrystalline anisotropy, there are directions in the space lattice in which is easier to magnetize, called easy directions.[18] The shape anisotropy is associated with the aspect ratio defined as l/d, length divided by wire diameter of nanostructure. The magnetization is independent of the orientation of the applied field for a spherical object, but for a non-spherical object it is easier to magnetize it along its long axis than along its short axis.[19] Additionally, they are significantly influenced by strong magnetostatic interactions among nanowires, because the nanowires synthesized in AAO are separated by relatively thin walls, typically of the order of tens or hundreds of nanometers.[9,16]

In this chapter, we discuss the synthesis and characterization of magnetic Fe nanostructures in AAO templates. The magnetic nanostructures with different aspect ratios were fabricated by controlling of duration of electrodeposition.

3.2 Experimental

3.2.1 Synthesis of AAO Templates

AAO templates were fabricated by two-step anodization in 0.3 M $H_2C_2O_4$ as described in Chapter 2. The alumina membrane was detached from Al without barrier layers by an electrochemical process. The templates were immersed in 5 wt% H_3PO_4 for 30 min to completely open the pore channels and also enlarge the pore size. After that, one side of the template was covered with conducting metal (Ag or Au film) by sputtering. This coated membrane was then used as a working electrode (WE).

3.2.2 Synthesis of Fe Nanostructures

For growing Fe nanostructures in AAO, we used Fe electrolyte, contained 240 g/L $FeSO_4 \cdot 7H_2O$, 45 g/L H_3BO_4, and 1 g/L ascorbic acid. Electrodeposition was conducted at constant current (-0.9 mA) at room temperature for 5 sec to 15 min on a Princeton Applied Research VMP2. A Pt wire was employed as a counter electrode (CE) and Ag/AgCl reference electrode (RE) was also connected. For microscopic and crystallographic studies of magnetic nanostructures, we removed the templates by using 0.1 M NaOH. Figure 3.1 shows a template-based electrodeposition system.

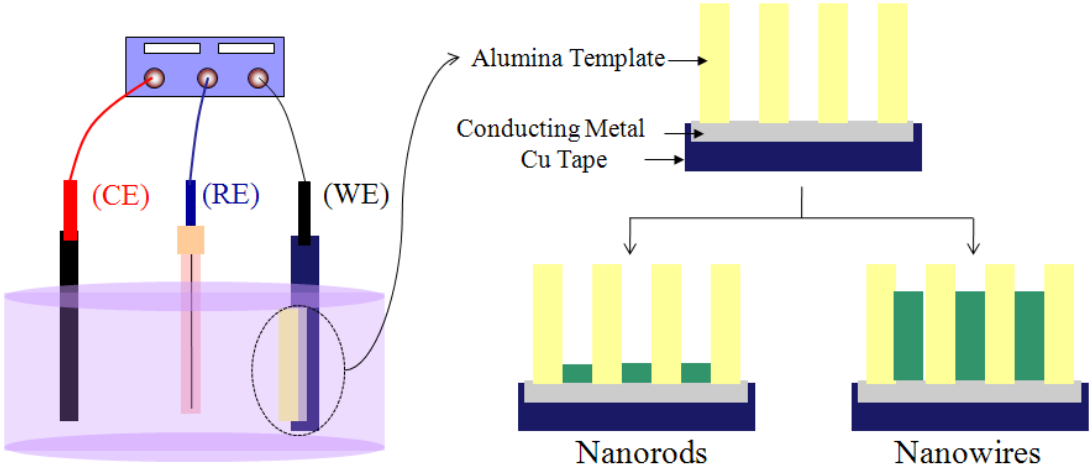

Figure 3.1 Illustration of electrodeposition system to fabricate nanostructures in AAO.

3.2.3 Characterization

The morphology of nanostructures was obtained by a field-emission scanning electron microscopy (FESEM, LEO 1530 VP). Powder X-ray diffraction (XRD) data were collected on a Phillips X-pert PW 3040 MPD X-ray powder diffractometer with Cu Kα radiation. A vibrating sample magnetometer (VSM, Lakeshore 7300 Series) was used for investigation of magnetic behavior of nanostructures in the membranes.

3.3 Results and Discussion

A series of Fe nanostructures was synthesized in a regular AAO template with 60 nm pore diameters and 100 nm interpore distances. FESEM images in Figures 3.2 and 3.3 show the morphology of Fe nanostructures with various aspect ratios and a fixed diameter. The diameter of all nanostructures corresponds well to the pore size of 60 nm and the length varied from 60 nm for the nanodots, 600 nm for the nanorods, and 4.5 μm for the nanowires, where the aspect ratios of nanostructures were 1:1, 1:10, 1:75, respectively. All of the pore channels were uniformly filled with Fe nanostructures.

Figure 3.4 XRD result of Fe nanowires in AAO shows a (110) plane at $2\theta = 45°$ and (200) plane appeared at $2\theta = 65°$. The result corresponds well to the bcc structure. Also, a Ag peak (*) appeared at $2\theta = 38°$ because of the Ag film sputtered onto the bottom surface of AAO.

Magnetic hysteresis loops measured with nanodots, nanorods, and nanowires at room temperature as seen in Figure 3.5. The direction of applied magnetic fields is either parallel ($\theta = 0°$) to the wire axis or perpendicular ($\theta = 90°$) to the wire axis. In Figure 3.5a, nearly spherical nanoparticles show no significant differences in coercivity (H_C) and the shape of hysteresis loops, even though the magnetic fields were applied parallel or perpendicular to wires. Both curves have the same coercivity of 70 Oe. The Stoner-Wohlfarth (SW) model[20,21] for elongated single domain particle predicts marked difference between the curves measured with the field at different angles. In particular, magnetization vector rotation due to field applied along the hard magnetization direction (i.e., transverse to the long axis) gives rise to nonhysteretic and linear magnetization characteristics. The coercivities of the hysteresis loops of the rods and wires are substantially smaller for the transverse magnetization direction than for the parallel one, and this tendency becomes stronger for the objects with larger aspect ratios. The measured values of H_C

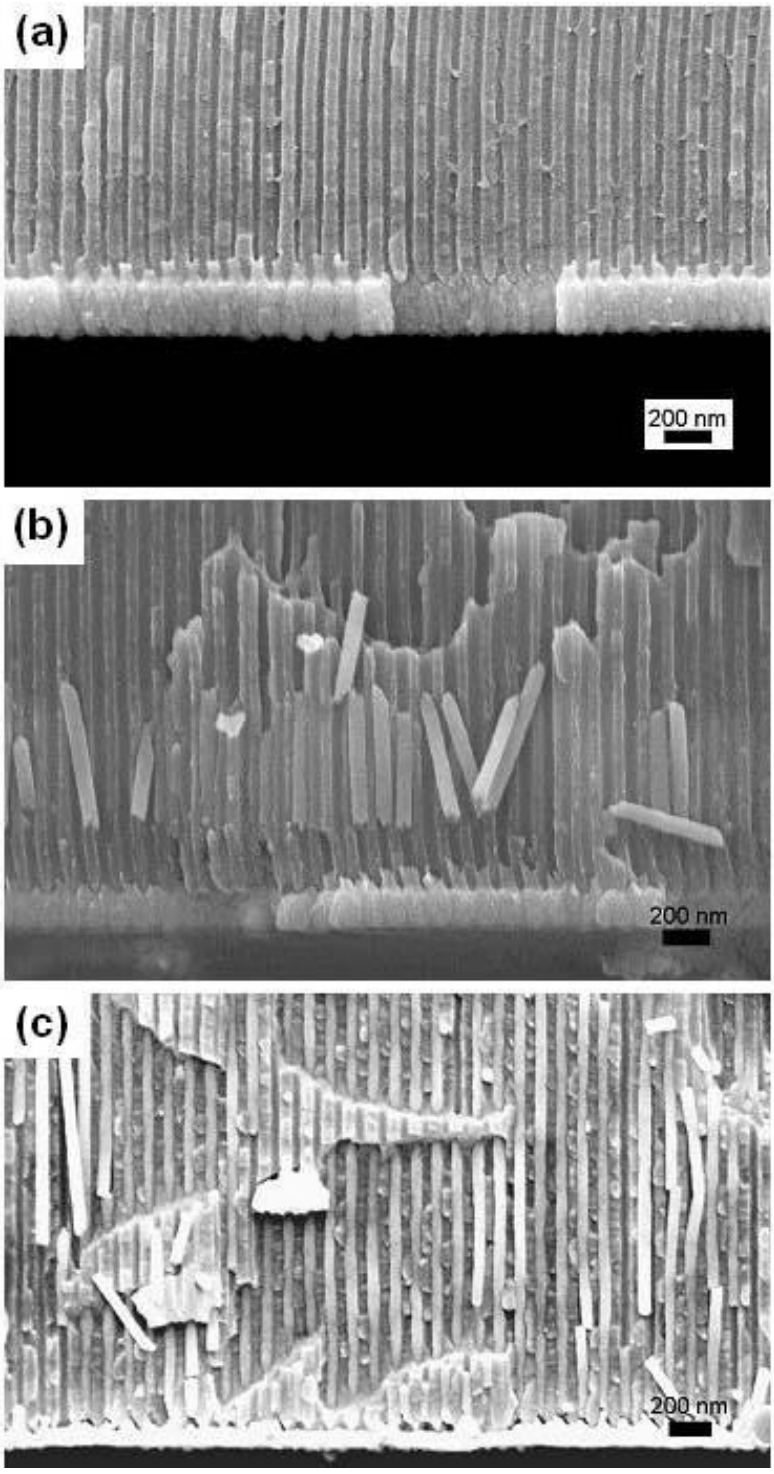

Figure 3.2 FESEM images of cross-section view of Fe nanostructures in conventional AAO with 60 nm pore diameters and 100 nm interpore distances; (a) nanodots, (b) nanorods, and (c) nanowires.

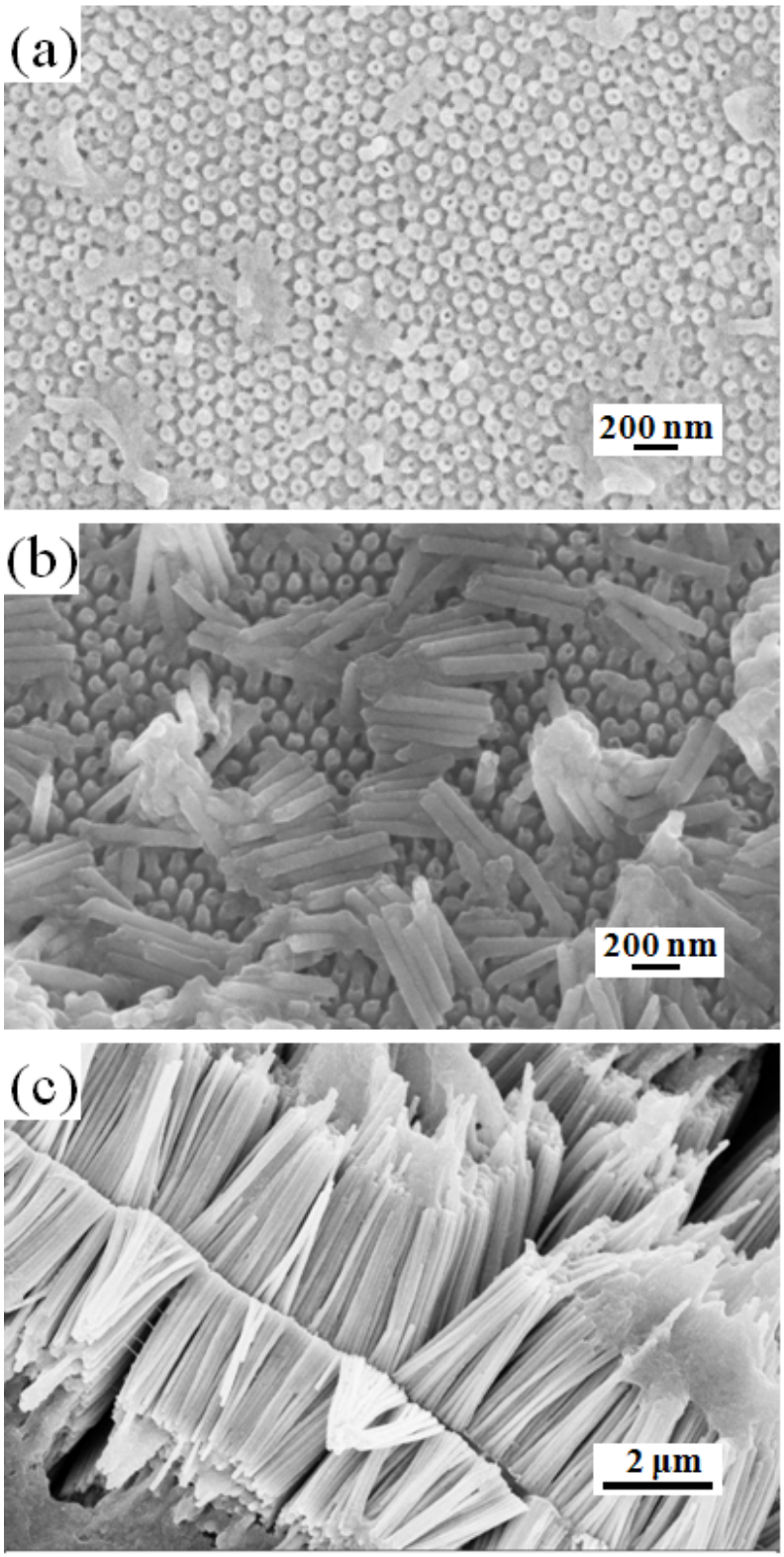

Figure 3.3 FESEM images of Fe nanostructures without AAO templates; (a) nanodots, (b) nanorods, and (c) nanowires.

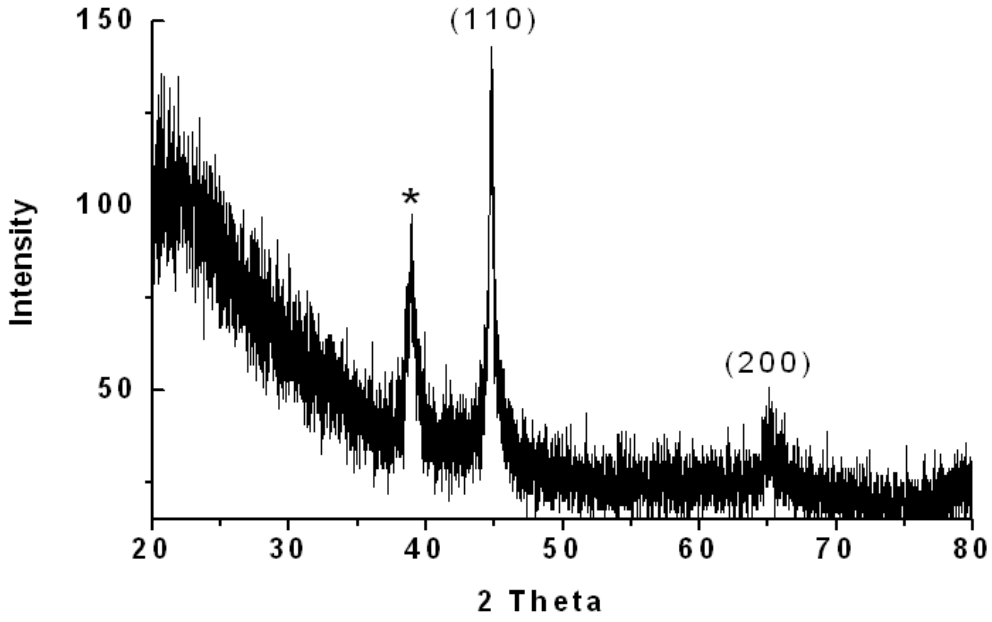

Figure 3.4 XRD result of Fe nanowires with the diameter of 60 nm. * indicates Ag peak at the bottom of the pore.

were 185 Oe at 0° compared with 130 at 90° for nanorods and 400 Oe at 0° compared with 90 Oe at 90° in the case of long nanowires. Although increased squareness and coercivity were observed for the field applied along the wires, it is clear that the shapes of the hysteresis loops presented in Figures. 3.5b and 3.5c cannot be explained through coherent magnetization rotation. Indeed, computer simulations by Ross et al.[22] and Nielsch et al.[23] show that the magnetization process in the nanostructures is evidently different from the abrupt coherent magnetization reversal predicted by the SW model. For the nanostructures with small aspect ratio, the magnetization occurs through incoherent magnetization reversal,[22] whereas in nanowires domain walls nucleate at the ends of the wires and propagate along the wires.[23]

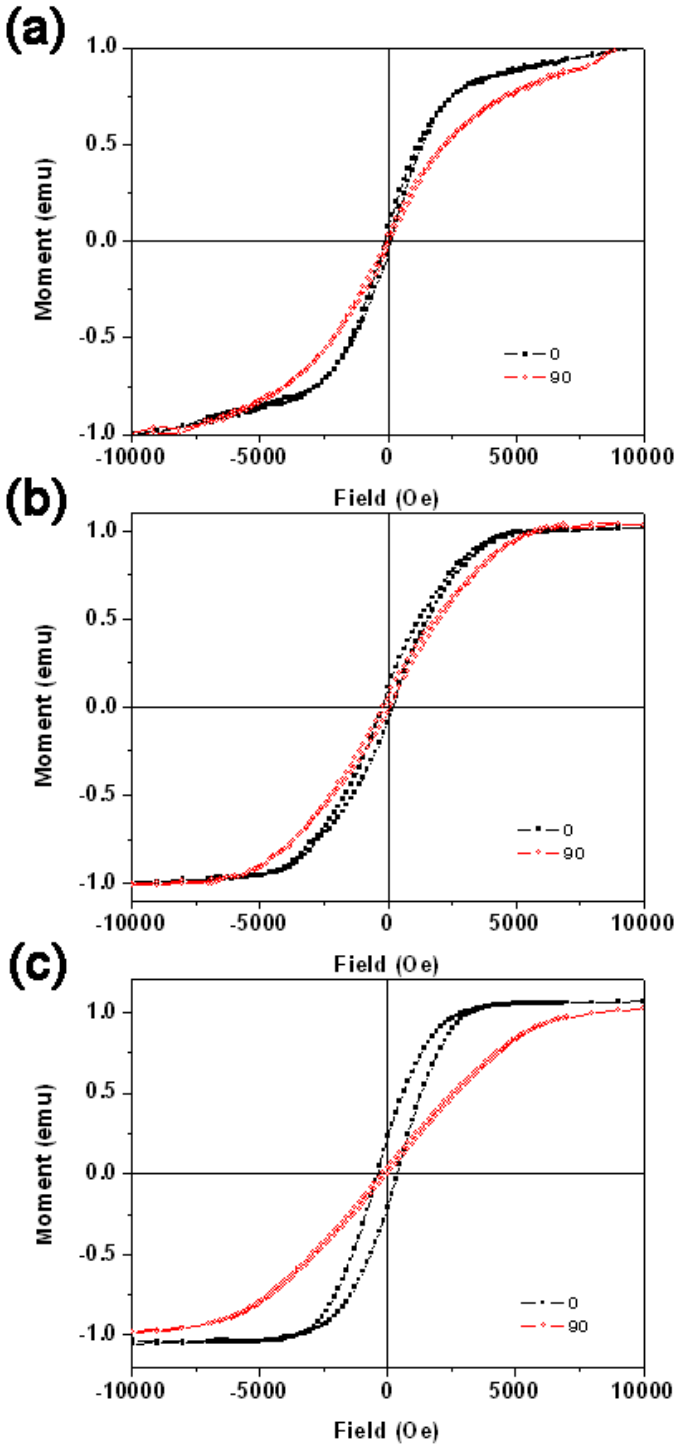

Figure 3.5 Hysteresis loops of Fe nanostructures in AAO; (a) nanodots, (b) nanorods, and (c) nanowires.

3.4 Conclusions

In summary, we synthesized Fe nanostructures, including nanodots, nanorods, and nanowires, in AAO templates with 60 nm diameters. The aspect ratio of nanostructures with keeping the diameter was controlled by changing electrodeposition time, where the ratio of nanodots, nanorods, and nanowires are 1:1, 1:10, and 1:75, respectively. The evolution of the hysteresis loops with the aspect ratio was consistent with the effect of shape anisotropy of the magnetic objects forming the arrays.

3.5 References

1. Chou, S., Krauss, P., and Restrom, P., *Science*, **1996**, *272*, 85.
2. S. Sun, C. Murray, D. Weller, L. Folks, and A. Moser, *Science*, **2000**, *287*, 1989.
3. Victor F. Puntes1, Kannan M. Krishnan, and A. Paul Alivisatos1, V. Puntes, *Science*, **2001**, *291*, 2115.
4. G. Sauer, G. Brehm, S. Schneider, K. Nielsch, R. Wehrspohn, J. Choi, H. Hofmeister, and U. Gösele, *J. Appl. Phys.* **2002**, *91*, 3243.
5. J. Qin, J. Nogués, M. Mikhaylova, A. Roig, J. S. Muñoz, and M. Muhammed, *Chem. Mater*., **2005**, *17*, 1829.
6. M. Rufenacht, S. Tsuijino, Y. Ohno, *Appl. Phys. Lett*., **1997**, *70*, 1043.
7. J. M. Baik, M. Schierhorn, and M. Moskovits, *J. Phys. Chem. C* **2008**, *112*, 2252.
8. Zeng, H.; Zheng, M.; Skomski, R.; Sellmyer, D.; Liu, Y.; Menon, L.; Bandyopadhyay, S. *J. Appl. Phys.* **2000**, *87*, 4718.
9. J.-S. Jung, J.-H. Lim, K.-H. Choi, S.-L. Oh, Y.-R. Kim, S.-H. Lee, D. A. Smith, K. L. Stokes, L. Malkinski, and C. J. O'Connor, *J. Appl. Phys*., **2005**, *97*, 10F306.
10. L. Malkinski, J.-H. Lim, W.-S. Chae, E.-M. Kim, and J.-S. Jung, *Electron. Mater. Lett*., **2009**, *5*, 87.
11. H. Masuda and K. Fukuda, *Science*, **1995**, *268*, 1466.
12. A. P. Li, F. Müller, A. Birner, K. Nielsch, and U. Gösele, *J. Appl. Phys*., **1998**, *84*, 6023.
13. W. Lee, R. Ji, U. Gösele, and K. Nielsch, *Nature Mater*., **2006**, *5*, 741.
14. I. Dumitru, F. Li, J. B. Wiley, D. Cimpoesu, A. Stancu, and L. Spinu, *IEEE Trans. Magn*., **2005**, *41*, 3361.
15. S.-L. Oh, Y.-R. Kim, L. Malkinski, A. Vovk, S. L. Whittenburg, E.-M. Kim, and J.-S. Jung, *J. Magn. Magn. Mater*., **2007**, *310*, e827.
16. O. C. Trusca, D. Cimpoesu, J.-H. Lim, X. Zhang, J. B. Wiley, A. Diaconu, I. Dumitru, A. Stancu, and L. Spinu, *IEEE Trans. Magn.*, **2008**, *44*, 2730.
17. Y. Ren, Q.F. Liu, S.L. Li, J.B. Wang, X.H. Han, *J. Mang. Magn. Mater*., **2009**, *321*, 226.
18. Soshin Chikazumi and C.D. Graham, *Physics of Ferromagnetism*, 2nd ed. (Claredon Press:

Oxford University Press, New York, 1997, ppxii, pp 655).
19. L. Sun, Y. Hao, C. L. Chien, P. C. Searson, 'Tunning the properties of magnetic nanowires' IBM Journal of Research and development, Vol 49, pp 79-102, Ian 2005.
20. J.L. Dormann, D. Fiorani, and E. Tronc, Adv. Chem. Phys. (John Wiley and Sons Inc., New York, 1977), Vol 98, pp 283-494.
21. E.C. Stoner and E.P. Wohlfarth "A mechanism of magnetic hysteresis in heterogeneous alloys", *Phil. Trans. Roy. Soc. A* **1948**, *240*, 599.
22. C. A. Ross, R. Chantrell, M. Hwang, M. Farhoud, T. A. Savas, Y. Hao, H. I. Smith, F. M. Ross, M. Redjdal, and F. B. Humphrey, *Phys. Rev. B* **2000**, *62*, 14252 .
23. K. Nielsch, R. Hertel, R. B. Wehrpohn, J. Bartel, J. Kirshner, U. Gösele, S. F. Fischer, and H. Kronmüller, *IEEE Trans. Magn.*, **2002**, *38*, 2571.

Chapter 4

Co and Ni Nanowires in Mild-Hard AAO Templates for Studying Magnetic Interactions between Nanowires*

4.1 Introduction

Conventional AAO templates are typically synthesized under the 'mild' anodizing conditions, which have a slow growth rate (below 10 μm/h). A 'hard' anodization process, which has a fast film growth rate (50~100 μm/h) and a range of interpore distances, has been reported by several research teams to minimize the limitations in processing seen in the production of conventional AAO templates.[1-3] Variations in reaction conditions allow one to control pore sizes and interpore distances as discussed in Chapter 2.

AAO templates have been widely used in the fabrication of a variety of magnetic nanowires including Fe,[4] Co,[5] Ni,[6] CoPt,[7] FePt,[8] or Fe3O4[9]. Interest in such systems includes potential applications in microwave electronics as filters or circulators[10] as well as in fundamental studies of perpendicular magnetic media.[11] The magnetic properties of AAO-nanowire composites strongly depend not only on the length of the magnetic component, but also on the diameter, shape, and interwire distance. The total effective anisotropy field is defined as the sum of dipolar interaction, magnetocrystalline, and shape anisotropy field.[12] Dipolar coupling between magnetic nanowires can greatly influence the properties of such composite systems.[11] To study the dipolar interaction, several research groups focused on Ni nanowires with different aspect ratios

*Much of the results from this study are described Jin-Hee Lim et al., *J. Mater. Chem.*, **2010**, *20*, 9246.

(length/diameter) at constant interwire distances. In the case of Ni nanowires with low aspect ratios, the dipolar interactions are significant and they can cancel or overcome the shape anisotropy.[13] Piraux et al.[12] synthesized Ni nanowires in polycarbonate and commercial alumina templates with different porosities and showed that enhanced porosity (smaller interwire distance) increased the dipolar interaction between nanowires. Although dipolar coupling has been investigated in a number of systems, these studies have not involved the variation of interpore distance with sets of wires with constant diameter and length. Therefore, the modification of interwire distance using AAO templates with well-ordered structures offers an important opportunity to explore these effects.

In this chapter, we describe the synthesis and characterization of Co and Ni nanowires in mild-hard (Mi-Ha) AAO templates with large interpore distances. Magnetic nanowire arrays produced from these templates demonstrate properties different than those synthesized in traditional mild templates.

4.2 Experimental

4.2.1 Preparation of Conventional Mild AAO and Mild-Hard AAO Templates

Conventional mild AAO templates (Mi-AAO) were synthesized by using a two-step anodization process in oxalic acid solution.[14] High purity Al (99.999%, 0.25 mm thickness, 1 x 2.5 cm^2) film was degreased in acetone and then annealed at 450 ℃ for 5 h in Ar atmosphere. The sample was electropolished in a 1:4 (volume ratio) solution of perchloric acid-ethanol at 25 V, 10 ℃. (Caution: the combination of perchloric acid and alcohols is a known explosion hazard-extreme caution, even with cooling, should be exercised.) The Al film was placed in 0.3 M oxalic acid at 17 ℃ and anodized at 40 V for 12 h. Subsequently, this initial oxide layer was completely etched

away at 80 ℃ in a solution of 1.8 wt% chromic acid-5 wt% phosphoric acid. A second anodization was then carried out in 0.3 M oxalic acid at 17 ℃ and 40 V for 2 h. Two carbon bars were employed as a counter electrode and a Kepco power supply (KLP 300-8-1200) was used to control current and voltage.

Combined mild-hard anodic aluminium oxide (Mi-Ha AAO) templates were synthesized by a three-step anodization procedure. Initially the synthesis follows the anodizing procedures as described above on conventional Mi-AAO through the secondstep, then an additional hard anodization step at 5 ℃ was carried out at 100 V for 30 min. To obtain this potential, the voltage was slowly increased from 40 V to 100 V over several minutes during which time the current density dramatically increased to 160 mA/cm^2. The current density then dropped over the next several minutes to around 20 mA/cm^2. After the second (Mi-AAO) or third anodization (Mi-Ha AAO) steps, templates were detached from the Al film by an electrochemical treatment in 1:1 mixture solution of perchloric acid-ethanol at 100 V for 10 sec at 10 ℃. To completely remove the barrier layers, samples were then immersed in a 5 wt% phosphoric acid solution for several minutes. The samples were rinsed with distilled water and acetone. The mild membrane (Mi-AAO) had 70 nm pores and the mild-hard membrane (Mi-Ha AAO) had 70 nm pores on the mild side and 110 nm pores on the hard side. Typically Mi-Ha AAO membranes (ca. 50 μm thick) contained 15 μm mild regions and 35 μm hard regions. Figure 4.1 highlights the complete fabrication process for both Mi-AAO and Mi-Ha AAO templates.

4.2.2 Synthesis of Co and Ni Nanowires

Co and Ni nanowires were grown in the pores of AAO templates by an electrodeposition method. The AAO membranes were formed into electrodes by first sputtering a thin layer of Ag film onto

one side of the template. For the Mi-Ha AAO, wires could be grown on either the hard or mild side of the template. Cu tape (3M) was attached to the Ag coating and then that side of the template was sealed with 3M scotch tape. An alligator clip was used to make contact to the Cu tape. Ni plating solution (Nickel sulfamate-RTU) was obtained from Technics Inc. and Co plating solution was prepared with 240 g/L cobalt sulfate heptahydrate (99% $CoSO_4 \cdot 7H_2O$, Sigma) and 40 g/L boric acid (99.5% H_3BO_4, Alfa Aesar). Metal nanowires were prepared at room temperature by a constant current method at -0.5 mA over several minutes on a Princeton Applied Research VMP2 with a Pt wire counter electrode. In those instances where removal of the template was desired, the sample was treated with a 0.1 M NaOH solution for 1 h.

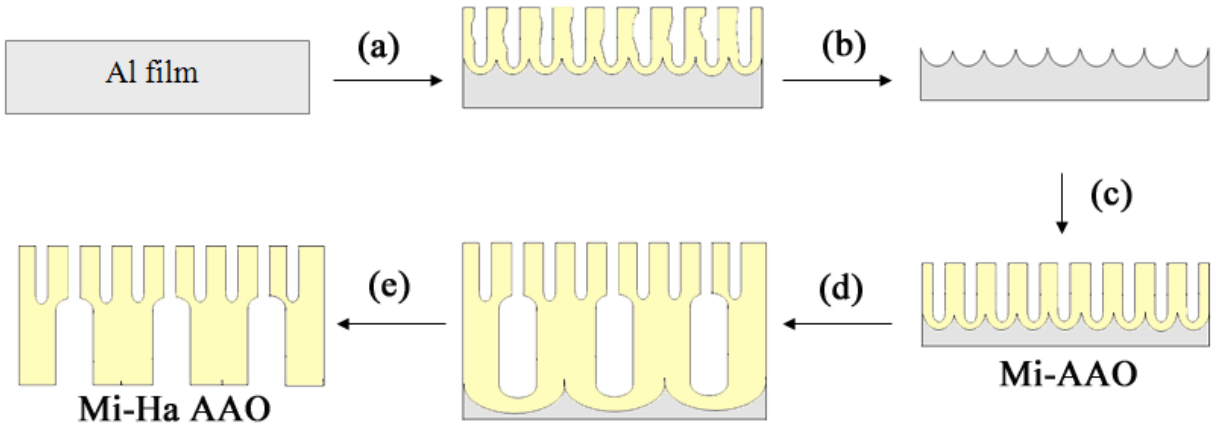

Figure 4.1 Schematic diagram of fabrication procedures for AAO templates. (a) First anodization of polished Al film at 40 V and 17 ℃, (b) etching of oxide layer, (c) second anodization at 40 V and 17 ℃ (Mi-AAO), (d) third anodization at 100 V and 5 ℃ (Mi-Ha AAO), and (e) after removal of barrier layer and Al film.

4.2.3 Characterization

A field-emission scanning electron microscopy (FESEM) was carried out on a LEO 1530 VP and

transmission electron microscopy (TEM) was performed on a JEOL 2010 electron microscope with a 200 kV acceleration voltage. A Philips X-pert PW 3040 MPD X-ray powder diffractometer with Cu Ka radiation was used to collect X-ray diffraction (XRD) data on the nanowire-membrane composites; the sample was mounted with the wires oriented perpendicular to the sample holder. The static magnetic behavior of the nanowire samples was studied with a vibrating sample magnetometer (VSM), Lakeshore 7300 Series; room temperature hysteresis data were collected on the nanowire–membrane composites with the wire oriented both parallel (0°) and perpendicular (90°) to the magnetic field.

4.3 Results

AAO templates with 70 nm pore diameter and straight pore channels are readily synthesized under mild conditions. These membranes (Mi-AAO) have an interpore distance of about 100 nm and a pore density of ca. 1.2×10^{10} pores/cm^2. In contrast, hard anodization produces membranes with larger interpore distances, 265 nm, and lower pore densities, ca. 1.6×10^{9} pores/cm^2. When used sequentially, the combination of both mild and hard anodization produces membranes (Mi-Ha AAO) with a distinct structure. While the mild (Figures 4.2a and 4.3a) and hard (Figures 4.2c and 4.3b) sides are comparable to that expected for the individual membranes (Table 4.1), the structure at the interface and the impact of this on the active pore structure are significant. Figures 4.3c and 4.3d show the low and high magnification images of the pore structure at the interface. In the transition from the mild region to the hard region approximately half of the channels remain continuous throughout the membrane while other pores initiated on the mild side terminate at the mild-hard interface. This effectively increases the distance between active pores on the mild side by as much as 3 times and in turn, decreases the pore density to values

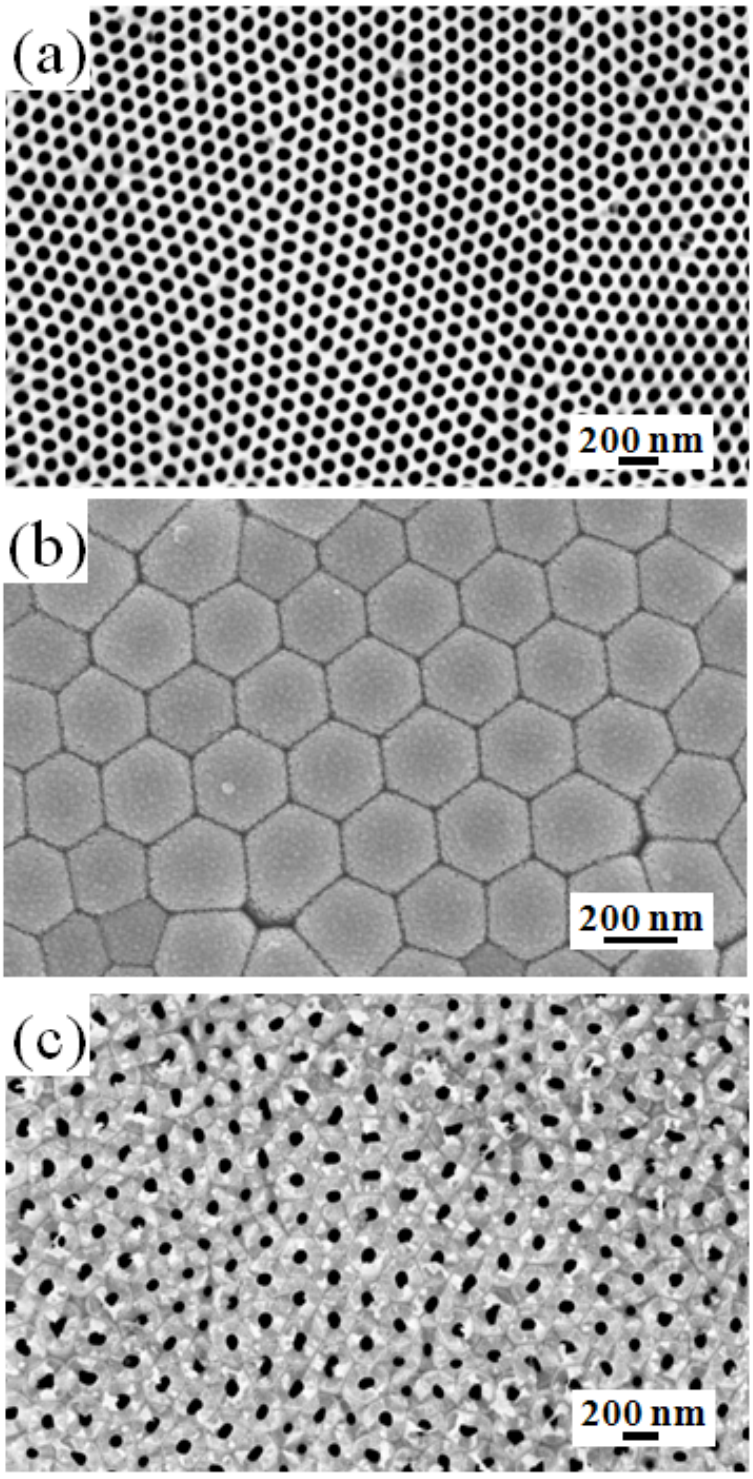

Figure 4.2 FESEM images of surface view of Mi-Ha AAO templates. (a) Top surface of mild side, (b) bottom surface with barrier layer (cylinder type), and (c) without barrier layer (channel type).

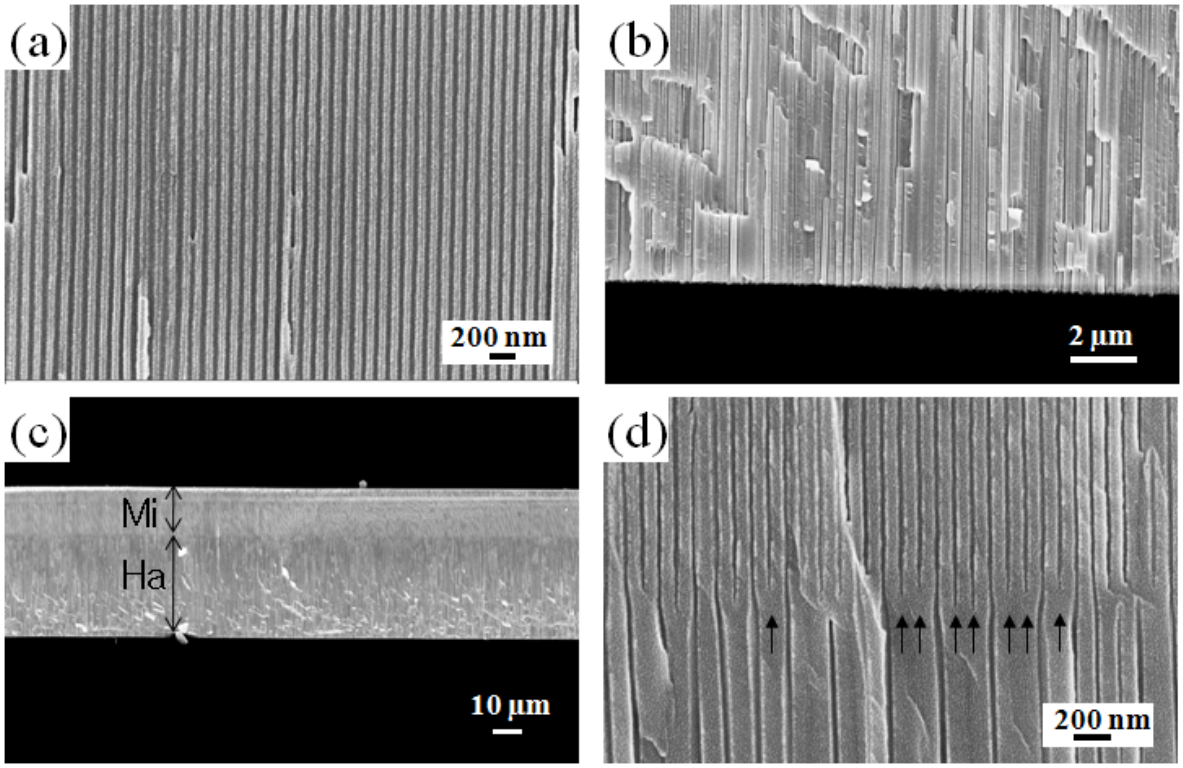

Figure 4.3 FESEM images of cross-section view of Mi-Ha AAO templates. (a) mild side, (b) hard side, (c) the boundary of mild (top) and hard side (bottom), and (f) higher magnification view of boundary region of mild (top) and hard side (bottom); black arrows highlight some selected pores that have been terminated in the hard anodization step.

Table 4.1 Structural properties of normal Mi-AAO and Mi-Ha AAO template.

Template / Condition	Mi-AAO	Mi-Ha AAO	
		Mild side	Hard side
Temperature (℃)	17	17	5
Voltage (V)	40	40	100
Film growth rate (µm/h)	7.5 (linear)	7.5 (linear)	55 (nonlinear)
Pore diameter (nm)	70±3	70±3	110±10
Barrier layer thickness (nm)	50	none	130
Interpore distance (nm): D_{int}	100	200~300	265±10
Pore density (pore/cm^2)	1.15x10^{10}	1.28~2.88x10^9	1.64x10^9

similar to that of the hard anodized portion of the membrane (Table 4.1). Similar structures have been reported recently by Shuoshuo and coworkers.[15]

The Mi-Ha AAO can be employed as a membrane for the fabrication of magnetic nanowire arrays. Wires were grown either in the hard or mild side of these membranes. Figure 4.4 shows cross-sectional images of nickel nanowires grown in various parts of the Mi-Ha membrane. In the hard side of the membrane (Figure 4.4a), 110 nm diameter wires are readily obtained within all available pores. Wires fabricated in the mild side of the AAO template, however, only grow in selected pores. Figure 4.4b shows several nickel wires occupying alternating channels. In Figure 4.4c, long wires (22 μm) that were grown across the mild-hard interface, exhibit a variation in diameter as expected in this region of the membrane. This is more obvious after removal of the template (Figure 4.4d).

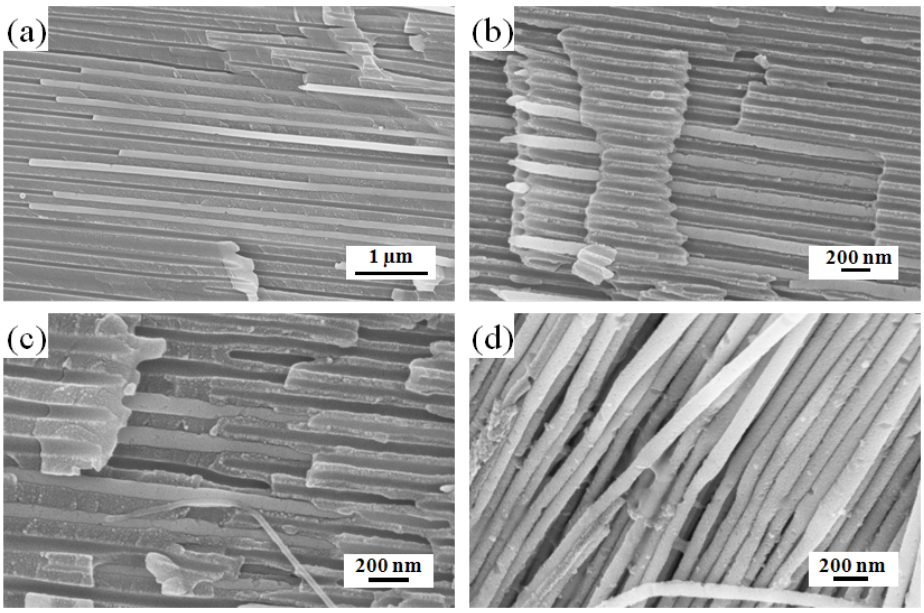

Figure 4.4 FESEM images of Ni nanowires synthesized in Mi-Ha AAO template. (a) 110 nm diameter wires grown in the hard side of the template. (b) 70 nm nanowires grown on mild side; growth of wires in alternating pores clearly shown. Nanowires grown across mild-hard interface, larger diameter portion of wire from hard side of template; (c) wires still in template, (d) wires shown after removal of template.

TEM images of dispersed nickel wires synthesized in the mild side of Mi-Ha and Mi-AAO are presented in Figures 4.5a1 and 4.5a2; selected area electron diffraction (SAED, inset) shows both sets of wires to be polycrystalline though highly crystalline in nature. Also, XRD data in Figure 4.5b reveal that the Ni nanowires in Mi-Ha AAO have an fcc structure with a highly oriented growth in the (111) direction (Ag peaks are from conducting metal film used in electrodeposition). For the cobalt nanowires synthesized in Mi-Ha AAO, TEM and SAED results in Figures 4.6a1 and 4.6a2 present evidence for polycrystalline nanowires with highly crystalline regions. XRD (Figures 4.6b1 and 4.6b2) of these wires shows the (101) and (100) directions of the hcp structure. In contrast, Co nanowires grown in the Mi-AAO template exhibit a strong (100) orientation (Figure 4.6b3).

Magnetization studies as a function of field were carried out on Ni and Co nanowires grown on the mild and hard sides of Mi-Ha AAO template as well as those grown in the standard Mi-AAO (Figures 4.6 and 4.7 and Table 4.2). Hysteresis loops were obtained at room temperature for fields both parallel (0°) and perpendicular (90°) to the wires. When the field is applied 0°, hysteresis loops show a higher coercivity in all systems. Magnetization of 3.3 μm and 11 μm nickel nanowires from the mild-side of a Mi-Ha AAO template is shown in Figures 4.6a and 4.6b, respectively. As expected,[16,17] the coercivity increases with increasing aspect ratio where the 3.4 μm wires exhibit a coercivity of 640 Oe and the 11 μm wires, 720 Oe. Also, the squareness of hysteresis loops (M_R/M_S, defined as the ratio of the magnetic remanence (M_R) to the saturation magnetization (M_S)) is almost unity at about 0.99. For 3.4 μm nanowires grown in a normal Mi-AAO template, the hysteresis loop is shown in Figure 4.6c; here there is an increase in the coercivity to 878 Oe but a reduction in the squareness to about 0.82. Figure 4.6d presents hysteresis data on 3.8 μm Ni nanowires synthesized on the hard side of Mi-Ha AAO template.

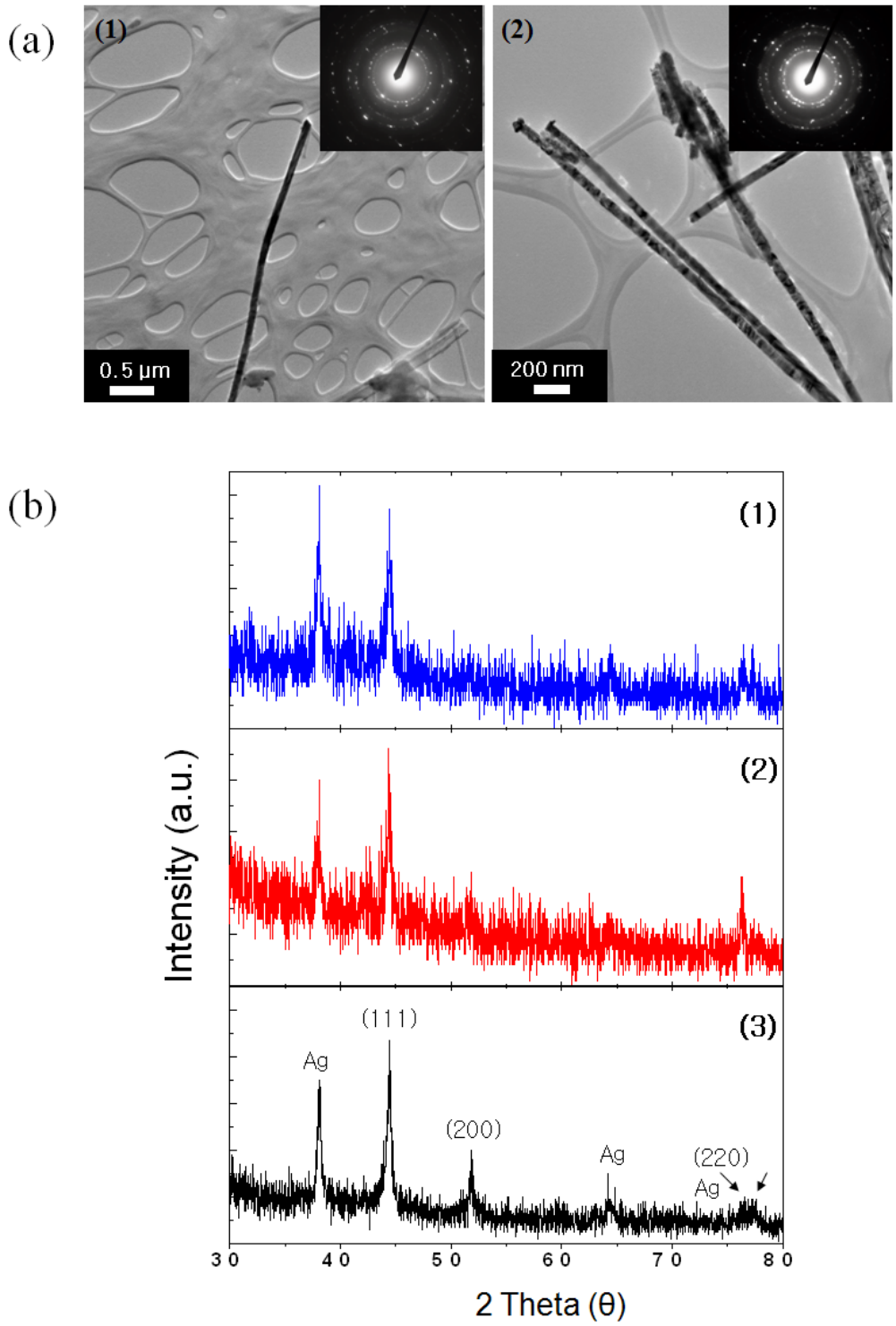

Figure 4.5 TEM images and diffraction data for Ni nanowires. (a) TEM image of dispersed Ni nanowires synthesized in mild side of Mi-Ha (a1) and Mi-AAO (a2). Inset shows SAED pattern, indicating polycrystalline structure. (b) XRD data for Ni nanowires in AAO templates: (b1) mild side and (b2) hard side of Mi-Ha AAO, (b3) normal Mi-AAO. (Ag from conducting film on bottom of AAO template.)

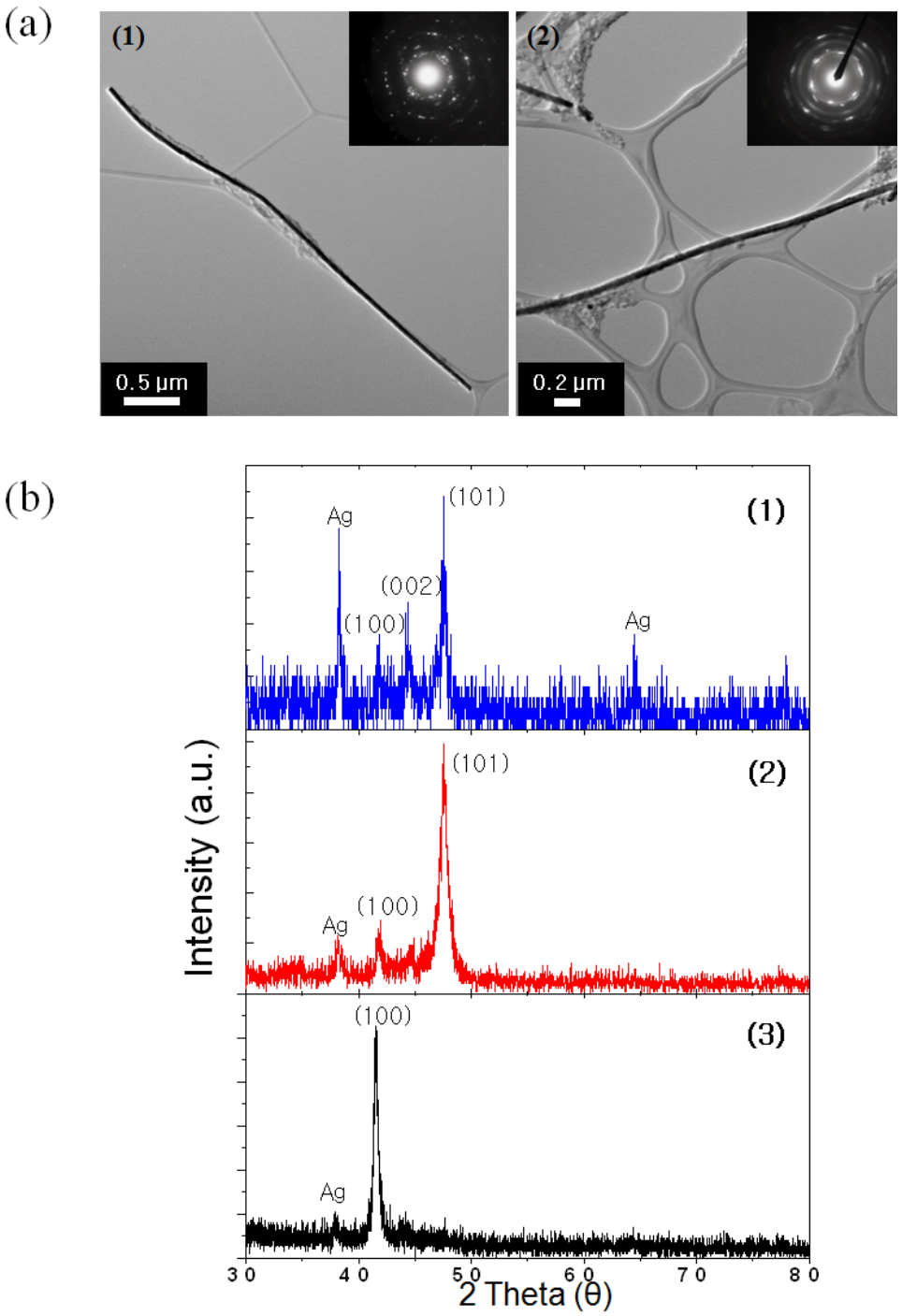

Figure 4.6 TEM images and diffraction data for Co nanowires. (a) TEM image of dispersed Co nanowires synthesized in mild side of Mi-Ha (a1) and Mi-AAO (a2). Inset shows SAED pattern, indicating polycrystalline structure. (b) XRD data for Co nanowires in AAO templates: (1) mild side and (2) hard side of Mi-Ha AAO, and (3) normal Mi-AAO. (Ag from conducting film on bottom of AAO template.)

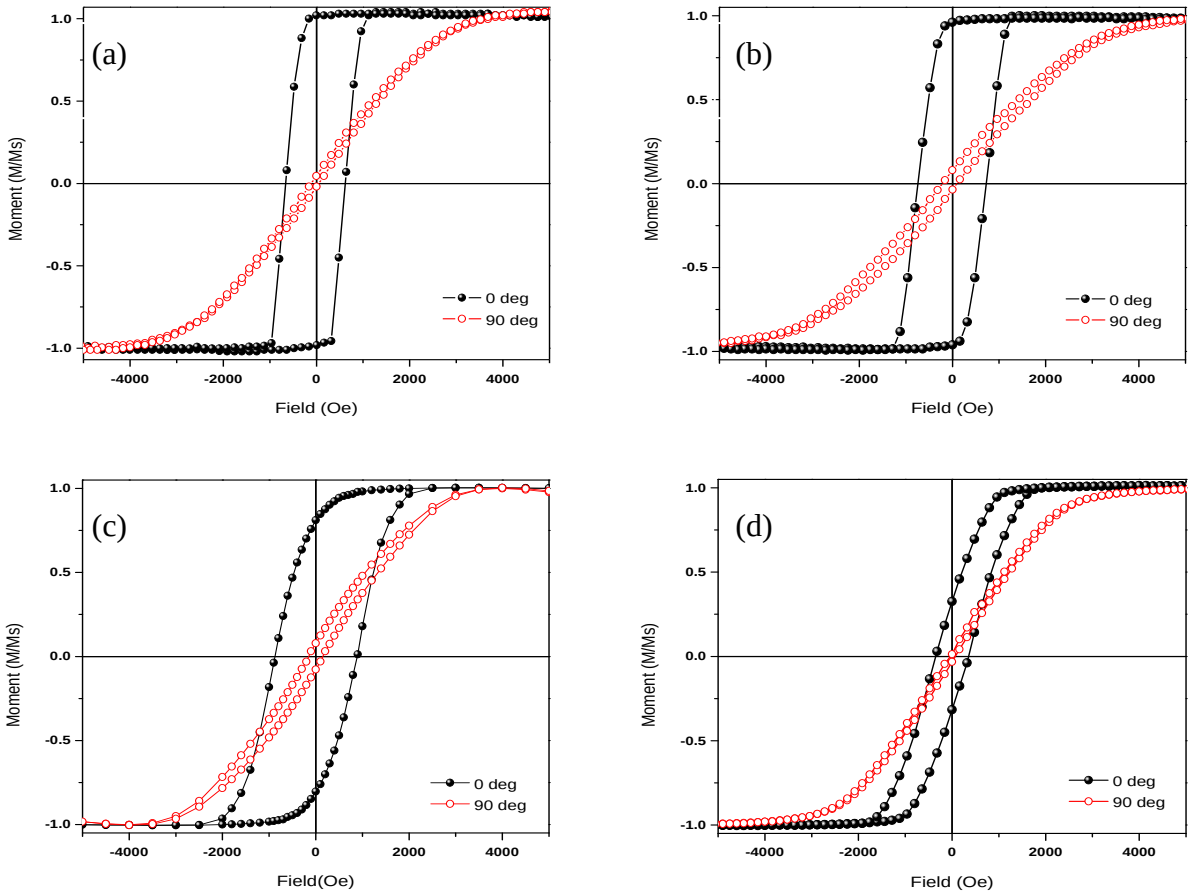

Figure 4.7 Hysteresis loops of Ni nanowires; (a, b) synthesized in Mi-Ha AAO (70 nm diameters, 200~300 nm interwire distances) with the length of (a) 3.3 μm, and (b) 11 μm; (c) synthesized in Mi-AAO (70 nm diameters, 100 nm interwire distances) with 3.4 μm in length; (d) synthesized in hard side of Mi-Ha AAO (110 nm diameters, 265 nm interwire distances) with 3.8 μm length**.**

These wires have a similar interwire distance to those in Figures 4.6a and 4.6b, but with a larger diameter of 110 nm. Here the coercivity and squareness are much less, 398 Oe and 0.39, respectively. It is well-known that increasing the relative diameter can decrease the squareness and coercivity of nanowires,[6] though nonuniformity in wire diameters may also contribute to this

behavior. Figure 4.7 and Table 4.2 present the magnetization data for the series of cobalt nanowires. Like the nickel wires, the squareness (0.90) for the wires grown on the mild side of the Mi-Ha AAO template is greater than either of those from the normal template (0.23) or the hard side of the Mi-Ha AAO template (0.25). Unlike the nickel wires, however, the coercivity for the cobalt wires grown on the mild side of the Mi-Ha AAO (950 Oe) is larger than the normal wires (750 Oe).

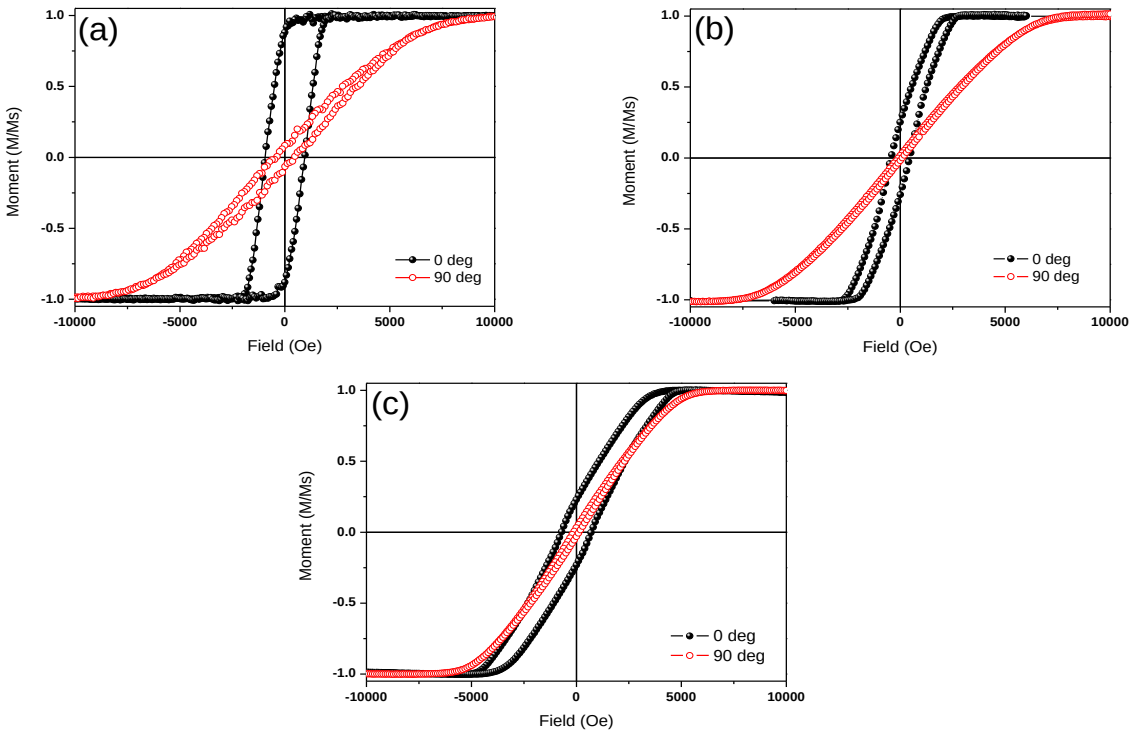

Figure 4.8 Hysteresis loops of Co nanowires; (a) synthesized in Mi-Ha AAO (70 nm diameters, 200~300 nm interwire distances) with the length of 4.5 μm; (b) synthesized in Mi-AAO (70 nm diameters, 100 nm interwire distances) with 4.7 μm length; (c) synthesized in hard side of Mi-Ha AAO (110 nm diameters, 265 nm interwire distances) with 4.8 μm length.

Table 4.2 Summary of magnetic data for Ni and Co nanowire composite arrays.

	Template	Diameter (nm)	Length (μm)	Interpore distance (nm)	Angle (°)	Coercivity (Oe)	Squareness (M_r/M_s)
Ni	Mild	70	3.4	100	0	878	0.82
					90	150	0.07
	Mi-Ha (*mild side*)	70	3.3	200~300	0	640	0.99
					90	80	0.03
	Mi-Ha (*mild side*)	70	11	200~300	0	720	0.99
					90	156	0.06
	Mi-Ha (*hard side*)	110	3.8	265	0	398	0.39
					90	50	0.06
Co	Mild	70	4.7	100	0	750	0.23
					90	150	0.03
	Mi-Ha (*mild side*)	70	4.5	200~300	0	950	0.90
					90	400	0.08
	Mi-Ha (*hard side*)	110	4.8	265	0	440	0.25
					90	50	0.01

4.4 Discussion

When considering magnetic interactions between adjacent magnetic nanowires, the ability to control the distance between wires by varying the pore structure of a template is of interest because it allows one to investigate the impact on wire-wire interactions. Some researchers have suggested that magnetic nanowire arrays could be used as tunable microwave filters.[12,13,16] For such applications, a better understanding of wire-wire interactions is needed to optimize absorption properties and varying the pore structure in AAO templates is one avenue to probe this behavior.

We have prepared a series of templates with two different pore structures so as to study the interactions between adjacent magnetic nanowires. The interpore distance of normal Mi-AAO template is about 100 nm. In the hard anodization, the interpore distance is about 265 nm. The stepwise application of mild and hard anodization initially starts with an interpore distance of about 100 nm, but once the hard anodization step is initialized the production of larger pores results in a termination of many of the mild side pores (Figure 4.2f). This produces a membrane where, though the interpore distance appears the same on the mild side (Figure 4.2a), the distance between continuous open pores is actually approximately 200~300 nm (Figure 4.2f). Terminated pore channels were obtained when the voltage was increased. The electric field becomes redistributed between the barrier layer and metal surface to reduce stress. The field is concentrated on selected pore channels so as to produce a thinner barrier layer relative to neighboring pores; the thinner barrier layer supports continued development of the selected pores while the thicker layers on neighboring pores curtail the electrolyte diffusion needed for sustained growth, so these pores terminate.

The crystalline nature and orientation of nanowires grown in porous templates are highly influenced by electrodeposition conditions including pH, current, frequency, and temperature.[5,6,18] While we used the same deposition conditions in the growth of sets of nanowires, variation was still observed. In the cobalt system, orientation of wires grown in the Mi-AAO differed from those in Mi-Ha AAO. Recent reports have described that the templates themselves[19,20] can have an important impact, where it is believed pore wall surface morphology as well as species incorporated into the pore wall during anodization in different acid solutions are important. In our studies, the important difference between the Mi-Ha AAO and Mi-AAO templates arises from the anodization conditions used in their fabrication. In the hard anodization

step, which immediately follows the mild anodization step, the mild side of Mi-Ha AAO template experiences much more extreme conditions due to the extensive local heating accompanying this process. These elevated temperatures may influence the membrane wall surface morphology and composition, even at the mild end of the membrane, subsequently impacting the nucleation and growth orientation of the magnetic wires. Further influence may come from the growth of the wires; the Mi-Ha AAO template is thicker with a smaller pore density. Since wires are grown in Mi-AAO and Mi-Ha AAO under the same conditions, those grown in Mi-Ha AAO grow at a faster rate and this might also influence the relative magnetic properties of the sets of wires.

Magnetization of nickel and cobalt nanowires is influenced by magnetocrystalline and shape anisotropy, as well as dipolar coupling between adjacent wires. The ratio of nanowire diameter to interwire distance is an important factor influencing the coercivity and squareness of hysteresis loops.[21] In general, when the ratio is decreased, coercivity and squareness increase due to the decreasing dipolar coupling between nanostructures. Sun et al.[11] using the micromagnetic simulations, investigated changes in magnetostatic interactions on varying the number, size and distance between interacting nanowires. They found that the coercivity and squareness decreased with increasing number and diameter of neighboring wires and increased with increasing interwire distance. In our study, when the field is applied 0°(parallel to the wires), hysteresis loops show a higher coercivity in all systems as shown in Figure 4.6 and 4.7 and Table 4.2. This result is consistent with the easy axis of magnetization being parallel to the wire. The squareness of the hysteresis loops for Ni (Figure 4.6a) and Co (Figure 4.7a) nanowires synthesized in the mild side of Mi-Ha AAO is larger compared to that in the normal Mi-AAO or hard side of Mi-Ha AAO. The lower squareness in the Mi-AAO relates to greater dipole interactions between

nanowires when the wires are close together. It is evident that larger interwire distances minimize such dipole interactions. In the case of the cobalt system, the coercivity of Co nanowires is greater for the Mi-Ha AAO (Figure 4.7a) versus that of the normal Mi-AAO (Figure 4.7c). In contrast, the coercivities of Ni nanowires in Mi-Ha AAO (Figure 4.6a) decreased compared to Mi-AAO (Figure 4.6c). Recently we observed similar variations in coercivity in Fe nanowires as a function of interpore distance.[17] Clearly the coercivity of nanowires is not only strictly dependent on the dipole interactions, but also magnetocrystalline and shape anisotropy play an important role in these properties. Detailed magnetic studies are warranted to better understand this behavior. First-order reversal curve (FORC) diagrams have been recently applied to map coercive field distributions and wire-wire interactions in nanowire arrays.[22,23] Such FORC studies as a function of interwire distance would better illuminate the behavior as a function of interpore distances.[24]

4.5 Conclusions

Mi-Ha AAO templates with selectively opened pore channels were produced by sequential application of both mild and hard anodizing processes. An interpore distance of Mi-Ha AAO was increased as much as 3 times compared to conventional Mi-AAO and the pore size was also modulated by the combination of mild and hard anodizations. Fabrication of AAO templates with varying interpore distance allows one to probe the magnetic interactions of adjacent nanowires. While an improvement in squareness can readily be seen on separation of both nickel and cobalt nanowires, the influence of this separation on coercivities is apparently more complex. Further investigation is needed to better understand the influence of wire-wire interactions on coercivity.

4.6 References

1. H. Masuda and K. Fukuda, *Science*, **1995**, *268*, 1466.
2. Woo Lee, Ran Ji, Ulrich Gösele, and Kornelius Nielsch, *Nat. Mater*., **2006**, *5*, 741.
3. Wei Chen, Jian-Shuang Wu, and Xing-Hua Xia, *ACS Nano*, **2008**, *2*, 959.
4. S. Yang, H. Zhu, D. Yu, Z. Jin, S. Tang and Y. Du, *J. Magn. Magn. Mater*., **2000**, *222*, 97.
5. X. Huang, L. Li, X. Luo, X. Zhu and G. Li, *J. Phys. Chem. C* **2008**, *112*, 1468.
6. H. Pan, B. Liu, J. Yi, C. Poh, S. Lim, J. Ding, Y. Feng, C. H. A. Huan and J. Lin, *J. Phys. Chem. B* **2005**, *109*, 3094.
7. F. M. F. Rhen, E. Backen and J. M. D. Coey, *J. Appl. Phys.*, **2005**, *97*, 113908.
8. Y. Dahmane, L. Cagnon, J. Voiron, S. Pairis, M. Bacia, L. Ortega, N. Benbrahim and A. Kadri, *J. Phys. D: Appl. Phys.*, **2006**, *39*, 4523.
9. T. Wang, Y. Wang, F. Li, C. Xu and D. Zhou, *J. Phys.: Condens. Mater.*, **2006**, *18*, 10545.
10. X. Kou, X. Fan, H. Zhu and J. Q. Xiao, *Appl. Phys. Lett.*, **2009**, *94*, 112509.
11. D.-L. Sun, J.-H. Gao, X.-Q. Zhang, Q.-F. Zhan, W. He, Y. Sun and Z.-H. Cheng, *J. Magn. Magn. Mater*., **2009**, *321*, 2737.
12. M. Darques, J. Spiegel, J. De la Torre Medina, I. Huynen and L. Piraux, *J. Magn. Magn. Mater*., **2009**, 321, 2055.
13. A. Encinas-Oropesa, M. Demand, L. Piraux, I. Huynen and U. Ebels, *Phys. Rev. B* **2001**, *63*, 104415.
14. J.-H. Lim, W.-S. Chae, H.-O. Lee, L. Malkinski, S.-G. Min, J. B. Wiley, J.-H. Jun, S.-K. Ham and J.-S. Jung, *J. Appl. Phys*., **2010**, *107*, 09A334.
15. C. Shuoshuo, L. Zhiyuan, H. Xing and L. Yi, *J. Mater. Chem*., **2009**, *19*, 5717.
16. O. C. Trusca, D. Cimpoesu, J.-H. Lim, X. Zhang, J. B. Wiley, A. Diaconu, I. Dumitru, A. Stancu and L. Spinu, *IEEE Trans. Magn*., **2008**, *44*, 2730.
17. S. L. Oh, Y. R. Kim, L. Malkinski, A. Vovk, S. L. Whittenburg, E. M. Kim and J. S. Jung, *J. Magn. Magn. Mater*., **2007**, *310*, e827.
18. J. Zhang, G. A. Jones, T. H. Shen, S. E. Donnelly and G. Li, *J. Appl. Phys.*, **2007**, *101*, 054310.
19. N. J. Gerein and J. A. Haber, *J. Phys. Chem. B* **2005**, *109*, 17372.
20. J. M. Baik, M. Schierhorn and M. Moskovits, *J. Phys. Chem. C* **2008**, *112*, 2252.
21. M. Vázquez, M. Hernández-Vélez, K. Pirota, A. Asenjo, D. Navas, J. Velázquez, P. Vargas and C. Ramos, *Eur. Phys. J. B*, **2004**, *40*, 489.
22. L. Spinu, A. Stancu, C. Radu, F. Li and J. B. Wiley, *IEEE Trans. Magn.*, **2004**, *40*, 2116.
23. M. Ciureanu, F. Beron, P. Ciureanu, R. W. Cochrane, D. Menard, A. Sklyuyev and A. Yelon, *J. Nanosci. Nanotechnol.*, **2008**, *8*, 5725.
24. Aurelian Rotaru, Jin-Hee Lim, Denny Lenormand, Andrei Diaconu, John. B. Wiley, Petronel Postolache, Alexandru Stancu, Leonard Spinu, submitted.

Chapter 5

Electrodeposited Iron Oxide Nanotubes in Porous Alumina Templates

5.1 Introduction

Iron oxide nanomaterials with various phases including hematite (α-Fe_2O_3), maghemite (γ-Fe_2O_3), and magnetite (Fe_3O_4) are widely used as magnetic carriers in biomedicine, magnetic recording materials, gas sensors, or catalysts because of their low cost, stability, nontoxicity, and environmental friendliness.[1-4] Currently, for future nanodevice designs and biomedical applications, considerable efforts have been invested in the development of synthetic methods for iron oxide nanostructures such as nanoparticles,[4] nanowires,[5] and nanotubes.[6] Furthermore, understanding the relationship between materials properties and their morphology is also important in the development of promising candidates as well as in controlling of the size, shape, and phase to extend application areas. Clearly, the morphology and phases of nanostructures are highly dependent on their preparation protocols.

Nanoparticles in the size regime of 5 to 20 nm have been widely studied for several decades. Self-assembled nanoparticles were synthesized by thermal decomposition or a solvothermal approach and were obtained with shapes consisting of diamonds, cubes, triangles, and spheres.[4,7-9] Recently, zero-dimensional nanoparticles are utilized as starting materials to fabricate one-dimensional nanostructures; Ye et al.[10] employed zero-dimensional Fe_3O_4/SiO_2 core-shell particles with a TiO_2 adhesive layer to produce peapod-like structures and Zhou et al.[11] reported γ-Fe_2O_3 nanochain structures synthesized by chemical vapor deposition, where the small nanoparticles were aggregated to larger particles and larger particles were then assembled into

necklace-like nanochains by strong anisotropic magnetic forces.

In the synthesis of iron oxide nanowires, researchers employed various techniques including chemical vapor deposition,[5] sol-gel,[12] electrodeposition,[13] or hydrothermal reduction.[14] Nasibulin et al. used pure Fe foil to grow one-dimensional α-Fe_2O_3 nanowires under strictly-controlled conditions.[15] Some iron oxide nanostructures change their phase after specific heat treatments; Fe_2O_3 can be transformed to Fe_3O_4 at > 300 ℃ under H_2 gas flow by reduction, and Fe_3O_4 can be converted back to Fe_2O_3 in air by reoxidation.

Nanotube structures have recently attracted much attention. The large surface area of α-Fe_2O_3 nanotubes leads to improved sensitivity as a gas sensor and higher capacity for lithium-ion batteries.[16,17] Magnetic properties of nanotubes are also very sensitive to their morphology such as wall thickness, inner/outer diameter, and length.[18-20] However, only a few studies have reported the synthesis of iron oxide nanotubes. Mohapatra et al.[6] synthesized α-Fe_2O_3 nanotubes by an anodization of pure Fe film. Most of the other reports are based on the template-assisted approaches such as thermal decomposition,[21] atomic layer deposition,[22] and hydrothermal methods.[23]

Here we focus on the synthesis and characterization of iron oxide nanotubes. To the best of our knowledge this is the first report describing the production of iron oxide nanotubes via template-based electrodeposition. This method readily produces β-FeOOH nanotubes, a starting material in the production of α-Fe_2O_3 or Fe_3O_4. The morphology, structure, and magnetic properties of these iron oxide nanotubes can be well controlled by heat treatments.

5.2 Experimental

5.2.1 Synthesis of Iron Oxide Nanotubes

Iron oxide nanotubes were synthesized by an electrodeposition method within anodic alumina membranes with 200 nm pore diameters (Whatman International Ltd.). A conducting Ag film was sputtered on one side of alumina membranes. Electrodes were prepared according to our previous report.[24] Electrodeposition was performed in an aqueous solution containing 9 g/L $FeCl_3$ (98%) and 14 g/L $(NH_4)_2C_2O_4 \cdot H_2O$ (99%) at -0.5 mA for 3~15 min. After that, the membranes were washed several times with DI water and acetone. For thermal treatments, the samples were heated at 500 ℃ (heating rate: 4 ℃/min) in flowing air or O_2 for 2 h, 325 ℃ (10 ℃/min) in pure H_2 for 2 h, and 600 ℃ (5 ℃/min) in H_2/N_2 for 2 h. The alumina membranes were dissolved in 0.1 M NaOH for 1 h.

5.2.2 Characterization

A field-emission scanning electron microscopy (FESEM: LEO 130 VP) and transmission electron microscopy (TEM: JEOL EM 2010) were used to investigate the size and shape of all the samples. TEM operated at an acceleration voltage 200 kV was also used for characterization of the crystal structure. Samples were examined with a Philips X-pert PW 3040 MPD X-ray powder diffractometer with CuKα radiation. Static magnetic behavior of the nanotube samples was studied with a vibrating sample magnetometer (VSM: Lakeshore 7300 Series). Room temperature hysteresis data were collected on the nanotube-membrane composites both parallel (0°) and perpendicular (90°) to the magnetic field. A superconducting quantum interface device (SQUID: Quantum Design MPMS XL) was employed for measurement of field cooled (FC) and zero field cooled (ZFC) magnetic curves.

5.3 Results

5.3.1 α-Fe_2O_3 nanotubes

Figure 5.1 shows cross-sectional view of a series of iron-containing nanotube structures grown in alumina templates in 5 min (Figures 5.1a-c) and 15 min (Figures 5.1d-f). The as-deposited iron oxyhydroxide (FeOOH) samples, Figures 5.1a and 5.1d, show that the resulting nanotubes contain a number of thin plate-like structures growing perpendicular to the walls of the channels such that in some instances they bridge a cross the inner walls. Samples with longer (15 min) deposition times (Figure 5.1d) exhibit a greater number of these plate-like features. When the tubes are heated in open air at 500 ℃, they exhibit a reduced surface area with loss of the plate structures as shown in Figures 5.1b and 5.1e. In contrast, if the tubes are heated in flowing O_2 at 500 ℃ (Figures 5.1c and 5.1f), the plate structures are maintained. A comparison of Figures 5.1b and 5.1e with Figures 5.1c and 5.1f, respectively, highlights that the morphology inside the nanotubes can be changed by the heating conditions, air versus O_2 flowing. The structure of iron oxide nanotubes after heat treatments at 500 ℃ was revealed by XRD as shown in Figure 5.2 where both sets of samples are α-Fe_2O_3. Henceforth, the Fe_2O_3 samples shown in Figures 5.1e and 5.2a (air treatment) and Figures 5.1f and 5.2b (oxygen treatment) are designated Fe_2O_3-air and Fe_2O_3-ox, respectively.

FESEM and TEM images of Fe_2O_3-air (Figure 5.3) and Fe_2O_3-ox (Figure 5.4) were obtained after removal of alumina templates with an NaOH solution. In Figure 5.3a, the α-Fe_2O_3 exhibits a tubular structure with smooth outer/inner surfaces. Figure 5.3b TEM image shows that the nanotubes contain small particles of 4~18 nm diameters. Some of the particles were separated from the surface likely due to the ultra-sonication procedure used during the sample preparation. It is also confirmed that Fe_2O_3-air has no plate-like features inside the tubes as also seen in Figures 5.1b and 5.1e. In case of Fe_2O_3-ox, we are able to see the plate-like structures through its

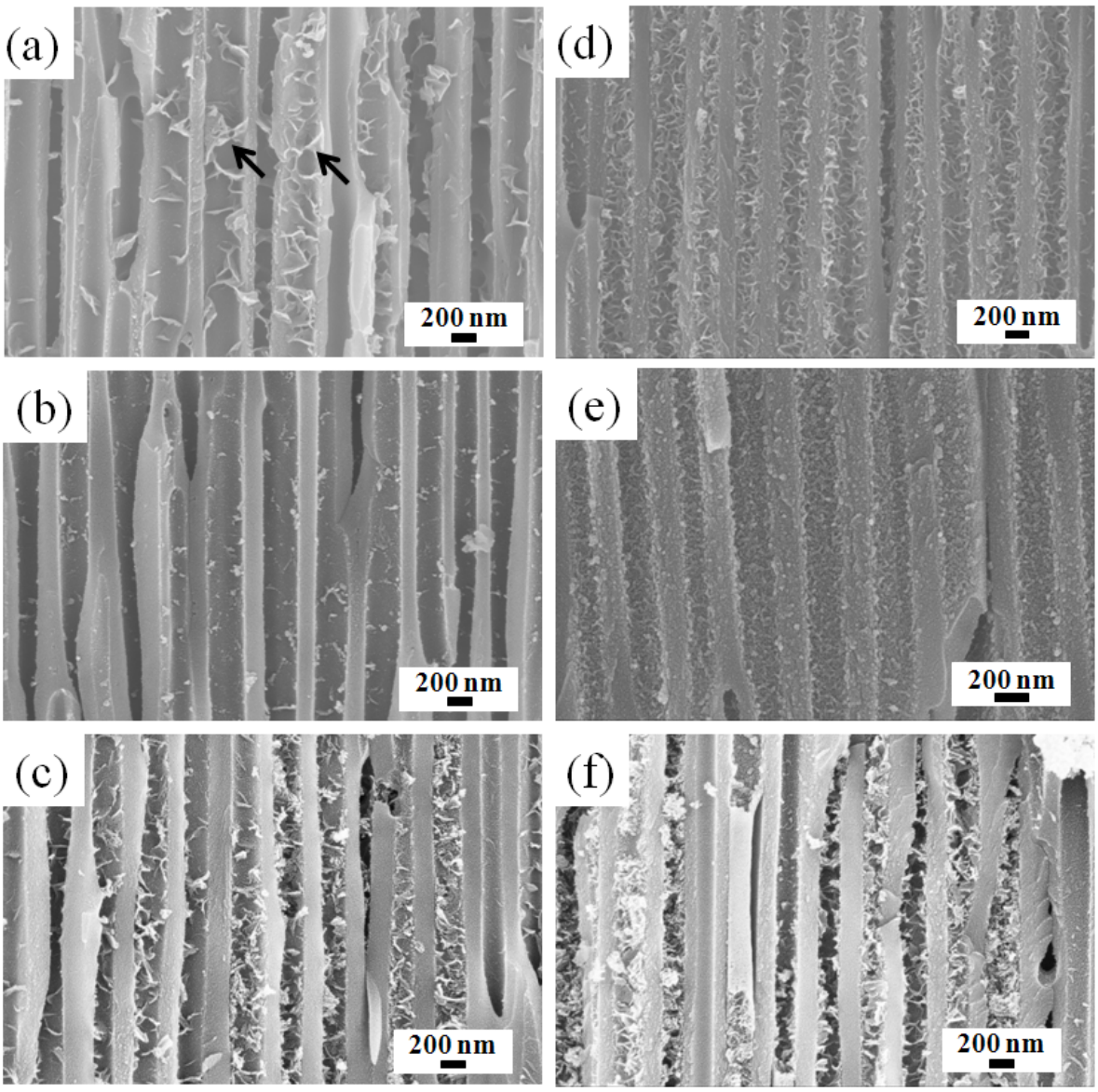

Figure 5.1 FESEM images of cross-sectional view of nanotubes electrodeposited for (a-c) 5 min and (d-f) 15 min; (a and d) as-synthesized (β-FeOOH), (b and e) after heating in air at 500 ℃ (α-Fe_2O_3), and (c and f) after heating in O_2 flowing at 500 ℃ (α-Fe_2O_3). As-synthesized and oxygen heated nanotubes have plate-like features inside the tubes marked as black arrows in image (a).

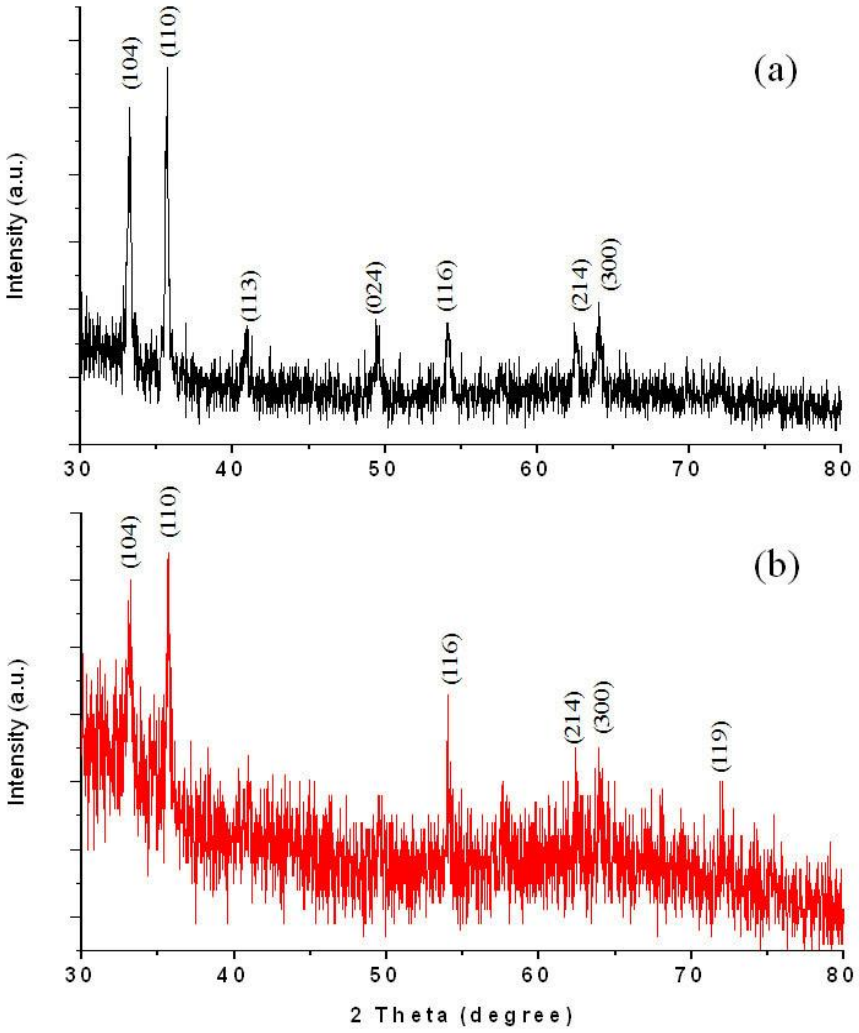

Figure 5.2 XRD results of α-Fe_2O_3 nanotubes (a) Fe_2O_3-air and (b) Fe_2O_3-ox. The alumina templates were partly dissolved before the measurement.

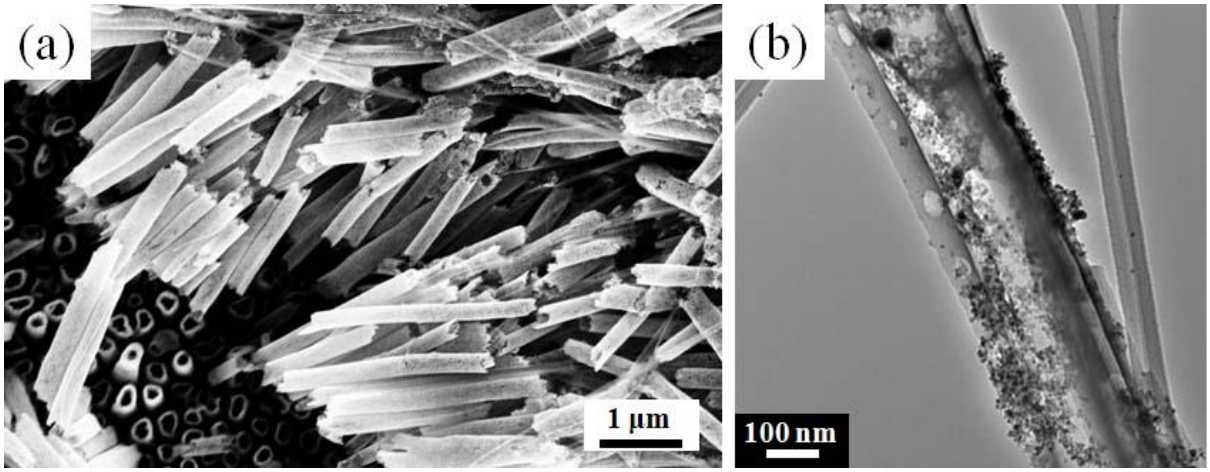

Figure 5.3 (a) FESEM and (b) TEM images of Fe_2O_3-air. After heating in air at 500 ℃, the alumina templates were dissolved in a 0.1 M NaOH solution.

thin wall (Figure 5.4a), where the arrows indicate these features. Figure 5.4b shows the top surface of Fe_2O_3-ox. The thin layer structures bridging the tube wall are also clearly observed by TEM in Figure 5.4c. Images of Fe_2O_3-ox show that the tubular structure is made up of small crystalline nanoparticles. The appearance of ring pattern in selected area electron diffraction (SAED) confirms the polycrystalline nature of α-Fe_2O_3 (Figure 5.4d). The resolved lattice fringe of 0.25 nm corresponds to the (110) plane of hematite as seen in Figure 5.4e.

Magnetic hysteresis loops of α-Fe_2O_3 nanotubes (Figures 5.5) were measured at room temperature, where the magnetic field was applied parallel (0º) and perpendicular (90º) to the tube axis. Coercivity and remanence are not exhibited at either 0º or 90º indicating that both sets of α-Fe_2O_3 nanotubes are superparamagnetic. The hysteresis loops for α-Fe_2O_3 nanotubes grown with 5, 10, and 15 min deposition times also show a superparamagnetic property. For a more detailed magnetic characterization of iron oxide nanotube arrays, the field cooled (FC) and zero field cooled (ZFC) magnetization curves were measured at applied field of 500 Oe, perpendicular to the wire axis. In general, bulk α-Fe_2O_3 materials are known to be

antiferromagnetic below the Morin transition (T_M, 260 K) and are weakly ferromagnetic above T_M due to a spin-flip transition.[23] The magnetization curves of Fe_2O_3-air and Fe_2O_3-ox are shown in Figures 5.6a and 5.6b, respectively; no evidence for the Morin transition is observed and the FC-ZFC further confirm superparamagnetic behavior. Similar results have been recently observed in α-Fe_2O_3 nanoparticles,[25] nanotubes,[26] and mesoporous α-Fe_2O_3.[27]

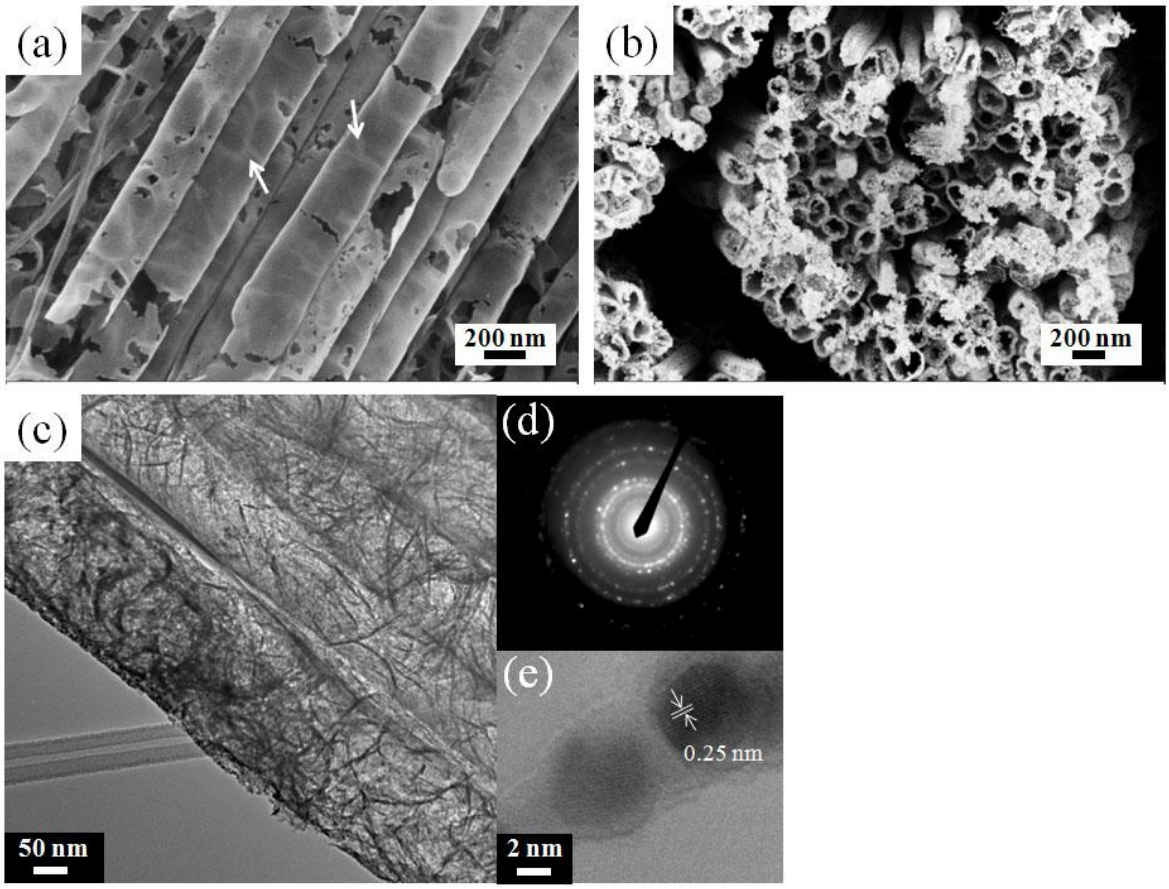

Figure 5.4 FESEM images of (a) side and (b) top surface of α-Fe_2O_3 nanotubes heated in O_2 gas at 500 ℃. Arrows indicate plate-like structures located in the transparent nanotubes. (c) TEM image and (d) SAED pattern of iron oxide nanotubes of Fe_2O_3-ox. The nanotubes consist of nanoparticles with 4~18 nm diameters and show polycrystalline α-Fe_2O_3. (e) The lattice fringe of 0.25 nm corresponds to the hematite iron oxide.

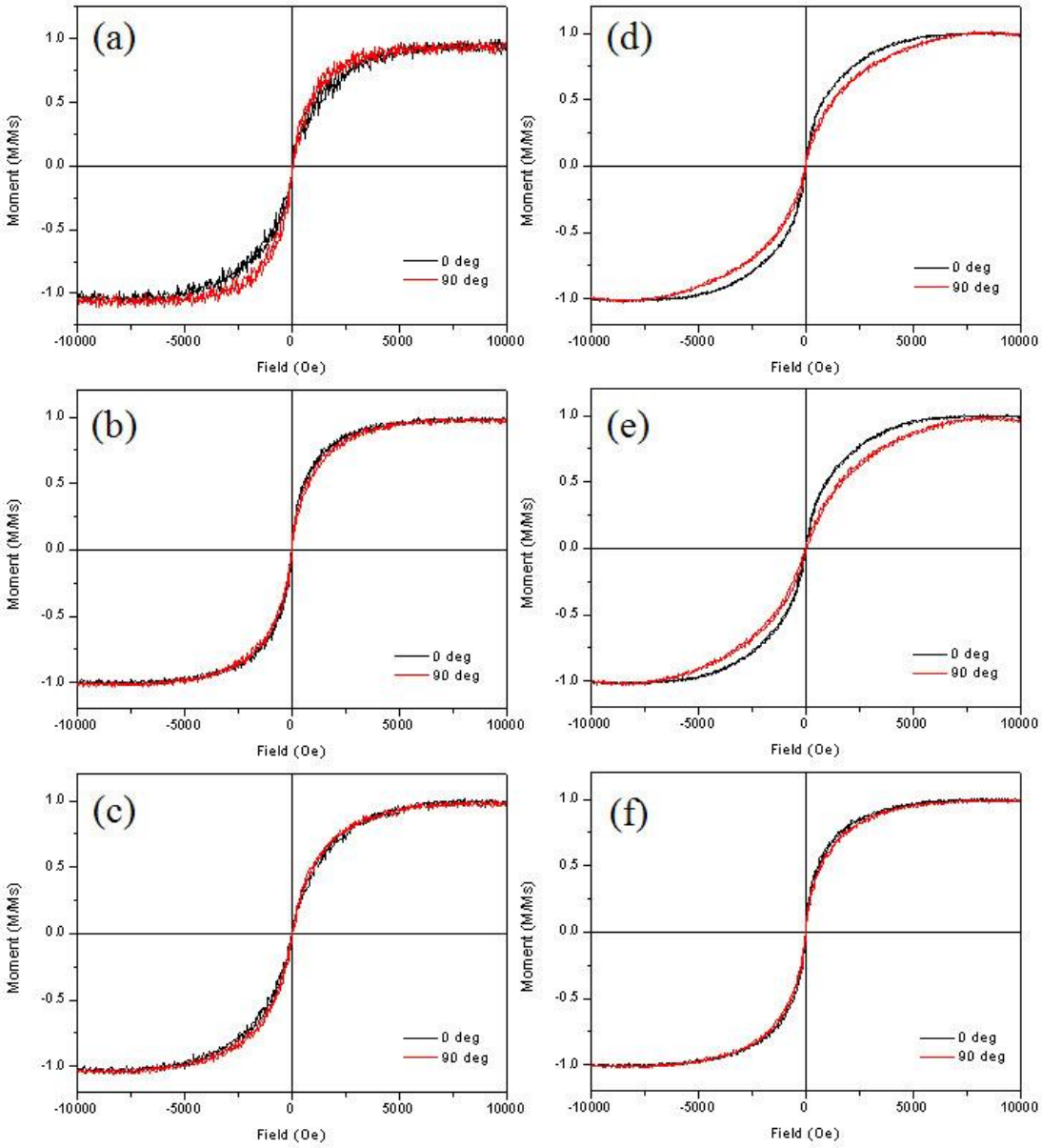

Figure 5.5 Hysteresis loops of α-Fe_2O_3 nanotubes; (a-c) Fe_2O_3-air and (d-f) Fe_2O_3-ox, electrodeposited for (a and d) 5 min, (b and e) 10 min, and (c and f) 15 min. The magnetic field was applied parallel (0 degree, black) and perpendicular (90 degree, red) to the nanotubes. Hematite Fe_2O_3 nanotubes show a superparamagnetic behavior.

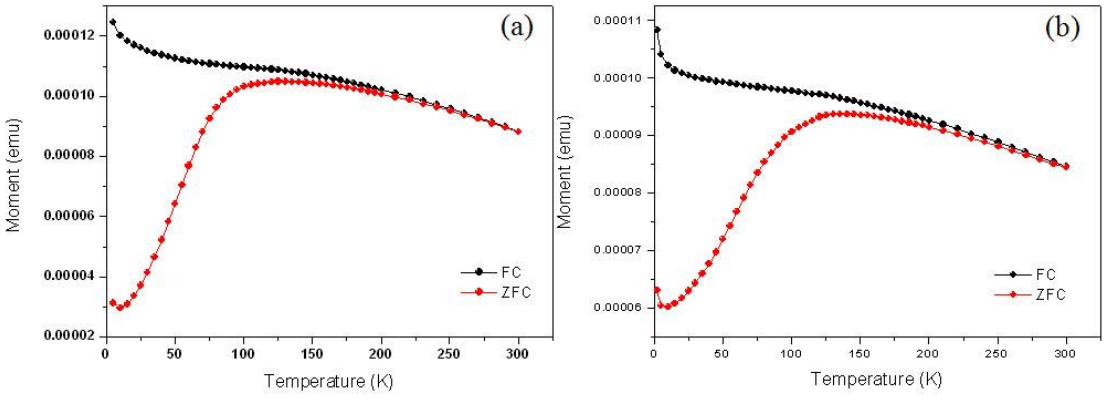

Figure 5.6 FC-ZFC magnetization curves of (a) Fe_2O_3-air and (b) Fe_2O_3-ox. The magnetic field of 500 Oe was applied perpendicular (90 degree) to the nanotubes.

5.3.2 Fe_3O_4 nanotubes

The α-Fe_2O_3 nanotubes in alumina templates were utilized in the synthesis of Fe_3O_4 nanotubes by reduction at high temperature under flowing H_2/N_2 gas. Fe_3O_4 nanotubes produced by using Fe_2O_3-air and Fe_2O_3-ox are called Fe_3O_4-air-hy and Fe_3O_4-ox-hy, respectively. FESEM images of Fe_3O_4-air-hy (Figure 5.7a) and Fe_3O_4-ox-hy (Figure 5.7b) show a cross-sectional view of Fe_3O_4 nanotubes in the template as prepared by heating at 600 ℃ in H_2/N_2 gas. Fe_3O_4-air-hy in Figure 5.7a shows large round particles that are similar to those seen with Fe_2O_3-air in Figure 5.1e. The nanostructures for Fe_3O_4-ox-hy in Figure 5.7b have thin plate features inside of the tubes as seen in Fe_2O_3-ox (Figure 5.1f).

TEM images of Fe_3O_4-air-hy (Figure 5.8) and Fe_3O_4-ox-hy (Figure 5.9) also show a tubular structure built from nanoparticles for the Fe_3O_4 nanotubes. Figures 5.8a and 5.8b clearly show the Fe_3O_4-air-hy morphology and the wall thickness of 9 nm. In Figure 5.8c, the particle size was increased to 7~25 nm diameters compare to Fe_2O_3-air (Figure 5.3). The SAED pattern in

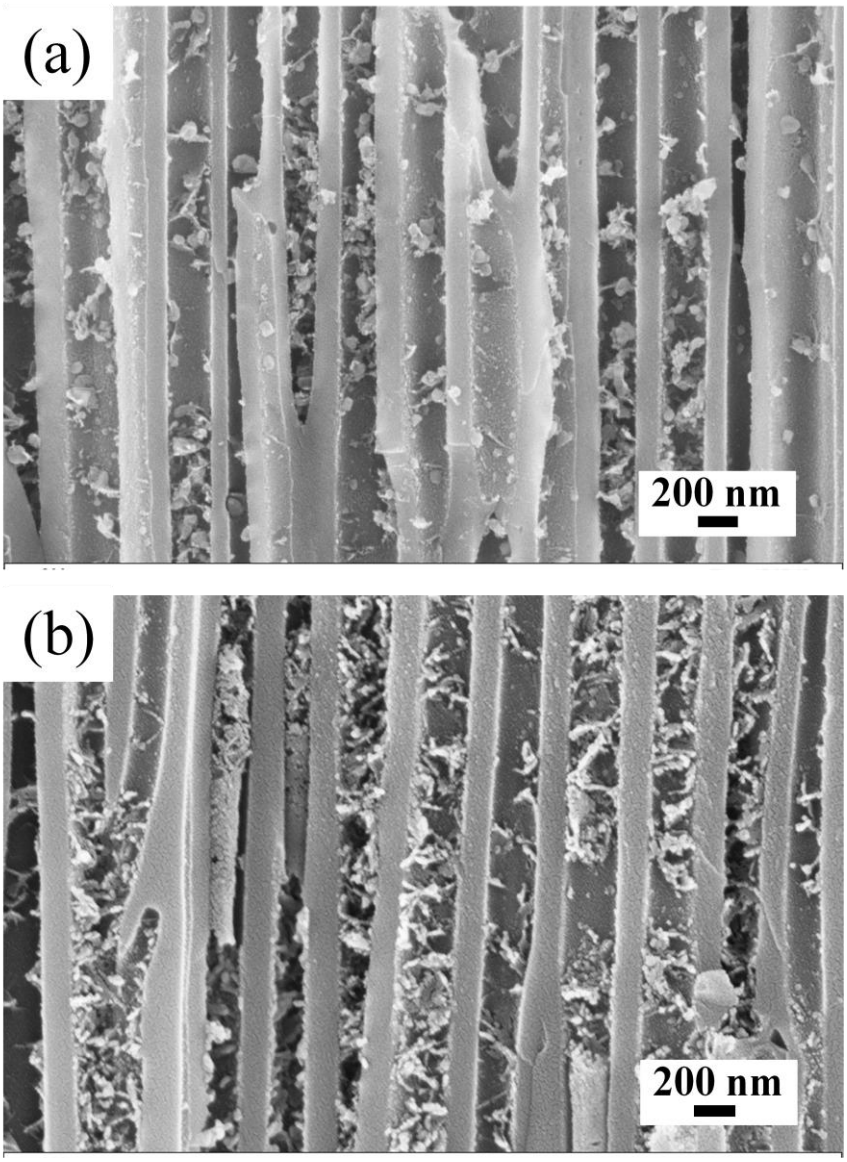

Figure 5.7 FESEM images of Fe_3O_4 nanotubes after heating in H_2/N_2 flowing at 600 ℃; (a) Fe_3O_4-air-hy and (b) Fe_3O_4-ox-hy.

Figure 5.8d indicates a magnetite diffraction ring pattern. Similar results were also observed in Fe_3O_4 nanotubes synthesized after heat treatment of Fe_2O_3-ox as shown in Figures 5.9a, 5.9b, and 5.9c. Also, the resolved lattice fringe of 0.257 nm (Figure 5.9d is quite consistent with (311) plane of the magnetite iron oxide. XRD results (Figures 5.10a and 5.10b) also confirmed that

hematite is converted to magnetite by reduction during heat treatments; patterns show the (220), (311), and (222) set of reflections of magnetite at 2θ = 30º, 35.7º, and 37.5º, respectively. (Partly dissolved alumina templates caused broad peaks near 20~30 and 60~70 degrees.)

Hysteresis loops of Fe_3O_4 nanotubes of Fe_3O_4-air-hy (Figure 5.11a) and Fe_3O_4-ox-hy (Figure 5.11b) were measured at room temperature. When the field is applied parallel (0º) and perpendicular (90º) to the nanotubes, the hysteresis loops show similar coercivity in both directions; the coercivities (Figures 5.11a and 5.11b) are 182 Oe and 194 Oe at 0°, respectively. The FC-ZFC magnetization curves in Figures 5.11c and 5.11d were measured at an applied field of 500 Oe, perpendicular to the wire axis. Magnetic curves in Figure 5.11 show that the materials consist of ferromagnetic nanotubes. Figure 5.11c curves show the Verwey transition (T_V) at about 125 K, which is the characteristic of magnetite.

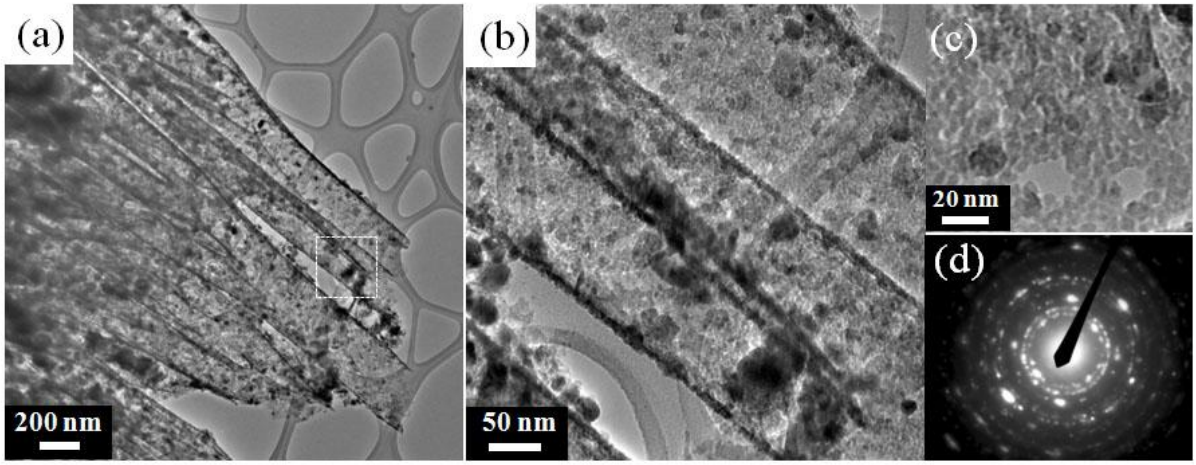

Figure 5.8 (a-c) TEM images and (d) SAED pattern of Fe_3O_4-air-hy after heating in H_2/N_2 flowing at 600 ℃, where the samples are from air-heated Fe_2O_3 (Fe_2O_3-air). (b and c) Images are magnified from the white box in (a) image.

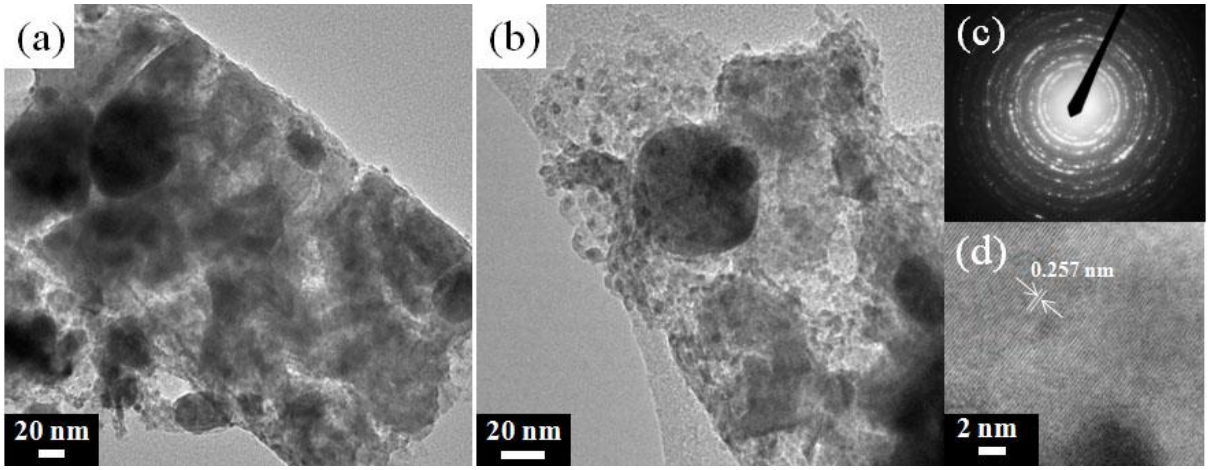

Figure 5.9 (a and b) TEM, (c) SAED pattern, and (d) HRTEM images of Fe_3O_4-ox-hy after heating in H_2/N_2 flowing at 600 ℃, where the samples are from O_2-heated α-Fe_2O_3 (Fe_2O_3-ox). (c and d) Images are consistent with magnetite iron oxide structures with the lattice fringe of 0.257 nm.

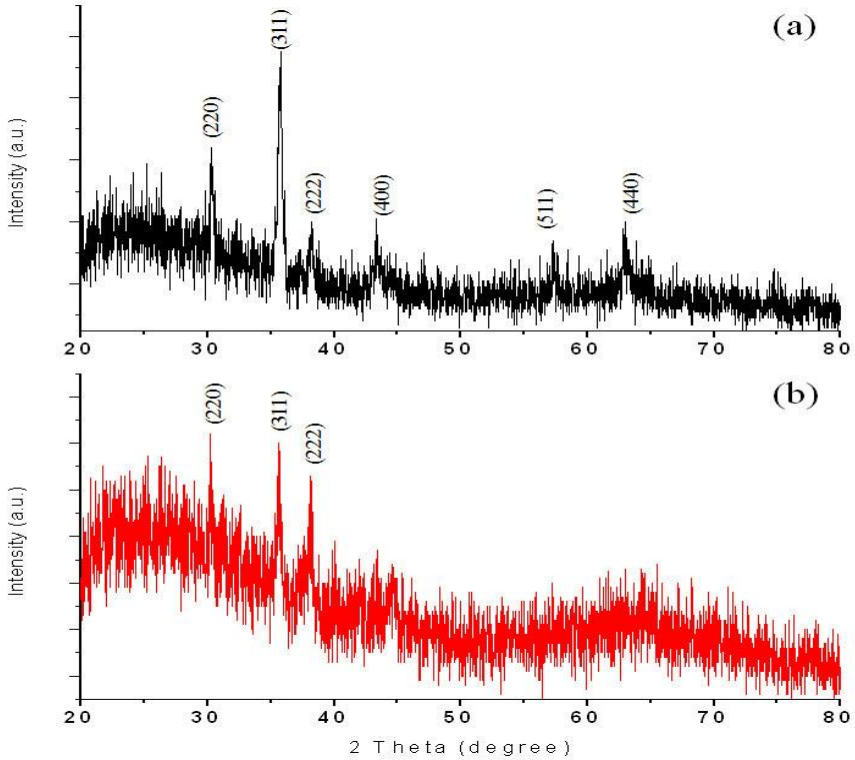

Figure 5.10 XRD results of Fe_3O_4 nanotubes obtained after heat treatments in H_2/N_2 flowing at 600 ℃; (a) Fe_3O_4-air-hy and (b) Fe_3O_4-ox-hy. Broad peaks at 20~30 and 60~70 degrees are from partly dissolved alumina templates.

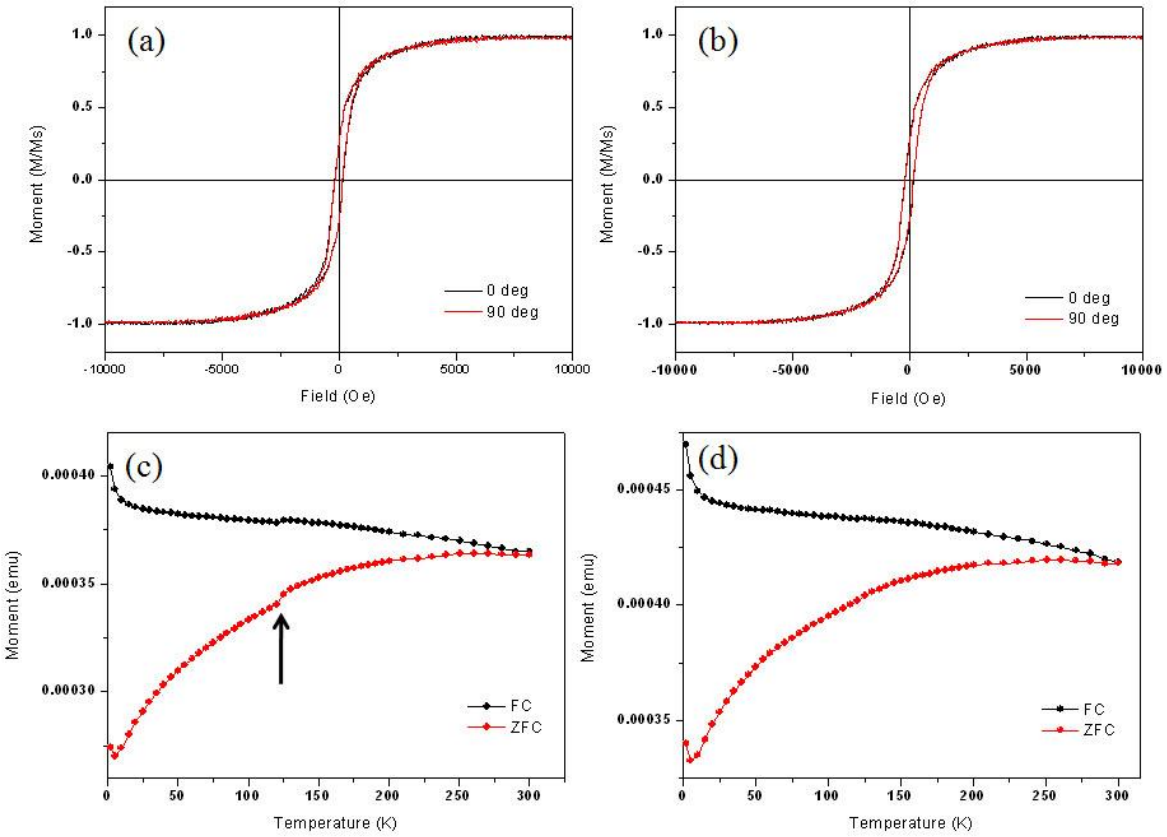

Figure 5.11 Hysteresis loops of Fe_3O_4 nanotubes; (a) Fe_3O_4-air-hy and (b) Fe_3O_4-ox-hy. The magnetic field was applied parallel (0 degree, black) and perpendicular (90 degree, red) to the nanotubes. FC-ZFC magnetization curves of Fe_3O_4 nanotubes; (c) Fe_3O_4-air-hy and (d) Fe_3O_4-ox-hy. The magnetic field of 500 Oe was applied perpendicular (90 degree) to the nanotubes. (c) FC-ZFC curve shows the Verwey transition at about 125 K (indicated with arrow).

5.4 Discussion

Hematite (α-Fe_2O_3) and magnetite (Fe_3O_4) nanotubes were synthesized in alumina templates. The first step in this process is the electrodeposition of β-FeOOH nanotubes from a mixture solution of $FeCl_3$ and $(NH_4)_2C_2O_4$ by an electrodeposition technique (eq. 1 and 2).[13,28] β-FeOOH then serves as a good starting material in the fabrication hematite or magnetite. The β-FeOOH was transformed into α-Fe_2O_3 with heat treatments at 500 ℃ in air or oxygen (eq. 3). The α-Fe_2O_3 then in turn can be reduced to Fe_3O_4 through heat treatments in H_2 gas (eq. 4). The chemical reactions using the various precursors can be described as follows:

$$(NH_4)_2C_2O_4 + 2H_2O \rightarrow 2NH_3 \cdot H_2O + 2CO_2 \quad (1)$$

$$FeCl_3 + 3NH_3 \cdot H_2O \rightarrow FeOOH + 3NH_4Cl + H_2O \quad (2)$$

$$2FeOOH \rightarrow Fe_2O_3 + H_2O \quad (3)$$

$$3Fe_2O_3 + H_2 \rightarrow 2Fe_3O_4 + H_2O \quad (4)$$

β-FeOOH nanowires have been synthesized by Zhang et al.[28] using an AC electrodeposition at high voltage. In our case, we synthesized β-FeOOH nanotube arrays from the same precursor, but under different deposition conditions so as to favor tubular structure formation. The proposed synthetic mechanism is illustrated in Figure 5.12. A thin conducting Ag film with thickness of 200 nm covers one side of pores and small amount of the Ag particles coat inside the pore during sputtering. When the alumina template is soaked in the electrolyte, the pore channels are filled with solution by capillary action, but not completely (Figure 5.12a). After we apply a constant current of -0.5 mA, the reduction process occurs and is favored along the pore wall (Figure 5.12b). β-FeOOH, however, also grows perpendicular to the wall, producing unique

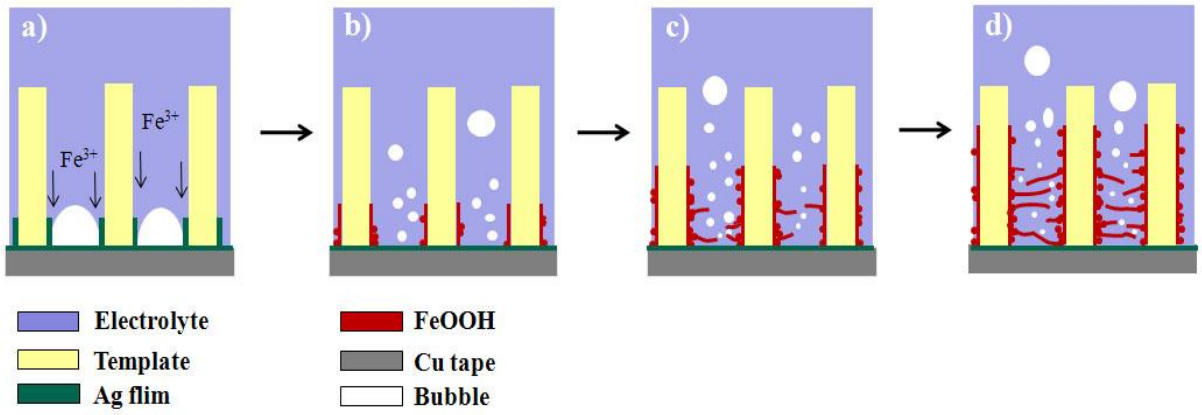

Figure 5.12 Illustration of synthesis procedures of β-FeOOH nanotubes using alumina templates. (a) The alumina template is soaked in the electrolyte. (b) β-FeOOH tubes are rapidly growing along the pore channels. (c) β-FeOOH is also slowly growing perpendicular to the walls of the nanotubes and thin plate-like structures are produced within the tubes. (d) Tubular structures with bridging plate components are continually growing during electrodeposition.

plate structures in the body of the tubes (Figure 5.12c). Even though it is a relatively slow process, bridging plate components may play an important role in tube formation. Bridge structures could limit the further influx of metal ions down the channel as well as block the emission of gases generated by the reduction process (Figure 5.12d), therefore further favoring tube formation by not allowing for extensive growth into the body of the nanotube.

As we mentioned above, α-Fe_2O_3 is well known antiferromagnet with the Morin transition temperature (T_M) of 260 K.[7] However, as the particle size of α-Fe_2O_3 materials becomes smaller, the T_M shifts to lower values.[25-27] Recently, several researchers reported that when particles are 8~20 nm diameters, T_M values are observed at less than 4 K and strongly depend on the size of nanomaterials.[27] In our study, magnetic hysteresis loops and FC-ZFC curves of α-Fe_2O_3 nanotubes (Figures 5.5 and 5.6) showed superparamagnetic properties without the Morin transition because the size of nanoparticles is below 20 nm diameters. Even though the

morphology and size of α-Fe_2O_3 nanotubes are different in Fe_2O_3-air and Fe_2O_3-ox, the magnetic properties are unchanged.

Magnetite Fe_3O_4 is a well known magnetic material with inverse cubic spinel structure (AB_2O_4), where the structure of magnetite Fe_3O_4 is composed of [Fe^{3+}] tetrahedral A site and [$Fe^{2+}Fe^{3+}$] octahedral B site with close-packed O^{2-} ions. Closely spaced Fe^{2+} and Fe^{3+} in the B site permits an easy electron exchange by means of fast electron hopping.[23,29] However, when the products are cooled down to below the critical temperature (T_V) near 120 K, Fe ions in the B site obtain a charge-ordered state with the reduction of the crystal symmetry from cubic to tetragonal; this is called the Verwey transition.[29,30] According to the FC-ZFC curves in Figure 5.11c, the T_V was observed at about 125 K. Interestingly, the magnetic properties of Fe_3O_4 nanotubes produced from Fe_2O_3-air and Fe_2O_3-ox are very similar regardless of the morphology of nanotubes because the nanotubes are composed entirely of small nanoparticles. Even though the T_V was not observed in Fe_3O_4-ox-hy (Figure 5.11d), TEM and XRD results show that the product is magnetite.

5.5 Conclusions

We have found a simple method for efficient synthesis of iron oxide nanotubes by a template-based electrodeposition method. Unlike other metal or metal oxide nanotubes,[31,32] the electrodeposited β-FeOOH nanotubes have plate-like features within the tubes. The length and wall thickness of the nanotubes depend on the duration of electrodeposition. After heat treatments of β-FeOOH nanotubes, the phase of β-FeOOH nanotubes in alumina templates was converted to Fe_2O_3 and Fe_3O_4. In addition, the nanotubes are composed of small nanoparticles and the morphology of inner-face was modified. Hematite Fe_2O_3 nanotubes show

superparamagnetic character and magnetite Fe_3O_4 can exhibit ferromagnetism with the Verwey transition at 125 K. We expect that Fe_2O_3 and Fe_3O_4 nanotubes can be useful to fabricate magnetic/nonmagnetic or magnetic/magnetic core-shell nanowire arrays that have tunable magnetic properties by controlling of interactions between core and shell materials for applications in the fields of nanodevices, biological, or electromagnetic systems.

5.6 References

1. Jiabiao Lian, Xiaochuan Duan, Jianmin Ma, Peng Peng, Tongil Kim, and Wenjun Zheng, *ACS Nano*, **2009**, *3*, 3749.
2. Martin Hermanek, Radek Zboril, Ivo Medrik, Jiri Pechousek, and Cenek Gregor, *J. Am. Chem. Soc*., **2007**, *129*, 10929.
3. Shanta R Bhattarai, Remant B Kc, Sun Y Kim, Manju Sharma, Myung S Khil, Pyoung H Hwang, Gyung H Chung, and Hak Y Kim, *J. Nanobiotech*., **2008**, *6*, 1.
4. Andreas Hofmann, Steffen Thierbach, Annetta Semisch, Andrea Hartwig, Matthias Taupitz, Eckart Rühl, and Christina Graf, *J. Mater. Chem*., **2010**, *20*, 7842.
5. Snajay Mathur, Sven Barth, Ulf Werner, Franciso Hernandez-Ramirez, and Albert Romano-Rodriguez, *Adv. Mater*., **2008**, *20*, 1550.
6. Susanta K. Mohapatra, Shiny E. John, Subarana Banerjee, and Mano Misra, *Chem. Mater*., **2009**, *21*, 3048.
7. Subarna Mitra, Soumen Das, Kalyan Mandal, and Subhadra Chaudhuri, *Nanotechn*ology, **2007**, *18*, 275608.
8. Igor Chourpa, Laurence Douziech-Dyrolles, Lazare Ngaboni-Okassa, Jean-Francois Fouquenet, Simone Cohen-Jonathan, Marin Soucé, Hervé Marchais and Pierre Dubois, *Analyst*, **2005**, *130*, 1395.
9. Jinwoo Cheon, Nam-Jung Kang, Sang-Min Lee, Jae-Hyun Lee, Ji-Hyun Yoon, and Sang Jun Oh, *J. Am. Chem. Soc*., **2004**, *126*, 1950.
10. Miaomiao Ye, Serkan Zorba, Le He, Yongxing Hu, Randolph Thomas Maxwell, Constantine Farah, Qiao Zhang, and Yadong Yin, *J. Mater. Chem*., **2010**, *20*, 7965.
11. Shao-Min Zhou, Xing-Tang Zhang, He-Chun Gong, Bin Zhang, Zhi-Shen Wu, Zu-Liang Du, and Si-Xin Wu, *J. Phys.: Condens. Matter*, **2008**, *20*, 075217.
12. Lorenza Suber, Patrizia Imperatori, Giovanni Ausanio, Fabio Fabbri, and Herbert Hofmeister, *J. Phys. Chem. B* **2005**, *109*, 7103.
13. D. S. Xue, C. X. Gao, Q. F. Liu, and L. Y. Zhang, *J. Phys.: Condens. Matter*, **2003**, *15*, 1455.
14. Zhenmeng Peng, Mingzai Wu, Ying Xiong, Jun Wang, and Qianwang Chen, *Chem. Lett*., **2005**, *34*, 636.
15. Albert G. Nasibulin, Simas Rackauskas, Hua Jiang, Ying Tian, Prasantha Reddy Mudimela, Sergey D. Shandakov, Larisa I. Nasibulina, Jani Sainio, and Esko l. Kauppinen, *Nano Res*., **2009**, *2*, 373.

16. Jun Chen, Lina Xu, Weiyang Li, and Xinglong Gou, *Adv. Mater*., **2005**, *5*, 582.
17. Jinping Liu, Yuanyuan Li, Hongjin Fan, Zhihong Zhu, Jian Jiang, Ruimin Ding, Yingying Hu, and Xintang Huang, *Chem. Mater*., **2010**, *22*, 212.
18. J. Escrig, M. Daub, P. Landeros, K. Nielsch, and D. Altbir, *Nanotechnology*, **2007**, *18*, 445706.
19. M. Venkata Kamalakar, and Arup K. Raychaudhuri, *Adv. Mater*., **2008**, *20*, 149.
20. Xiu-Feng Han, Shahzadi Shamaila, Rehana Sharif, Jun-Yang Chen, Hai-Rui Liu, and Dong-Ping Liu, *Adv. Mater*., **2009**, *21*,1.
21. Tao Wang, Ying Wang, Fashen Li, Chongtao Xu, and Dong Zhou, *J. Phys.: Condens. Matter*, **2006**, *18*, 10545.
22. Kristina Pitzschel, Josep M. Montero Moreno, Juan Escrig, Ole Albrecht, Kornelius Nielsch, and Julien Bachmann, *ACS Nano*, **2009**, *3*, 3463.
23. Chun-Jiang Jia, Ling-Dong Sun, Zheng-Guang Yan, Yu-Cheng Pang, Li-Ping You, and Chun-Hua Yan, *J. Phys. Chem. C* **2007**, *111*, 13022.
24. Jin-Hee Lim, Aurelian Rotaru, Seong-Gi Min, Leszek Malkinski, and John B. Wiley, *J. Mater. Chem*., **2010**, *20*, 9246.
25. M. Chirita, and I. Grozescu, *Chem. Bull. "POLITEHNICA" Univ.*, **2009**, *54*, 1.
26. Lu Liu, Hui-Zhong Kou, Wenling Mo, Huajie Liu, and Yuqui Wang, *J. Phys. Chem. B* **2006**, *110*, 15218.
27. Feng Jiao, Andrew Harrison, Jean-Claude Jumas, Alan V. Chadwick, Winfried Kockelmann, and Peter G. Bruce, *J. Am. Chem. Soc*., **2006**, *128*, 5468.
28. Liying Zhang, Yafei Zhang, *J. Mag. Mag. Mater*., **2005**, *321*, L15.
29. Friedrich Walz, *J. Phys.: Condens. Matter*, **2002**, *14*, R285.
30. Wendong Wang, Minhui Yu, Matthias Batzill, Jibao He, Ulrike Diebold, and Jinke Tang, *Phys. Rev. B* **2006**, *73*, 134412.
31. Dongdong Li, Richard S. Thompson, Gerd Bergmann, and Jia G. Lu, *Adv. Mater*., **2008**, *20*, 4575.
32. Min Lai, Jae-Hong Lim, Syed Mubeen, Youngwoo Rheem, Ashok Mulchandani, Marc A Deshusses, and Nosang V Myung, *Nanotechnology*, **2009**, *20*, 185602.

Chapter 6

Metal Nanowire Arrays in Pre-patterned AAO Templates

6.1 Introduction

The miniaturization of electronic and mechanical devices is becoming more important in recent years because small features can result in increasingly higher speeds and decreasing energy consumption.[1,2] The fabrication of small devices with high quality requires cutting edge lithography techniques such as photolithography, nanosphere lithography, electron-beam (e-beam) lithography, imprinting lithograph, etc.[3]

Recently, lithography techniques have been employed for patterning of metallic nanowires, carbon nanotubes, porous thin films, nanoparticles, and nanospheres.[2,4-11] In general, patterned structures are placed on the silicon substrate, but the restricted length of polymer resist is limited the length of nanostructures.[12] For fabrication of patterned arrays, most people used a lift-off process in which the metal is vapor deposited through a line mask. The width and length of metal are determined lithographically, and the limited thickness of the metal is controlled during the deposition process.[13]

Several researchers have also used porous AAO templates as a substrate instead of silicon and produced nanowires with high aspect ratios in the pre-patterned AAO by electrodeposition. Li et al.[6] reported the patterned metal nanowire arrays by photolithography. Selectively opened pore channels were produced on the template during UV exposure and developing processes, and the opened pores allowed the nanowire growth in the channels by electrodeposition after coating the open pore surface with conducting metal. The patterned metal nanowires with defined structures

were observed in the desired location after removing of templates. However, photolithography always requires photomasks to direct photons to a certain location and is difficult to create nanoscale patterned nanowire arrays.

In this chapter, patterned metal nanowire arrays fabricated by either nanosphere lithography or e-beam lithography are discussed. In case of nanosphere lithography, it uses colloidal spheres as a mask to make arrays of patterned nanostructures. Between neighboring spheres are formed holes and the size of holes between spheres is determined by the size of the colloidal particles that form the mask.[14-16] The nanosphere lithography is a simple, fast, and inexpensive method to pattern substrates over large area.[1] Highly ordered sphere arrays can be used to create interstitial triangular structures,[17] metallic rings,[18] nanopillars,[19] and multilayers with modified topography[20]. Vossen et al.[16] modified the hole sizes of colloidal masks to prepare a thin layer of silica by a simple wet-chemical method. Hexagonal-patterned Si nanowires,[14] ZnO nanorods[21] or carbon nanotubes[22] have been produced by this approach. Unlike nanosphere lithography, e-beam lithography is a sophisticated nanofabrication tool based on a highly focused electron beam that allows very high resolution direct-write patterning on electron beam sensitive resists.[23] E-beam lithography systems can easily produce designed nanostructures on a substrate for applications such as field emitters,[24] transistors,[25] and sensor devices.[26]

Here we patterned the surface of AAO templates by either nanosphere lithography or e-beam lithography. Nanostructures were grown in the patterned pore channels by electrodeposition. We are able to control both the design and size of nanostructures such that single nanowire arrays can be fabricated, where the smallest diameter of single nanowire is about 80 nm.

6.2 Experimental

6.2.1 Nanosphere Lithography

Conventional AAO templates with pore diameters of 60 nm and interpore distances of 100 nm were fabricated by two-step anodization as described in Chapter 2. Polystyrene (PS) spheres with 100, 200 nm, and 950 nm diameters were purchased from Bangs Laboratories Inc. and were used as shadow masks. Ordered and close-packed PS sphere arrays were obtained on the membrane by spin coating at 3000 rpm using an aqueous 10 wt% PS sphere solution. Synthetic procedures are illustrated in Figure 6.1. After Ag or Au sputtering on the well-ordered PS spheres (Figure 6.1a), metal nanowires in the membrane are electrodeposited at -0.9 mA for 15 min (Figure 6.1b). Cup-shaped nanostructures can be produced by dissolving away all the PS spheres and AAO template after simple coating of PS spheres (Figure 6.1c). Before the etching of AAO templates, PS spheres were removed by CH_2Cl_2 and by subsequent rinsing in acetone and water. In some cases, the Ag film coated on AAO was dissolved in concentrated HNO_3 for 5 min.

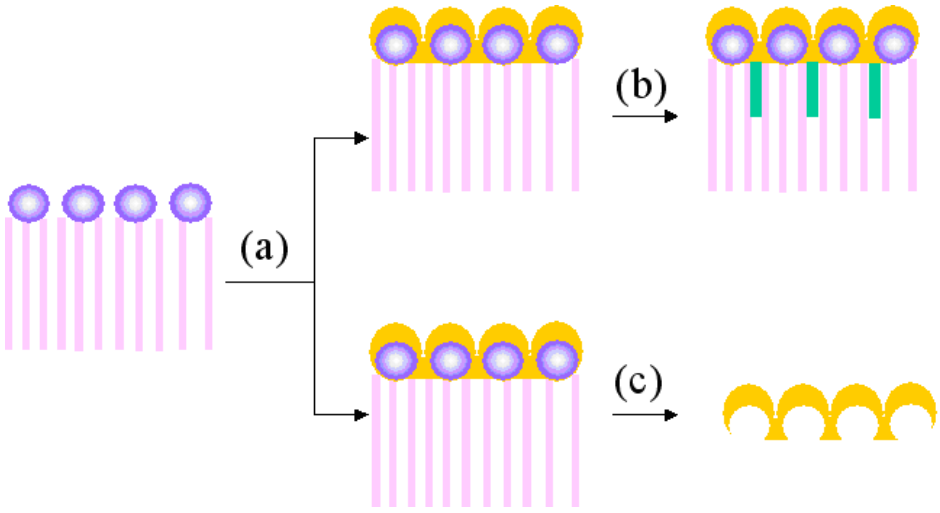

Figure 6.1 Schematic diagram of patterning of nanowires and cup-shaped structures; (a) Ag coating on ordered PS spheres, (b) electrodeposition, and (c) removal of spheres and membrane.

6.2.2 E-beam Lithography

E-beam lithography is a method that allows an image to be transferred to a substrate without the use of mask. In our experiments, we used Au coated AAO templates as a substrate and poly(methylmethacrylate) (PMMA) was employed as a resist. The fabrication procedure of patterned nanowires is illustrated in Figure 6.2. PMMA was spin coated on the AAO template at 3000 rpm for 60 sec and the template was then baked at 170 ℃ for 60 sec. The e-beam lithography was performed using field emission scanning electron microscope (FESEM, LEO 130 VP) at 10 kV with JC Nabity nanometer pattern generation system. To get high resolution patterned images on PMMA, we found the best imaging conditions at 10 kV, over 10000x magnification and move the beam to the dumped part of the substrate to adjust the focus and check the beam current. Finally, the beam was moved to the end of AAO substrate at low magnification. After e-beam patterning, the resist was developed in a solution of 1:3 methylisobutylketone (MIBK) and isopropyl alcohol (IPA) for 70 sec. The template was rinsed in IPA and water for 60 sec. The electron-beam exposed resist was removed, opening up selective arrays of the porous membrane. Finally, the open pores can be filled with metal nanowires by an electrodeposition. Electrodeposition was carried out at -0.9 mA on a Princeton Applied Research VMP2. For the observation of patterned nanowires, CH_2Cl_2 and 0.1 M NaOH were used to remove the PMMA and AAO template, respectively.

6.2.3 Characterization

For imaging, we used an optical microscope (OM: Olympus BX51), field-emission scanning electron microscopy (FESEM: LEO 130 VP), and transmission electron microscopy (TEM: JEOL 2010). Magnetic hysteresis loops were measured by a superconducting quantum interface

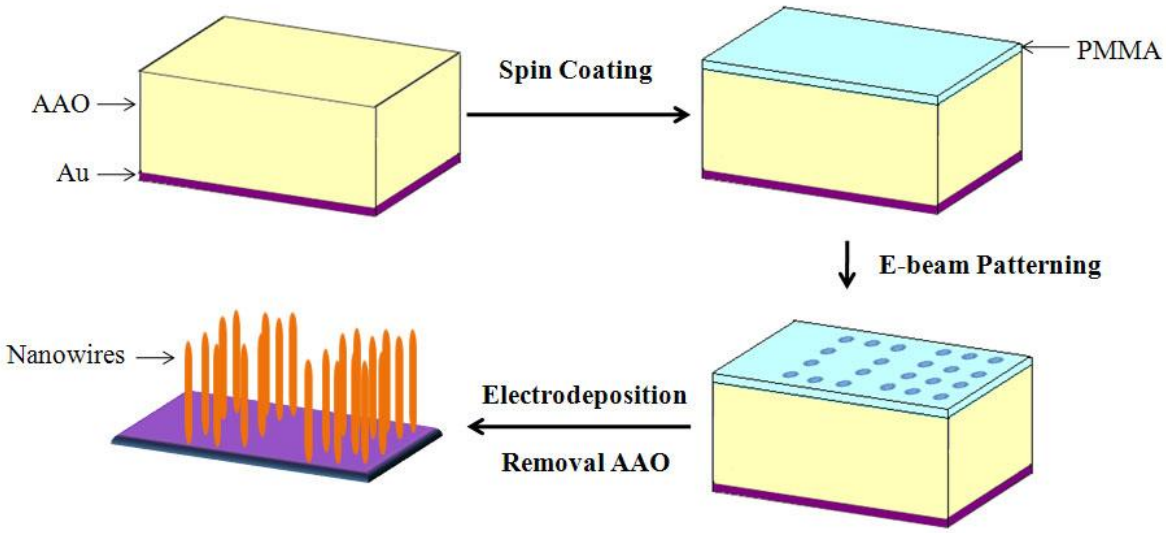

Figure 6.2 Schematic diagram of synthetic procedures of patterned nanowire arrays on AAO templates.

device (SQUID: Quantum Design MPMS XL) at room temperature.

6.3 Results and Discussion

6.3.1 Patterned Nanowire Arrays by Nanosphere Lithography

Figure 6.3a images show that almost all of the pores of the AAO are closed with PS spheres when we used PS with 100 nm diameters. However, if we choose 950 nm PS spheres, not all the AAO pores are blocked so that nanowire growth can take place. Figure 6.3b shows the ordered PS spheres on AAO templates. The open space between neighboring spheres is marked with red-triangles in the inset of Figure 6.3b. The size of space is about 400 nm. PS spheres with the diameter of 200 or 300 nm didn't show any patterning on AAO templates with 100 nm interpore spaces. The concaved top surface caused by pore channels in AAO obstructed the hexagonally ordered patterning of PS spheres.

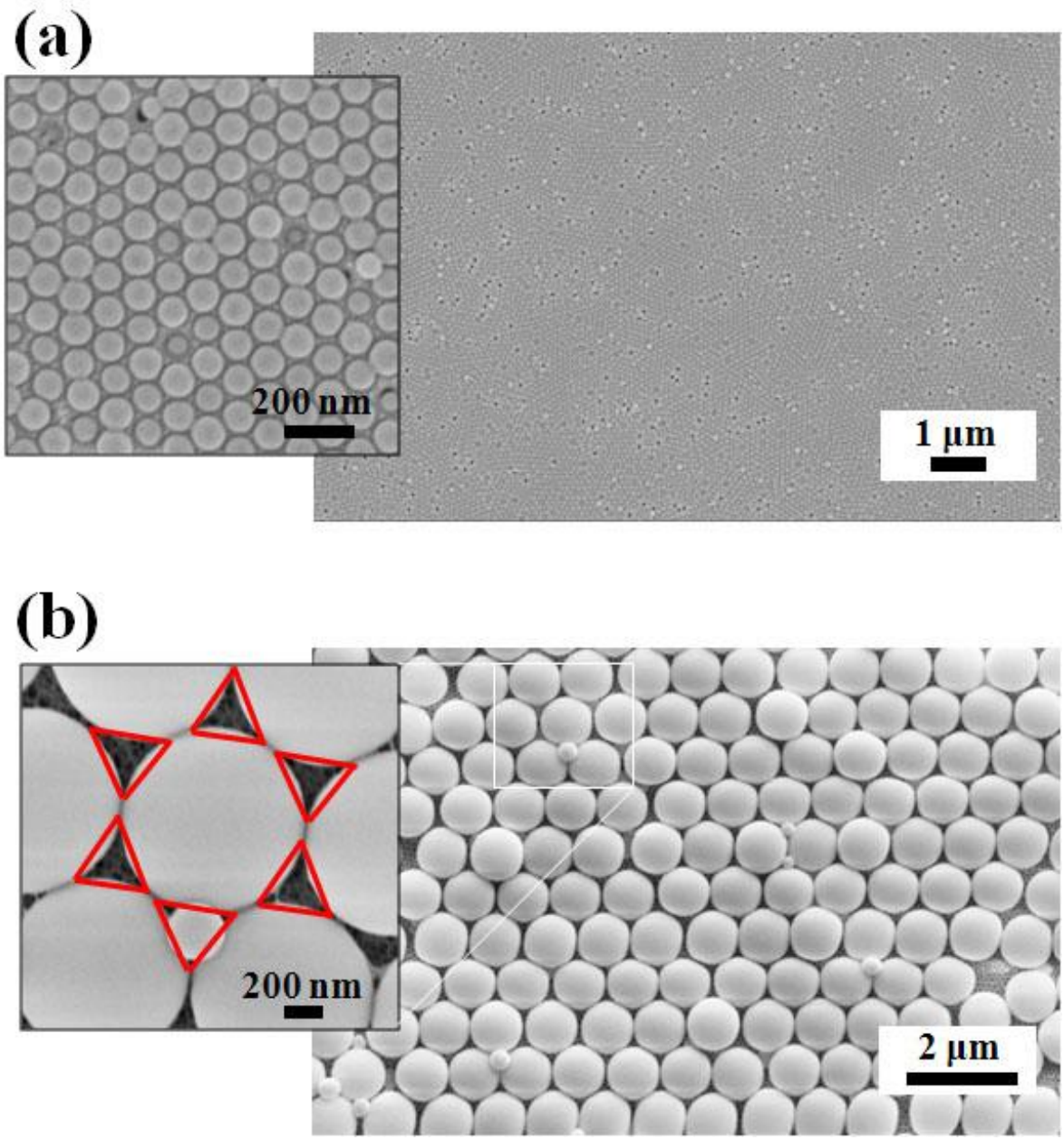

Figure 6.3 FESEM images of ordered PS spheres on AAO templates; (a) 100 nm and (b) 950 nm PS spheres. Inset shows how the spheres are ordered on templates. 100 nm PS spheres are closed all pores and 950 nm PS, however, can make open pore channels as shown in (b).

By using a combination of sputtering and electrodeposition, with the self-assembled sphere arrays, we can then make a series of structures with unusual cup-shaped features as shown in Figures 6.1. Both 100 nm and 950 nm PS spheres produced cup-shaped structures as shown in Figures 6.4 and 6.5. In case of 100 nm PS, spheres are coated with a 20 nm thick layer of Au. This is enough to cover the top of the spheres but not enough to connect them all. Au coated PS spheres on AAO were easily dispersed in ethanol by ultra-sonication and porous thin Au layers were produced on the membranes as shown in Figure 6.4a. The dispersed Au coated PS spheres were observed by TEM in Figure 6.4b. Half of the PS spheres were covered with Au. The PS can then be dissolved with CH_2Cl_2 to produce the cup-shaped nanostructures with 100 nm diameters (Figure 6.4c). The sphere size and their packing geometries highly affect the resulting nanostructured arrays. Figure 6.5 images show cup-shaped structures on AAO templates. These can serve as a conducting film to grow patterned nanostructures. In contrast, the metal film sputtered on 950 nm PS spheres did not corresponding to the triangle pattern that we expected in Figure 6.3b. When we sputtered a metal film on the sample, the metal covered all around the spheres and created the cup-shaped patterning on the membranes. The outer diameter of cup-shaped structures is about 1 μm and the inner diameter corresponded to the size of PS spheres in the mask.

Using 100 nm PS spheres, we cannot produce any patterned nanowire arrays because all the pore channels were closed. However, by dissolving metal covered PS spheres on AAO template, pores can be reopened and spherical empty spaces were obtained in the conducting metal film (Ag). Finally, Au nanowires can grow in each pore channels by a normal electrodeposition process.[27,28] Figure 6.6a image shows the Au nanowire arrays with spherical features at the tips, where the spherical area was hollow. Figure 6.6b image was obtained after removal of Ag film

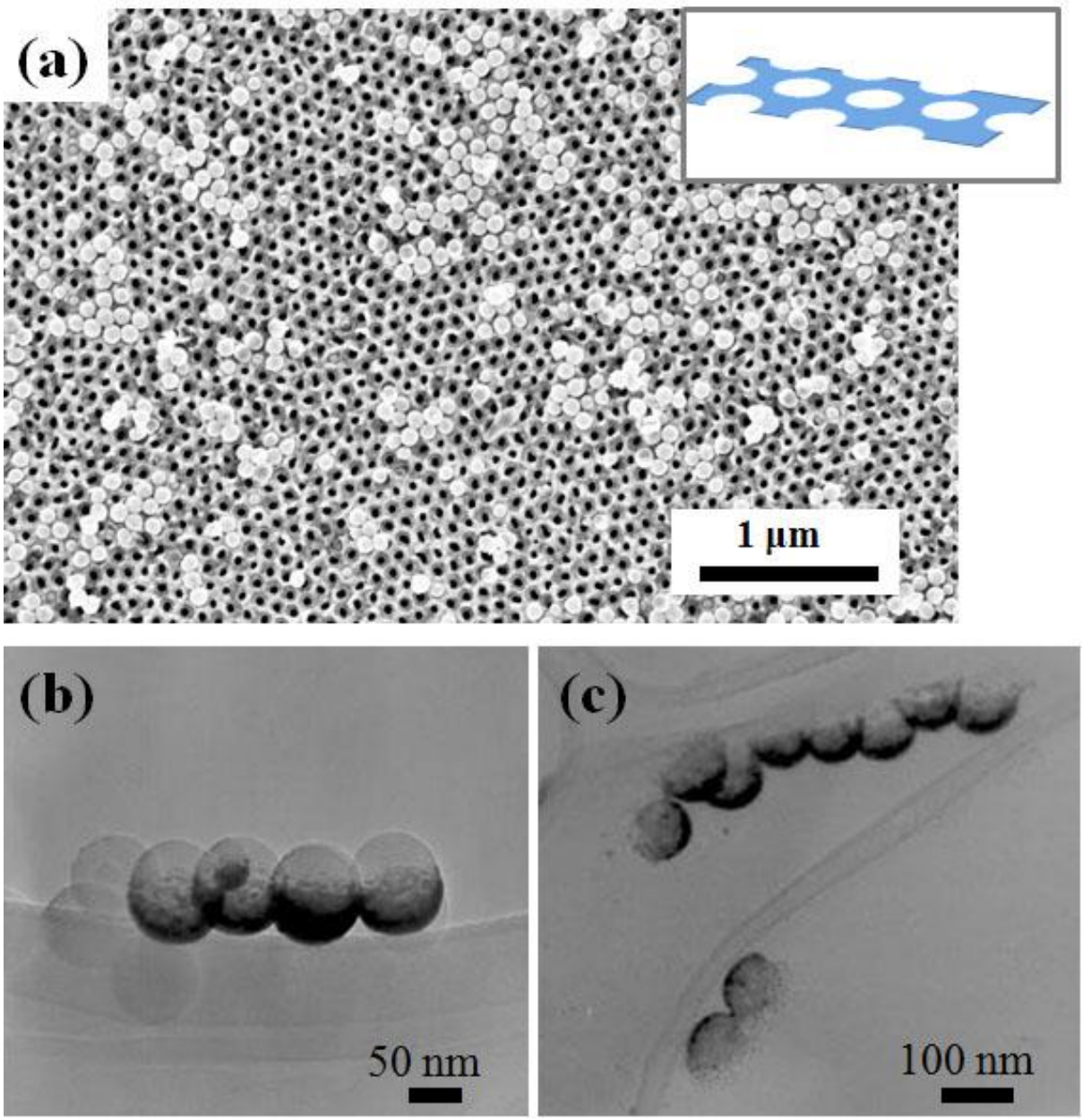

Figure 6.4 (a) FESEM image of porous thin Au film on AAO templates after removal of Au coated PS by ultra-sonication. TEM images of nanometer scale cup-shaped Au on the PS spheres (b) and without PS spheres (c).

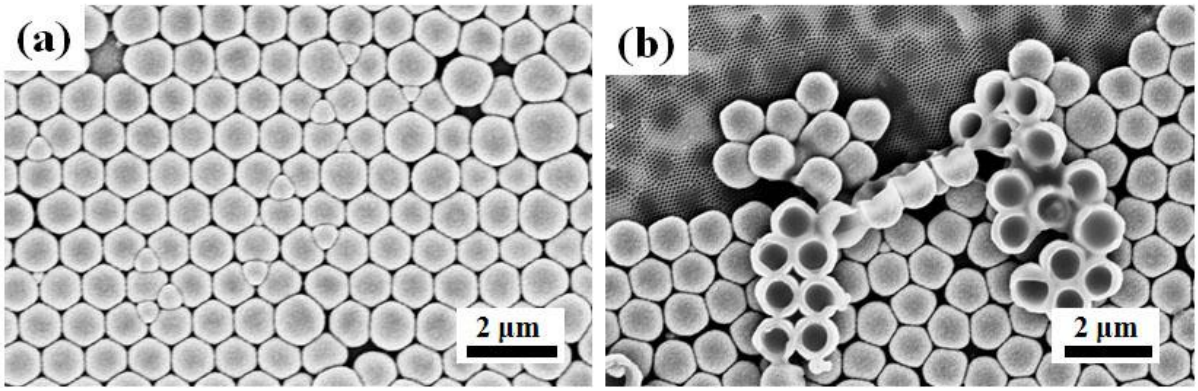

Figure 6.5 FESEM images of Ag cups with 1 μm outer diameter on AAO templates.

and AAO templates by using concentrated HNO_3, and 0.1 M NaOH, respectively. Figure 6.6 clearly shows the unusual morphology. In some cases, the spherical region of nanowire was disappeared during sample preparation.

In the growth of nanowires from 950 nm PS sphere arrays, Ag cups on AAO templates were employed as the working electrode in Au nanowire electrodeposition. Figure 6.7 shows patterned Au nanowire arrays on Ag cups. The patterns correspond well to the expected cup-shape pattern. Figure 6.7a shows the cross-section view of both Ag cups and Au nanowire arrays; while Figure 6.7b provides a schematic presentation of the structure. Top surface of nanostructures also shows the patterned arrays of 1 μm Au nanowires.

This technique is a low cost and simple method for growing patterned nanowire arrays based on the self-assemble of PS spheres on AAO templates. The size and geometry of PS spheres are very important in making patterned nanowire arrays. Through this technique we produced nanowires with spherical features at one end of wire. In addition, the cup-shaped nanostructures are readily prepared by simple sputtering. These can then be used as a working electrode to grow

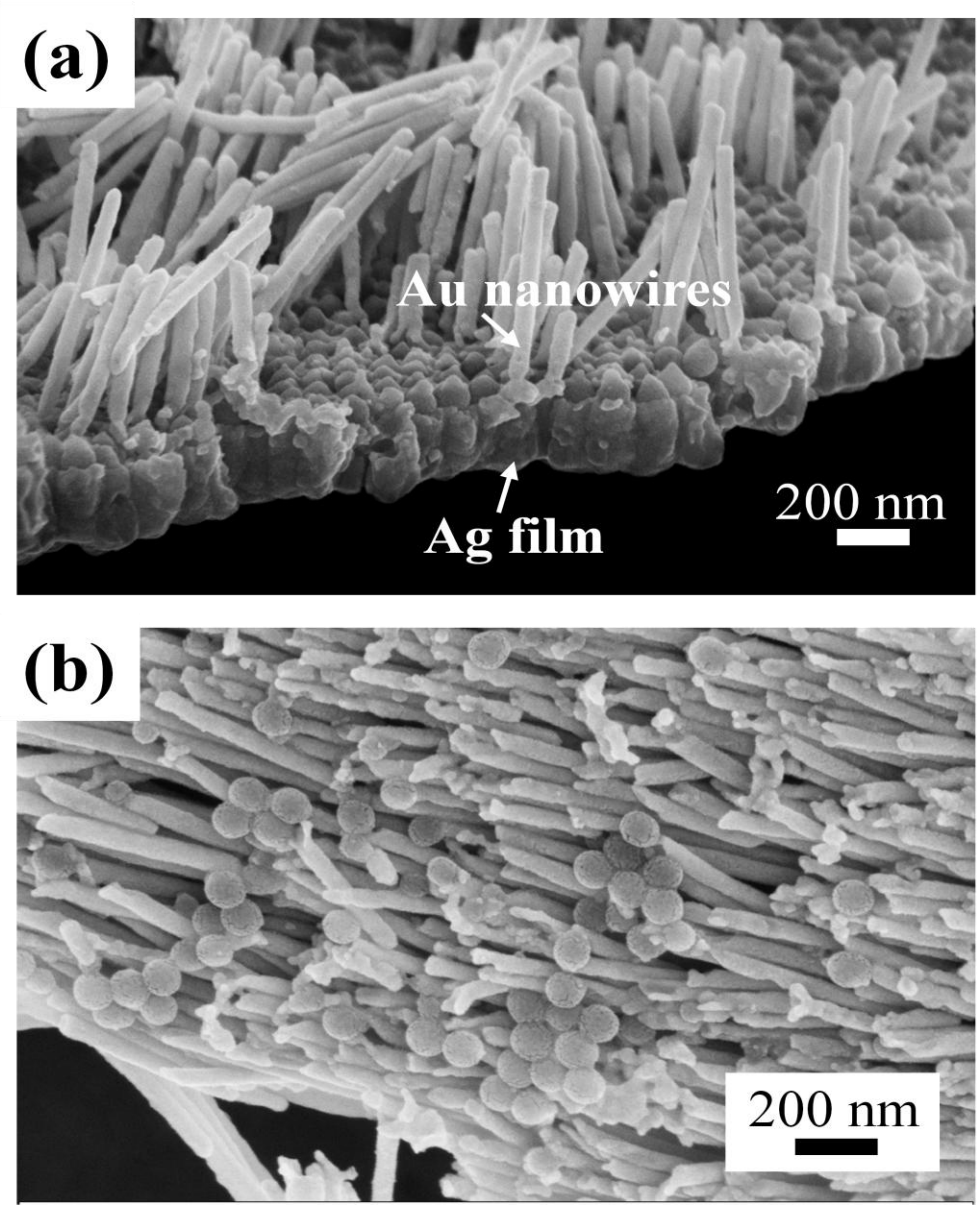

Figure 6.6 FESEM images of (a) Au nanowires on Ag film after removal of AAO templates and (b) Au nanowires after removal of both Ag film and templates. When 100 nm PS spheres are coated on AAO templates with 100 nm interpore distances, no patterned structures are observed.

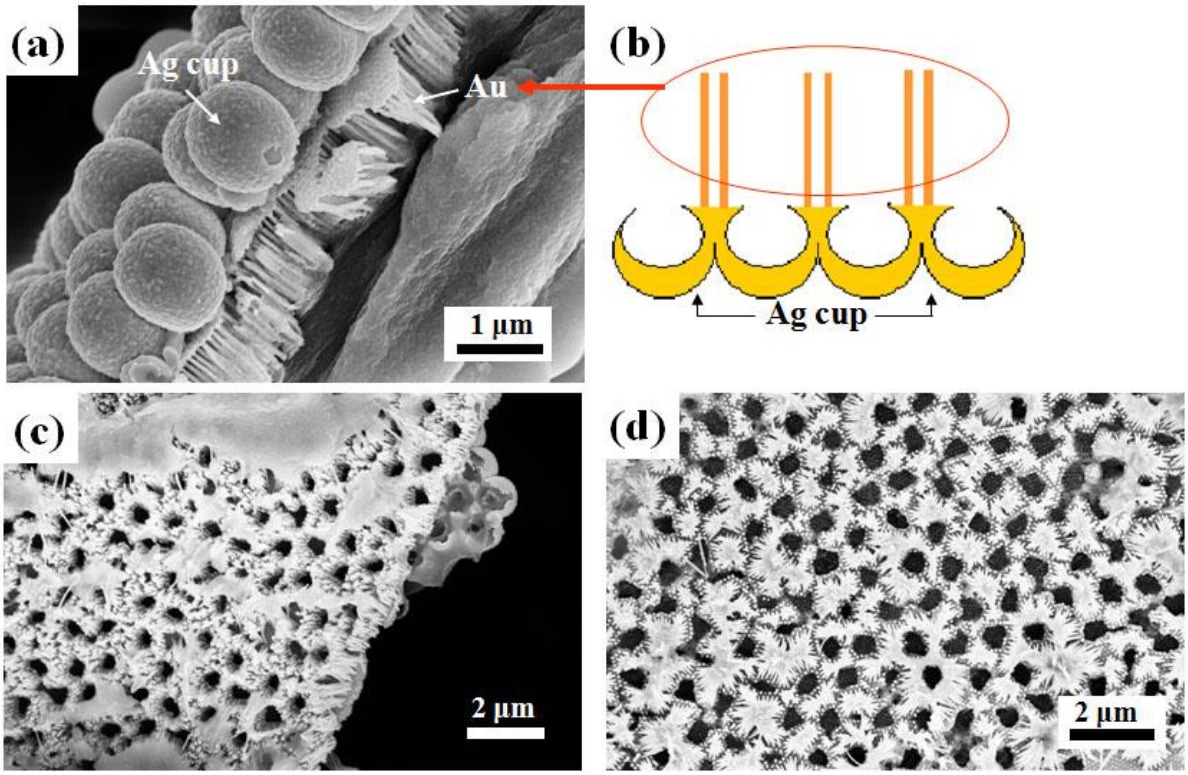

Figure 6.7 FESEM image of patterned Au nanowire arrays on Ag cups; (a) cross-section view, (b) illustration of its morphology, (c) tilted image, and (d) top surface view of nanostructures.

nanowires. The diameter and interwire distances can be also controlled by templates. However, the nanosphere lithography cannot be readily varied so as to direct detailed features of nanowire arrays.

6.3.2 Patterned Nanowire Arrays by E-beam Lithography

E-beam lithography is one of the most widely used techniques to produce patterned nanoarchitectures,[29] electrodes,[30] or 3D nanostructures[31] at specific positions. Herein we describe the patterned metal arrays of various feature sizes and shapes synthesized by the combination of template-based electrodeposition and e-beam lithography techniques.

Figure 6.8 shows portrait images of former Korean President Moo-Hyun Roh. The pattern was obtained by drawing 700 nm diameter small dots on the original photo. After e-beam patterning on PMMA, optical image was obtained and shows a clear pattern on the substrate. For the patterning, we used normal AAO templates as a substrate synthesized by two-step anodization in 0.3 M $H_2C_2O_4$ for 2 h as described in Chapter 2. The template has interpore distances of 100 nm and 15 μm length (growth rate: 7.5 μm/h). The pre-patterned AAO template was connected to the electrode to grow Ni nanowires at the patterned position by electrodeposition. After the electrodeposition and removal of PMMA, we can still see the portrait image on the AAO templates. The optical micrograph in Figure 6d shows free standing nanowire arrays without the template. For more detailed observation of patterned structures, we employed FESEM as shown in Figure 6.9. It shows that the pattern structures are composed bundles of Ni nanowires, which exist at specific positions to form a portrait image. Figure 6.9a image corresponds well to Figure 6.8d. High magnification images show that the portrait consists of bundle of Ni nanowires with the length of 15 μm. Some of the nanowires grew at the top of the templates during electrodeposition and formed large particles at their tips as shown in Figure 6.9d.

With e-beam lithography we can readily vary the features and sizes of patterned structures by using a computer program; no masks are required like in photolithography. The ‘UNO’ feature shown in Figure 6.10a consists lines 9.5 μm wide made up of 40 nm diameters Ni nanowires. Other patterns of simple lines are achieved as shown in Figures 6.10b-d. The patterned Au nanowires have 10 μm lengths and the width of 5 μm in Figure 6.10b. The line length can be extended to several micron sizes and the width of lines can also be reduced in Figure 6.10c. In addition, Figure 6.10d shows we can control the distance between two lines. Au dot arrays with 1 μm diameters were prepared on hard side of Mi-Ha AAO in Figure 6.11a. The dots were used as

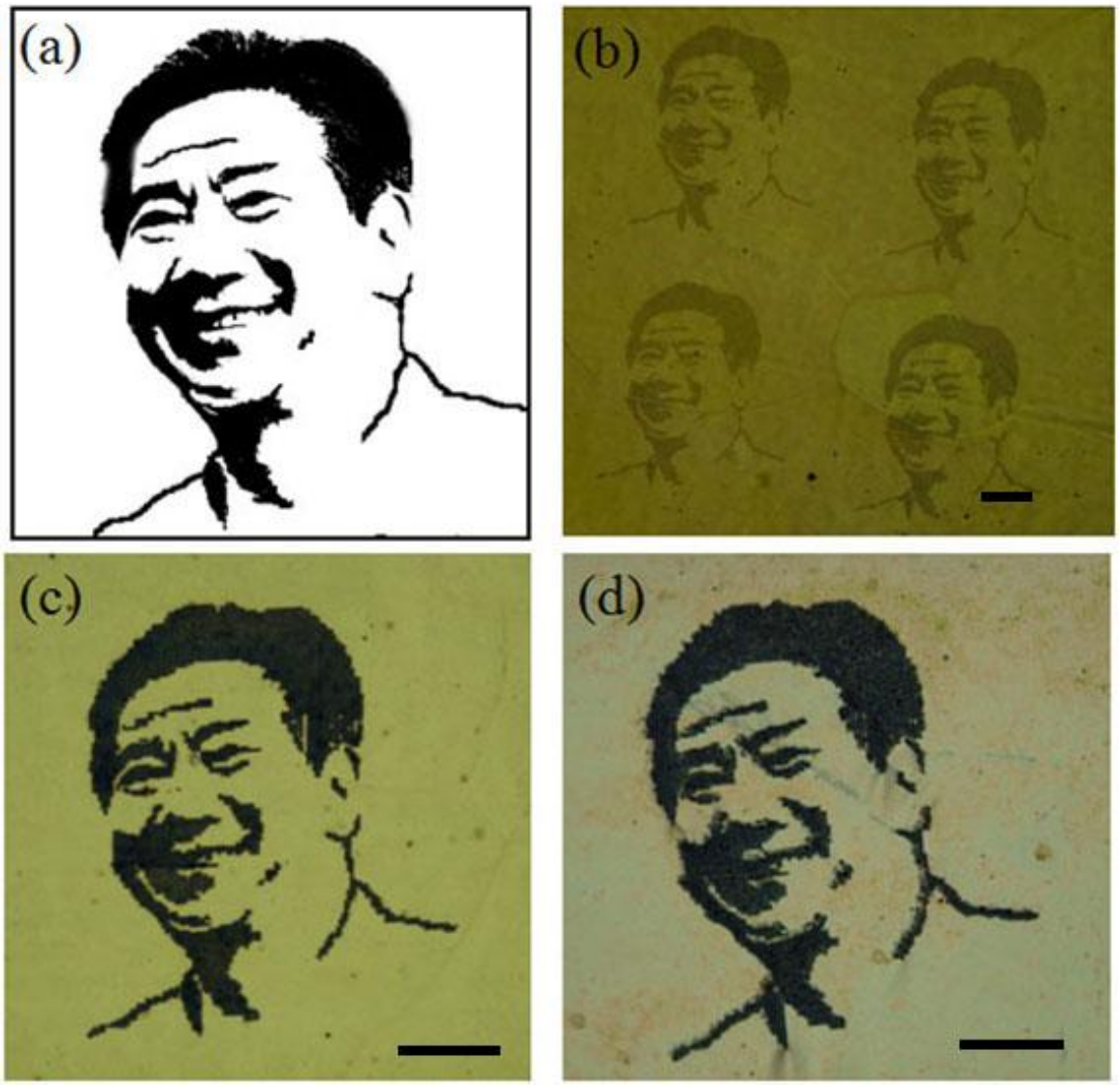

Figure 6.8 (a) Original portrait image of former Korean President Moo-Hyun Roh. Optical micrographs of a portrait, Moo-Hyun Roh; (b) e-beam patterning, (c) Ni electrodeposition and removing of PMMA, and (d) free standing Ni nanowires after removing of AAO template. Scale bar is 100 μm.

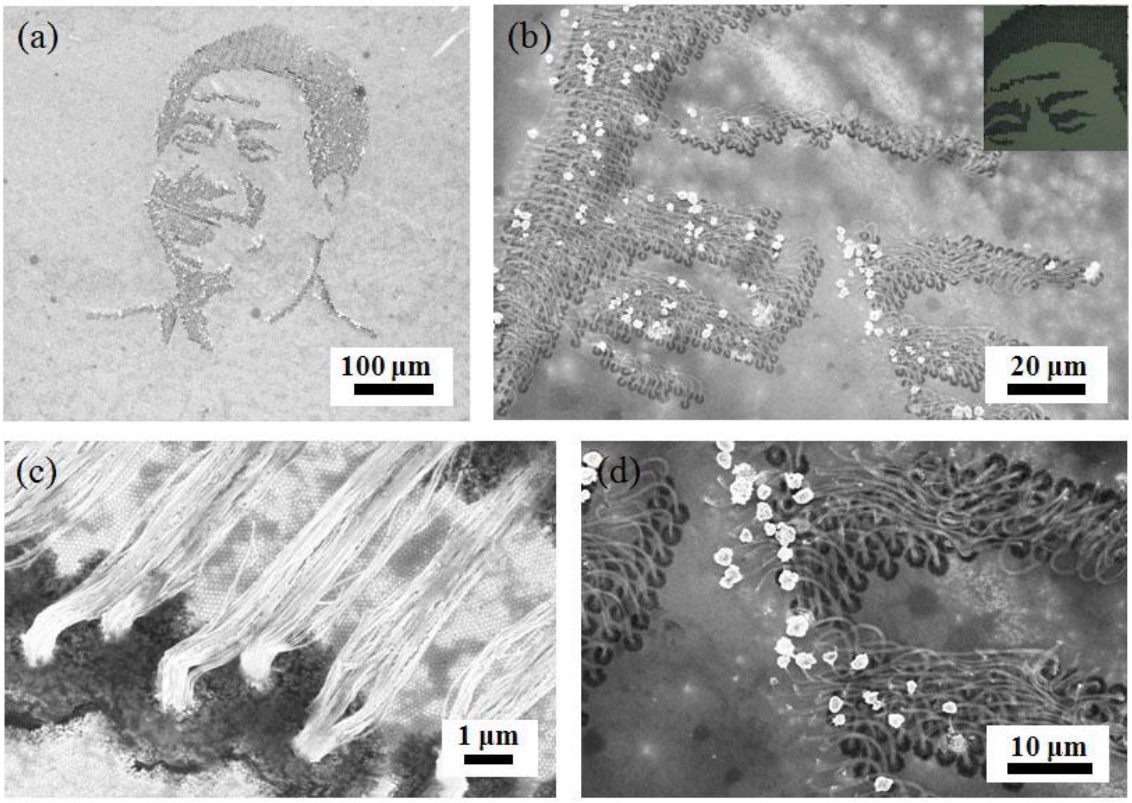

Figure 6.9 FESEM images of patterned nanowire corresponding to Figure 6.8. (a) Patterned portrait is composed bundle of Ni nanowires with 70 nm diameters. (b-d) Magnified images show detail nanowire structures grown each dots. The length of nanowires is about 15 µm. Some nanowires were over grown and show large particles at the end of the nanowires.

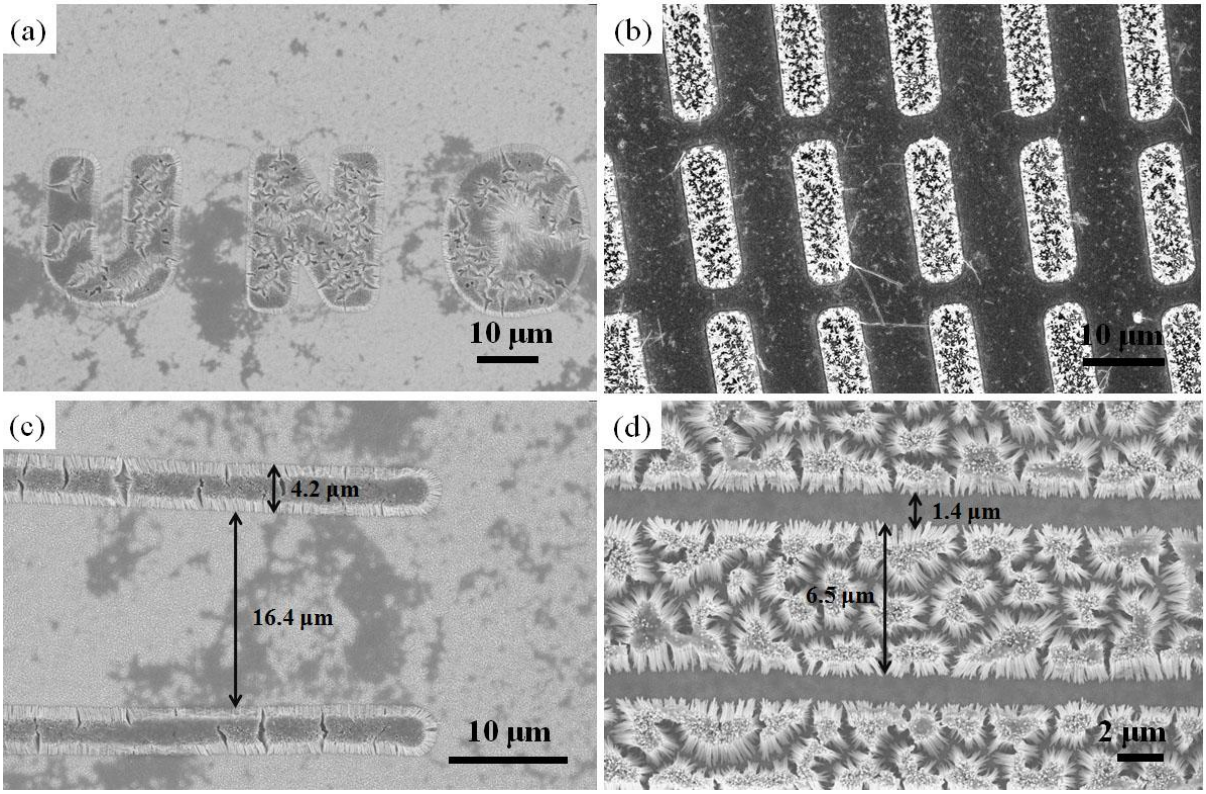

Figure 6.10 FESEM images of patterned nanowire arrays with different designs; (a) Ni nanowire arrays with line width of 9.5 µm in 'UNO', (b) Au nanowires with line width of 5 µm in squares, Ni nanowires with line width of (c) 4.2 µm and (d) 6.5 µm in simple line patterns.

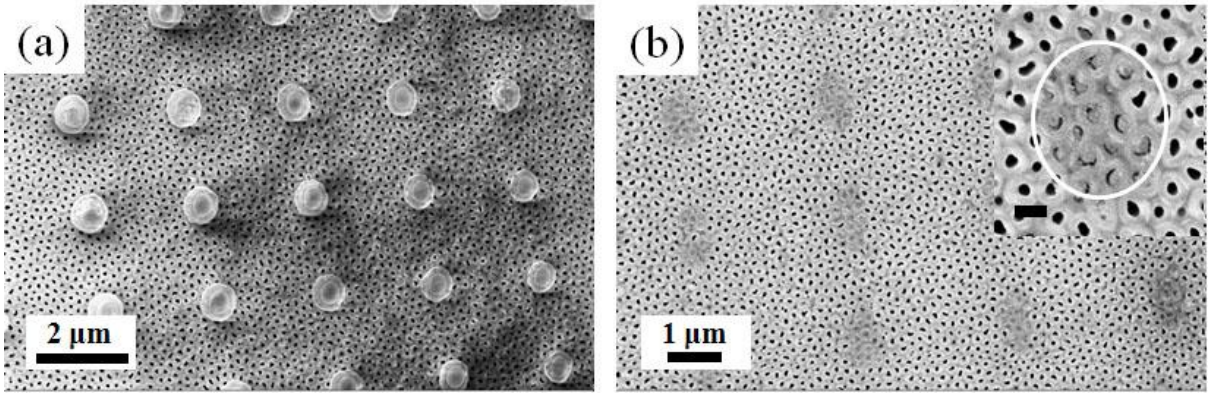

Figure 6.11 FESEM images of (a) patterned Au dot arrays on Mi-Ha AAO and (b) Ni nanowires in hard side of Mi-Ha AAO. Inset shows magnified image of Ni nanowires. Scale bar is 200 nm.

a conducting electrode to fabricate Ni nanowires. After removal of Au dots, we can find the nanowires grown in the selected pores in the template as seen in Figure 6.11b. It is clear that the pre-patterned AAO templates are very useful to create patterned nanostructures with high aspect ratio.

This method allows one to grow small groups of wires or even individual wires with large wire-wire distances. In this study, we are able to control the number of nanowires and distance between nanowire arrays by patterning of individual dot on AAO templates. First, we used normal AAO templates with 70 nm diameters and 100 nm interpore distances to grow small groups of nanowires. Second, to fabricate single nanowire arrays, we used Mi-Ha AAO templates with 300 nm interpore distances, 80 nm diameters in mild side and 120 nm diameters in hard side of Mi-Ha AAO (detail structural information of Mi-Ha AAO are in Chapter 4).[27] By e-beam lithography, 300 nm dot arrays were patterned on normal AAO templates. Figures 6.12 and 6.13 show that several nanowires with 40 nm diameters were grown and consist one dot pattern. After e-beam patterning (Figure 6.12a), selected areas exhibit open pore channels, which can be filled with metal nanowires by electrodeposition (Figure 6.12b). Optical micrographs show patterned Ni nanowires in normal AAO templates. Even through PMMA and AAO templates were dissolved, black dot arrays still appeared in Figure 6.12c. In other words, each dot composed with several nanowires and formed the patterned arrays on the substrate and these are stable even after removal of templates.

Especially significant in this work is our ability to grow single wires. When 300 nm dot arrays were patterned on Mi-Ha AAO templates with 300 nm interpore distances, we can produce single nanowire arrays with various diameters using both mild and hard side of Mi-Ha templates. When we patterned mild side of Mi-Ha AAO templates, the opened pore can be filled

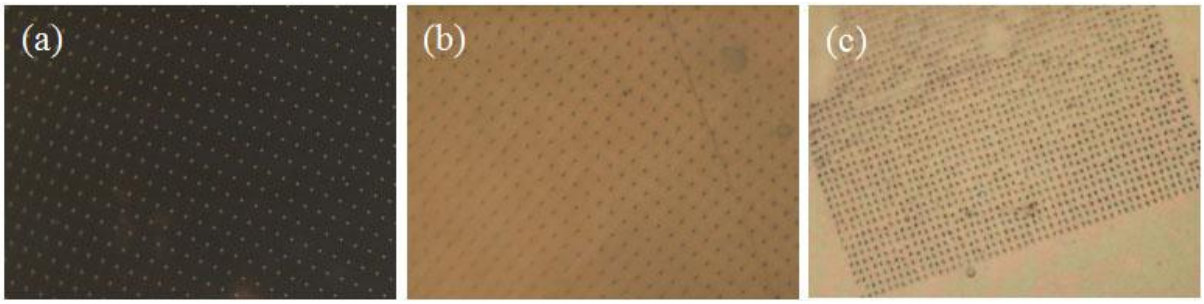

Figure 6.12 Optical micrographs of patterned Ni nanowires synthesized in normal AAO templates; (a) after e-beam patterning, (b) Ni electrodeposition, and (c) removal of PMMA and AAO template.

with 80 nm magnetic nanowires. Magnetic nanowires with 120 nm diameters can be also fabricated by using hard side of Mi-Ha AAO. Figure 6.14a shows optical micrograph after e-beam patterning on PMMA, and FESEM image in Figure 6.14b indicates a single nanowire obtained after removal of templates. In some cases, two wires were grown at the same position as shown in the inset of Figure 6.14b. The interwire distances are about 5 μm. As mentioned above, the interaction between adjacent nanowires can significantly affect their magnetic properties. This synthetic approach allows us to produce and study isolated single nanowires. The magnetic properties of single nanowires with large interwire distances are presented in Figures 6.14c and 6.14d. Hysteresis loops show, as expected, that the single nanowires with small diameter (Figure 6.13c) have more coercivity and larger squareness (M_R/M_S) than the larger ones (Figure 6.14d), where the 80 nm wires exhibit a coercivity of 540 Oe and squareness of 0.58, and the 120 nm wires show a coercivity of 300 Oe and squarness of 0.28.

For the patterning of nanostructures we combined e-beam lithography and template-based electrodeposition. The AAO templates with hexagonally ordered pore structures were employed as a substrate. The selectively opened pore channels were filled with nanowires and produced

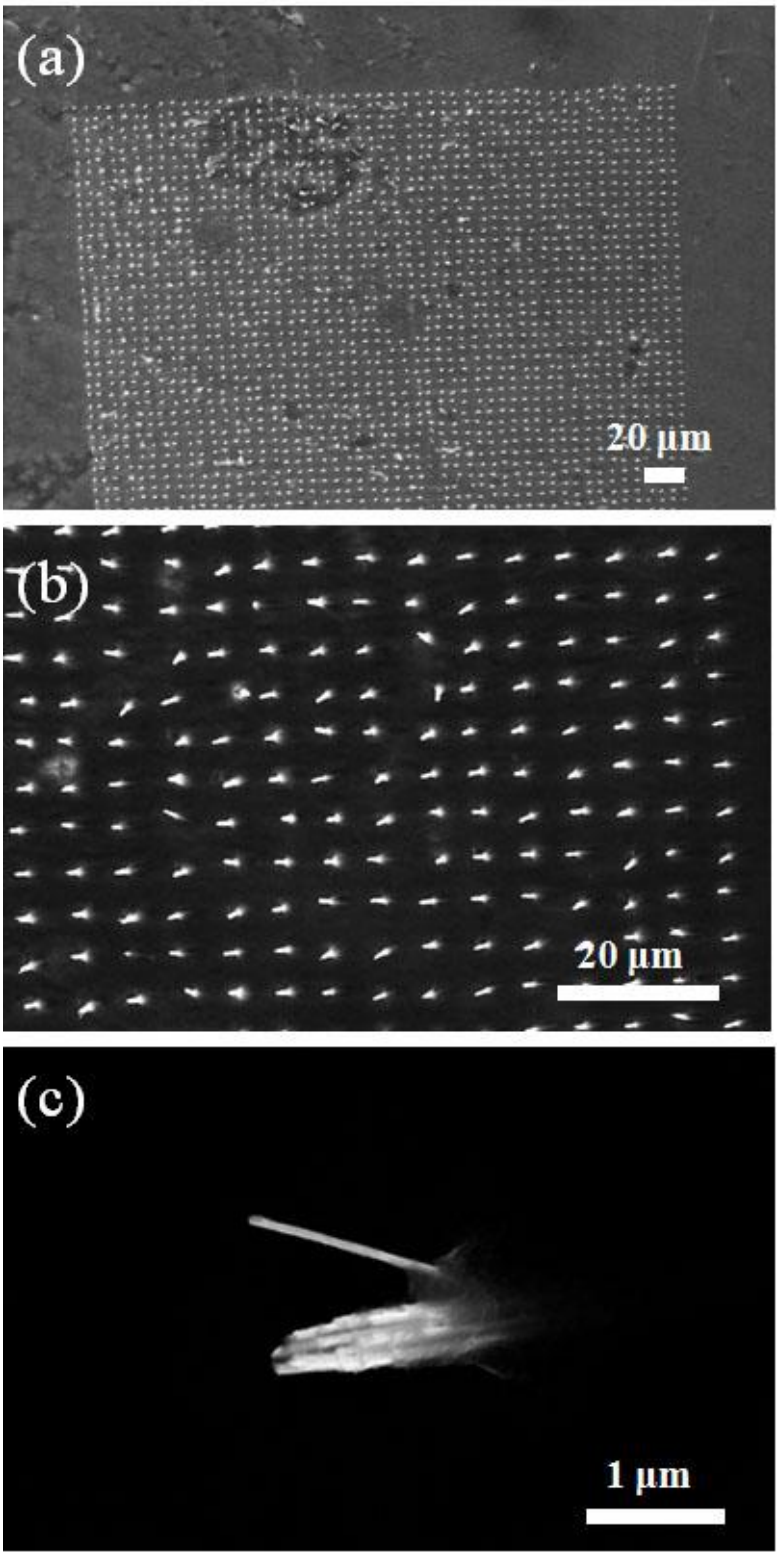

Figure 6.13 (a) FESEM images of patterned Ni nanowires synthesized in normal AAO. (b) High magnification images show that the distance between two patterns is about 7 µm. (c) The diameter and length of nanowires are 70 nm and 2.8 µm, respectively.

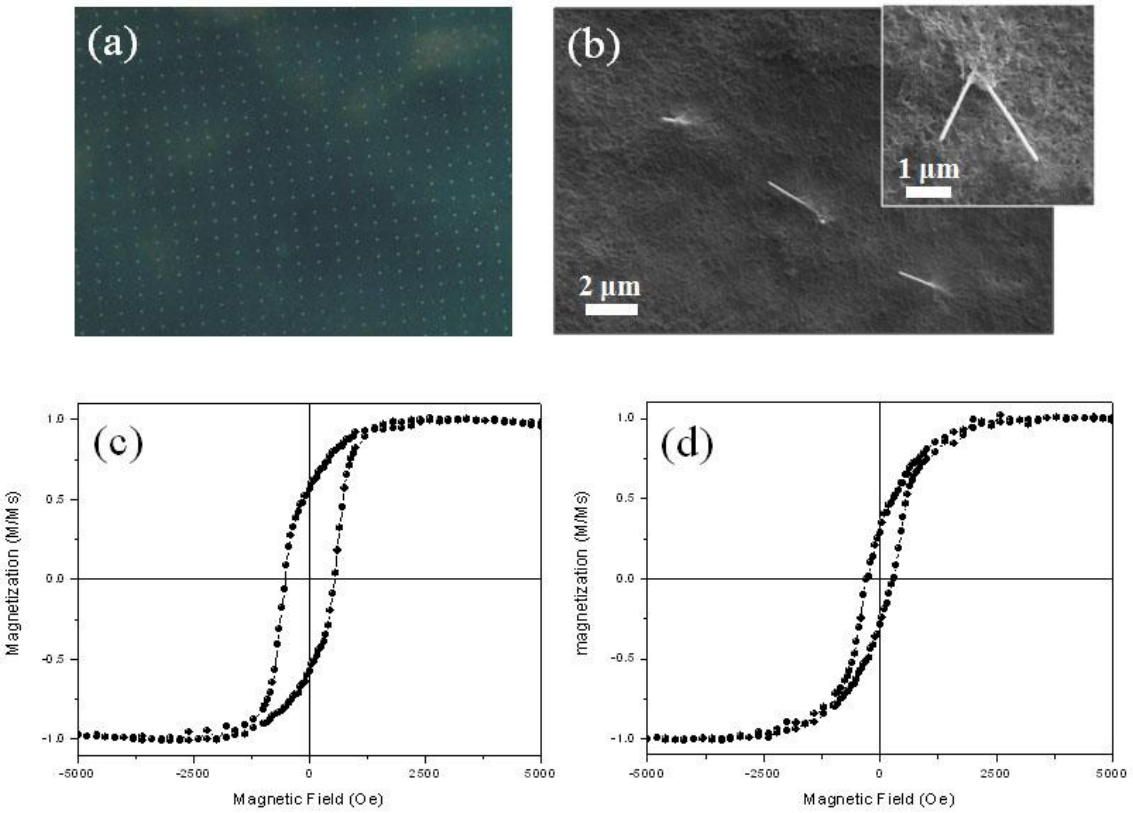

Figure 6.14 (a) Optical micrograph and (b) FESEM images of Ni nanowire arrays patterned on mild side of Mi-Ha AAO templates, where the wire diameter is 80 nm. Inset shows that two Ni nanowires were grown on one patterned position. Room temperature hysteresis loops of patterned Ni nanowires with (c) 80 nm and (d) 120 nm diameters.

patterned nanowire arrays. This approach easily varied the features and sizes of patterned structures and produced patterned nanowire arrays with high aspect ratios that cannot be created by simple lift-off and vapor deposition processes. As we have seen in above the dimensions of patterned structures were reduced from micron to nanometer scale. The smallest patterned nanowire arrays consisted of wires with 80 nm diameters and 2 μm lengths.

As discussed in Chapters 3 and 4, magnetic properties of nanomaterials strongly depend on the anisotropy energy such as magnetocrystalline anisotropy, shape anisotropy and magnetostatic

interaction.[32-34] In general, the anisotropy for the nanowires synthesized in templates is determined mainly by the shape anisotropy, where the magnetic easy axis is parallel to the wire axis, and the magnetostatic coupling between neighboring wires.[34] The magnetocrystalline anisotropy energy is usually much smaller than the shape anisotropy for such systems. In this case, however, the distance between nanowires is 5 μm and patterned nanowires are difficult to interact with each other. Therefore, the shape anisotropy with a magnetic easy axis parallel to the wire axis highly affects their properties. The coercivity and squarness of hysteresis loops increase with increasing aspect ratio as we expected.

6.4 Conclusions

For the patterning of nanowires, we used the lithography techniques, nanosphere lithography and e-beam lithography. Nanosphere lithography is a simple and low cost method compare to other lithographies. Hexagonally assembled PS spheres used as a mask create holes between spheres and the size of the holes is determined by the size and geometry of ordered PS sphere on AAO templates. This method created patterned nanowires arrays, but only one feature is available. By a simple coating process, the top half of PS spheres are covered with metal to produce the unique cup-shaped nanostructures with sizes ranging from micrometer down to several nanometers. We expect the cup-shaped nanostructures can be used for the funtionalization of nanoarchitectures or fabrication of 3D building block.[35-37] In the other lithography approach, e-beam nanolithography was combined with template-based electrodeposition. This is the most powerful technique for the fabrication of new patterned structures with high aspect ratios. We are able to readily vary the features and sizes of patterned structures. By the controlling of pore diameters and interpore distances of AAO templates acting as a substrate, the size and number of patterned nanowires is

also adjustable.

6.5 References

1. H. M. Saavedra, T. J. Mullen, P. Zhang, D. C. Dewey, S. A. Claridge and P. S. Weiss, *Rep. Prog. Phys.*, **2010**, *73*, 036501.
2. E. J. Bae, W. B. Choi, K. S. Jeong, J. U. Chu, G.-S. Park, S. Song and I. K. Yoo, *Adv. Mater.*, **2002**, *12*, 277.
3. D. Bruce Burckel, Joel R. Wendt, Gregory A. Ten Eyck, A. Robert Ellis, Igal Brener, and Michael B. Sinclair, *Adv. Mater.*, **2010**, *22*. 3171.
4. Lorraine Nagle, Declan Ryan, Stephen Cobbe, and Donald Fitzmaurice, *Nano Lett.*, **2003**, *3*, 51.
5. Lee Johnson, and Darren A. Walsh, *J. Mater. Chem.*, **2011**, *21*, 7555.
6. Feng Li, Mo Zhu, Changgeng Liu, Weilie L. Zhou and John B. Wiley, *J. Am. Chem. Soc.*, **2006**, *128*, 13342.
7. Sang Eun Jee, Pyung Soo Lee, Beom-Jin Yoon, Soo-Hwan Jeong, and Kun-Hong Lee, *Chem. Mater.*, **2005**, *17*, 4049.
8. T. Bhuvana, and G. U. Kulkarni, *ACS Nano*, **2008**, *2*, 457.
9. Laurent Vila, Pascal Vincent, Laurence Dauginet-De Pra, Gilles Pirio, Eric Minoux, Laurent Gangloff, Sophie Demoustier-Champagne, Nicolas Sarazin, Etienne Ferain, Roger Legras, Luc Piraux, and Pierre Legagneux, *Nano Lett.*, **2004**, *4*, 521.
10. Jeong-Hyun Cho, and David H. Gracias, *Nano Lett.*, **2009**, *9*, 4049.
11. Young Joon Hong, Hye Seong Jung, Jinkyong Yoo, Yong-Jin Kim, Chul-Ho Lee, Miyong Kim, and Gyu-Chul Yi, *Adv. Mater.*, **2000**, *21*, 222.
12. T. N. Lo, Y. T. Chen, C. W. Chiu, C. J. Liu, S. R. Wu, I. K. Lin, C. I. Su, W. D. Chang, Y. Hwu, B. Y. Shew, C. C. Chiang, J. H. Je and G. Margaritondo, *J. Phys. D: Appl. Phys.*, **2007**, *40*, 3172.
13. W. Xu, J. Wong, C. C. Cheng, R. Johnson and A. Scherer, *J. vac. Sci. Technol. B* **1995**, *13*, 2372.
14. Bodo Fuhrmann, Hartmut S. Leipner, and Hans-Reiner Höche, *Nano Lett.*, **2005**, *5*, 2524.
15. Dirk L. J. Vossen, Joan J. Penninkhor, and Alfons van Blaaderen, *Langmuir*, **2008**, *24*, 5967.
16. A. Kosiorek, W. Kandulski, P. Chudzinski, K. Kempa, and M. Giersig, *Nano Lett.*, **2004**, *4*, 1359.
17. M. Winzer, M. Kleiber, N. Dix and R. Wiesendanger, *Appl. Phys. A* **1996**, *63*, 617.
18. J. Boneberg, F. Burmeister, C. Schäfle and P. Leiderer, *Langmuir*, **1997**, *13*, 7080.
19. S. M. Weeks, F. Y. Oring and W. A. Murray, *Langmuir*, **2004**, *20*, 11208.
20. M. Albrecht, G. Hu, I. L. Guhr, T. C. Ulbrich, J. Boneberg, P. Leiderer and G. Schatz, *Nat. Mater.*, **2005**, *4*, 203.
21. X. Wang, C. J. Summers and Z. L. Wang, *Nano Lett.*, **2004**, *4*, 423.
22. K. H. Park, S. Lee, K. H. Koh, R. Lacerda, K. B. K. Teo and W.I. Milne, *J. Appl. Phys.*, **2005**, *97*, 024311.
23. H. Duan, J. Zhao, Y. Zhang, E. Xie and L. Han, *Nanotechnology*, **2009**, *20*, 135306.
24. S. E. Huq, L. Chen and P. D. Prewett, *Microelectronic Engineering*, **1995**, *27*, 95.

25. T. Hanrath and B. A. Korgel, *J. Nanoengineering and Nanosystems*, **2005**, *218*, 25.
26. K. J. Jeon, J. M. Lee, E. Lee and W. Lee, *Nanotechnology*, **2009**, *20*, 135502.
27. Jin-Hee Lim, Aurelian Rotaru, Seong-Gi Min, Leszek Malkinski, and John B. Wiley, *J. Mater. Chem*., **2010**, *20*, 9246.
28. J.-H. Lim, W.-S. Chae, H.-O. Lee, L. Malkinski, S.-G. Min, J. B. Wiley, J.-H. Jun, S.-K. Ham and J.-S. Jung, *J. Appl. Phys*., **2010**, *107*, 09A334.
29. Alexandru Vlad, Constantin Augustin Dutu, Pierre Guillet, Piotr Jedrasik, Charles-André Fustin, Ulf Södrevall, Jean-Francois Gohy, and Sorin Melinte, *Nano Lett*., **2009**, *9*, 2838.
30. F. Carcenac, L. Malaquin, and C. Vieu, *Microelectronic Engineering*, **2002**, *61-62*, 657.
31. Jeong-Hyun Cho, Anum Azam, and David H. Gracias, *Langmuir*, **2010**, *26*, 16534.
32. J. L. Duvail, S. Dubois, and L. Piraux, A. Vaurés, A. Fert, D. Adam, M. Champagne, F. rousseaus, and D. Decanini, *J. Appl. Phys*., **1998**, *84*, 6359.
33. M. Vázquez, M. Hernández-Vélez, K. Pirota, A. Asenjo, D. Navas, J. Velázquez, P. Vargas, and C. Ramos, *Eur. Phys. J. B* **2004**, *40*, 498.
34. O. C. Trusca, D. Cimpoesu, J.-H. Lim, X. Zhang, J. B. Wiley, A. Diaconu, I. Dumitru, A. Stancu, and L. Spinu, *IEEE Trans. Magn*., **2008**, *44*, 2730.
35. Zhiyong Gu, Hongke Ye, and David H. Gracias, *JOM*, **2005**, *12*, 60.
36. Kwan Skinner, Chris Dwyer, and Sean Washburn, *Nano Lett*., **2006**, *6*, 2758.
37. James A. Sioss, and Christine D. Keating, *Nano Lett*., **2005**, *5*, 1779.

Appendix A

Magnetic Core-Shell Nanowires

In this study, we describe the fabrication and characterization of metal nanotubes and mixed-metal core-shell nanowires in AAO using a two-step electrodeposition. We prepared initially ferromagnetic nanotube structures, and during a second electrodeposition process, ferromagnetic cores were synthesized in the nanotubes.

Core-shell nanowires were grown electrochemically within porous membranes. To create the electrode used in deposition, an alumina membrane (Whatman Corp., average diameter of 200 nm) was sputtered on one side with Ag film (200~300 nm thick). Most of the surface of the Ag film was coated with glue (3M Scotch) to avoid deposition of metal on this part of electrode; a small uncoated region of AAO was fixed to an alligator clip. Electrodeposition was carried out at room temperature by a constant current method in a two-step process on a Princeton Applied Research VMP2. A platinum wire was used as the counter electrode. Plating solutions, Ni (Nickel sulfamate-RTU) and Au (Orotemp 24) plating solution were commercially available from Technics Inc. and Co plating solution was prepared in-house 240 g/L cobalt sulfate hepta-hydrate (99% $CoSO_4 \cdot 7H_2O$, Sigma) and 40 g/L boric acid (99.5% H_3BO_4, Alfa Aesar). Initially nanotubes were grown in one solution by deposition at -0.5 mA for 10 min, then the sample was rinsed three times with distilled water and transferred to the second solution were the core structure was grown, also at -0.5 mA over a 10 min period. The metal nanotubes, which are fabricated by first deposition process, are fully filled by a subsequent deposition step with Au, Co, or Ni, respectively. The AAO containing metal nanostructures are etched slowly with 1.0 M NaOH and washed several times with distilled water resulting in well-aligned nanowires.

A field-emission scanning electron microscopy (FESEM) imaging was obtained on a LEO 1530 VP. EDS was carried out using EDAX GENESIS equipped with JSM 5410 electron microscope. Transmission electron microscopy (TEM) was performed on a JEOL 2010 electron microscope with a 200 kV acceleration voltage. Powder X-ray diffraction (XRD) data were collected on a Phillips X-pert PW 3040 MPD X-ray powder diffractometer with Cu Kα radiation.

Well-aligned metal nanotube and core-shell nanowire arrays are successfully fabricated by a two-step electrodeposition method as illustrated in Figure A.1. The AAO templates used in this study have an average pore diameter of 200 nm. As shown in Figure A.2, Ag film was sputtered onto the top surface of AAO: this also resulted in some silver in the pore channels. Figure A.2a image shown the cross-section view of Ag coated template indicates incompletely closed pore channels. Figure A.2b image also shows the porous Ag film obtained after removal of AAO. The porous Ag film on the AAO templates was worked as catalysts to grow nanotube structures by electrodeposition.

Metal nanotube arrays, which compose the shell part of the core-shell structures, are fabricated by in the first electrodeposition step. We are able to grow both Co and Ni nanotubes by deposition at -0.5 mA for 10 min. FESEM images of metal nanotube arrays show that the synthesized nanostructures are clearly composed of well-aligned nanotubes (Figure A.3). Typically, the metal nanotubes are easily aggregated and bend when the AAO is etched away by a NaOH solution. These nanotubes are around 10 μm length with a 40 nm shell thickness. In addition we are able to control the wall thickness of nanotubes by controlling deposition potential. The Ni nanotubes with shell thickness of 93 nm were synthesized at -0.7 mA in Figure A.3b.

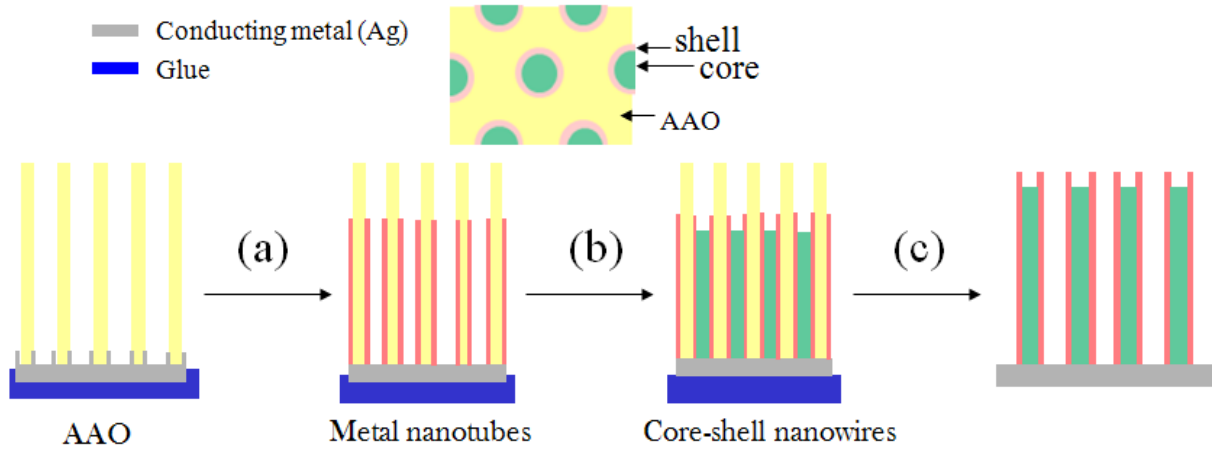

Figure A.1 Schematic diagram for preparation of metal core-shell nanowire arrays; (a) first electrodeposition, (b) second electrodeposition, and (c) removing of AAO templates.

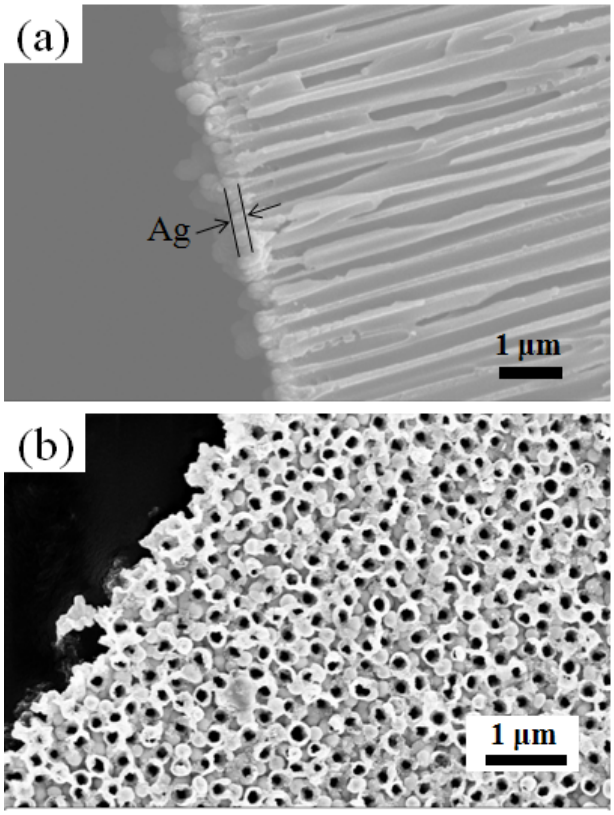

Figure A.2 FESEM images of (a) cross-section view of Ag film on AAO and (b) surface view of Ag film after removal of AAO. The thickness of Ag film is around 200~300 nm.

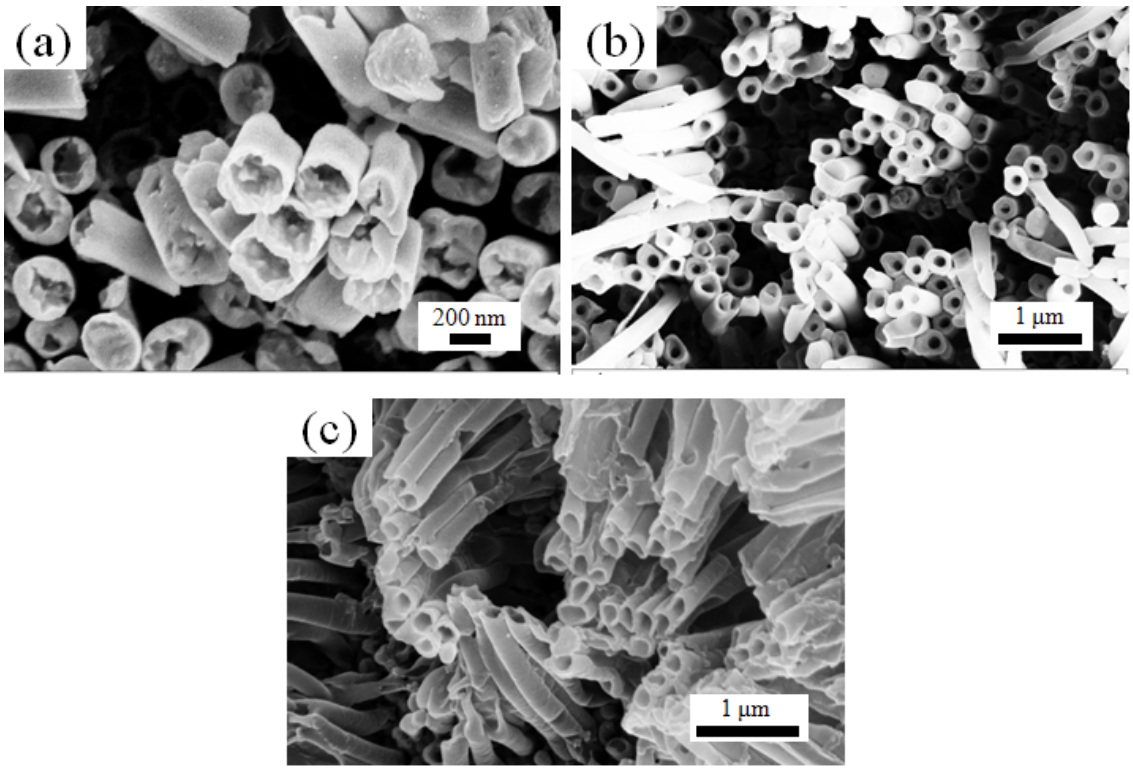

Figure A.3 FESEM images of (a) Ni nanotubes synthesized at -0.5 mA, (b) Ni nanotubes synthesized at -0.7 mA, and (c) Co nanotubes synthesized at -0.5 mA.

The core of the core-shell nanostructures can be produced in the second electrodeposition process using either Co or Ni nanotubes. Figure A.4 shows the core-shell nanowire arrays with an interwire distance of around 400 nm. The diameter of metal shell component maintains its diameter of around 40 nm and the core of the tube is completely filled. Additionally, the length of wires is like that of the corresponding nanotubes (ca. 10 µm).

Energy-dispersive spectrometry (EDS) was used for elemental analysis of both nanotubes and core-shell nanowires after removal of AAO (Figure A.5). Figures A.5a and A.5b were measured from those nanotubes shown in Figure A.1.3; EDS clearly shows both Co and Ni peaks. Also, NiCo and CoNi core-shell nanowires contained both Ni and Co peaks (Figures A.5c and A.5d).

Ag peaks result from the conducting metal under the nanostructures.

Electrochemically grown Co and Ni nanowires generally have hcp and fcc structures, respectively. The strong peaks in Figure A.6a, for NiCo core-shell nanowires, are detected at $2\theta \approx 42°$ and 76° corresponding to the Ni (111) and (002). Also, the core-shell nanowires are showing Co peaks and intensity of peaks depends on which material is composing the core part of core-shell nanowires. In our experiments, Co and Ni nanotubes do show the hcp and fcc structures, as evidenced by the XRD data in Figures A.6b and A.6c.

For the TEM measurement, the nanostructures dispersed in a NaOH solution during removal of AAO was collected by magnet, and then was re-dispersed into ethanol. A droplet of ethanol containing metal nanostructures was placed onto a copper grid and the solvent was evaporated prior to microscopy. Figures A.7a and A.7b clearly show that the core-part of core-shell nanowires was fully filled during second electrodeposition. The selected area electron diffraction (SAED) pattern in Figure A.7c shows that the core-shell nanowires are composed with a polycrystalline structure. The fact that the wires are polycrystalline may be related to the wider diameter of the pores or the electrodeposition process.

The nanotubes were synthesized with Co and Ni and the cores were Co, Ni and Au. Core-shell nanostructures can also be grown with other materials like nonmagnetic, soft or hard magnetic materials. It should be possible to expand this approach to the growth of core-shell structures with other materials such as semiconductors or conducting polymers for potential applications in electronics, magnetics, biological systems, or sensor materials. We still need more studies in magnetic properties of core-shell nanostructures.

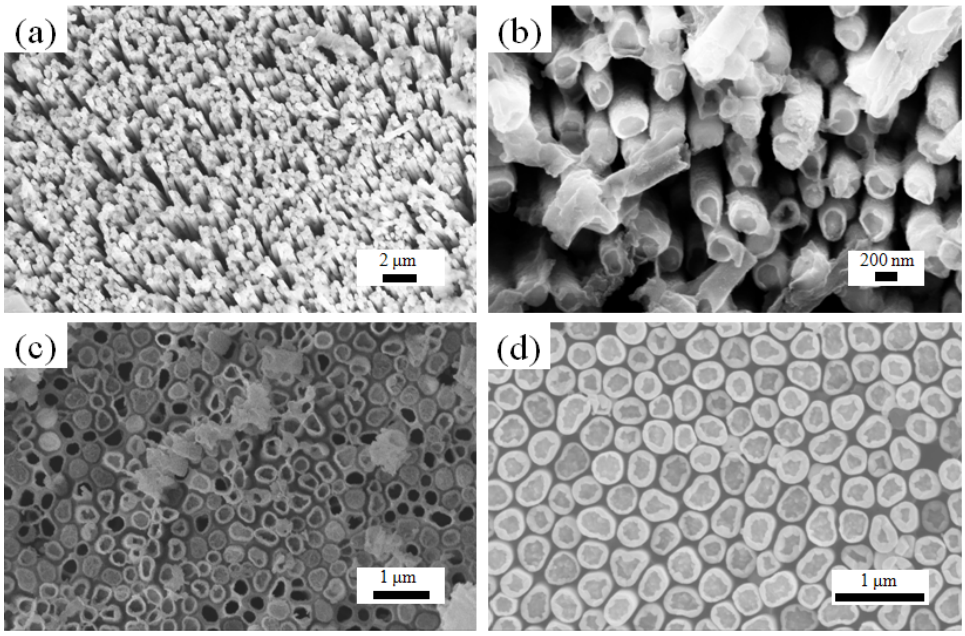

Figure A.4 FESEM images of (a, b) NiCo, (c) CoNi, and (d) AuNi core-shell nanowire arrays.

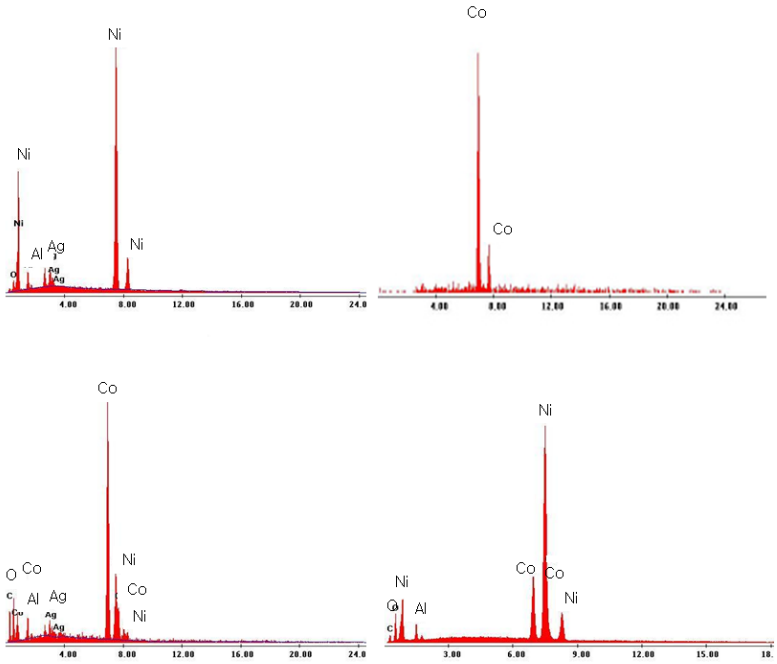

Figure A.5 EDS of (a) Ni nanotube, (b) Co nanotube, (c) CoNi, and (d) NiCo core-shell nanowire after removal of the AAO.

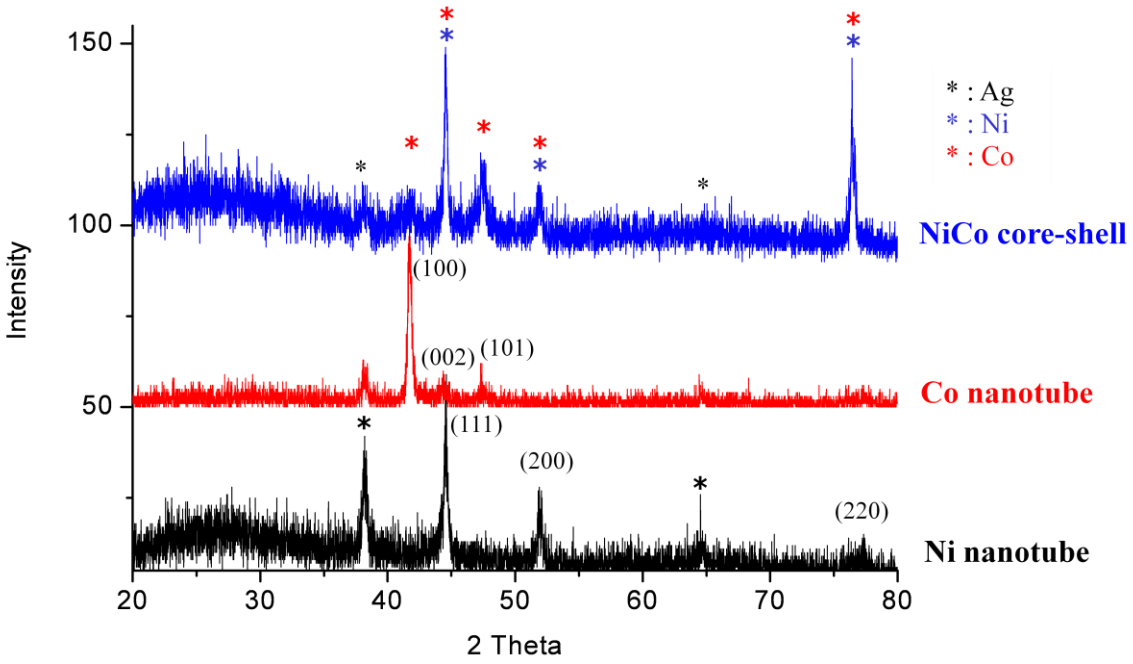

Figure A.6 XRD results of (a) NiCo core-shell nanowires, (b) Co nanotubes, and (c) Ni nanotubes (Ag from conducting film on bottom of AAO template).

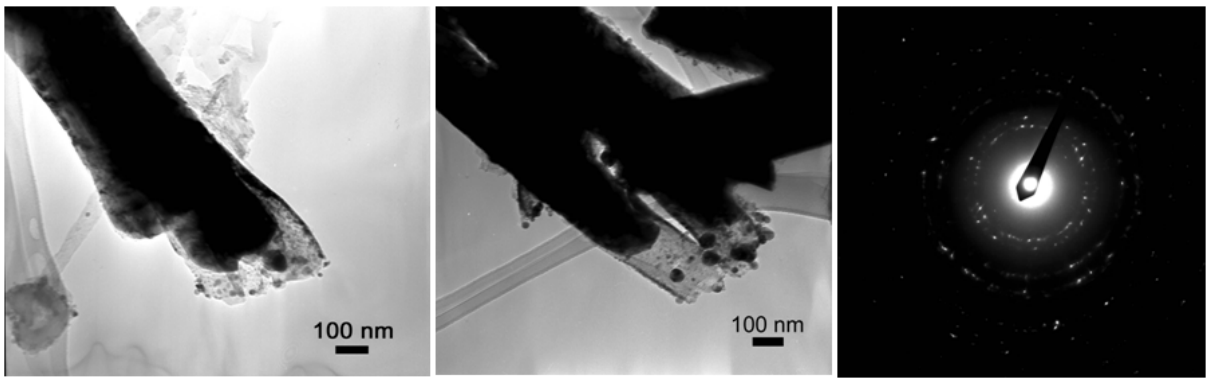

Figure A.7 TEM images and SAED pattern of NiCo core-shell nanowires.

Appendix B

Anodization of Sn Film

We discuss the synthesis of porous tin oxide nanostructures by an anodization using a $H_2C_2O_4$ solution that is comparably less toxic than that fluoride containing electrolytes. The morphology and surface area were controlled by changing concentration of electrolytes.

Plate-like oxide layers were also synthesized in a mixture solution of ethylene glycol-0.3 M H_2SO_4. For fabrication of porous SnO_2, Sn films were anodized in 0.3 M, 0.1 M and 0.05 M $H_2C_2O_4$ at constant current 90 mA. Because the synthesized metal oxide is SnO, we heated SnO in air at 500 ℃ for 3 h to form SnO_2 nanostructures. Carbon bars were used as a counter electrode and vigorously stirred during anodization.

A field-emission scanning electron microscope (FESEM) imaging was obtained on a LEO 1530 VP. Transmission electron microscopy (TEM) was performed on a JEOL 2010 electron microscope with a 200 kV acceleration voltage. Powder X-ray diffraction (XRD) data were collected on a Phillips X-pert PW 3040 MPD X-ray powder diffractometer with Cu Kα radiation. ASAP 2020 surface area and porosity analyzer was used for characterization of Brunauer-Emmett-Teller (BET) surface area of porous nanomaterials.

Figure B.1 images show plate-like pieces of SnO after anodization of Sn film in a mixture solution of ethylene glycol and 0.3 M H_2SO_4 at 93 mA for 1 h. It shows an oxide film without an ordered pore structure; only a few pores were observed, but it was not opened from top to bottom.

When the Sn film was anodized in $H_2C_2O_4$ at constant current 90 mA for 1 h, porous structures were achieved as shown in Figure B.2. The pore size of oxide nanostructures is about 30~80 nm

and the wall thickness is about 5 nm. As-synthesized tin oxide showed black color and is easily separated from the Sn film. The SnO was collected for characterization of its BET surface area. The surface area of SnO was 51.5091 m^2/g. As shown in Figure B.2, the oxide layers formed as layer structures, unlike those Al_2O_3 and TiO_2 membranes that are also synthesized by anodization. The oxide layer was randomly oriented and separated from Sn film so that barrier layers were found middle of the oxide layers; black arrows in Figure B.2b indicate the barrier layers. TEM images of SnO layer show porous structures (Figure B.3a and B.3b) and high resolution TEM (HRTEM) image shows the lattice fringe of 0.27 nm corresponds to the (110) plane of SnO. EDS also proved this material consists of Sn and O. XRD peak shows structural information of SnO (Romarchite, space group: P4/nmm) with (110), (002) and (102) directions at 33°, 37°, and 44°, respectively.

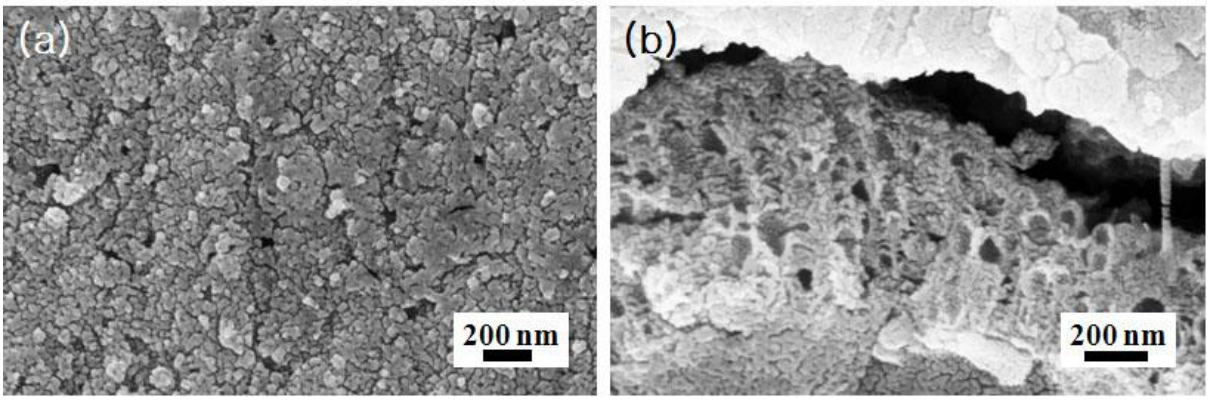

Figure B.1 FESEM images of (a) top surface view and (b) cross-section view of plate-like SnO.

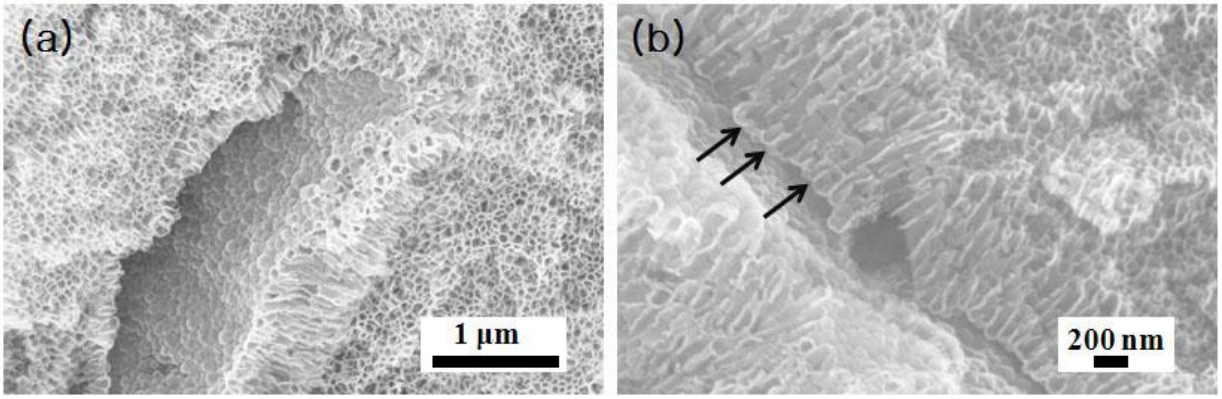

Figure B.2 FESEM images of porous SnO synthesized in 0.3 M $H_2C_2O_4$; (a) low and (b) high magnification.

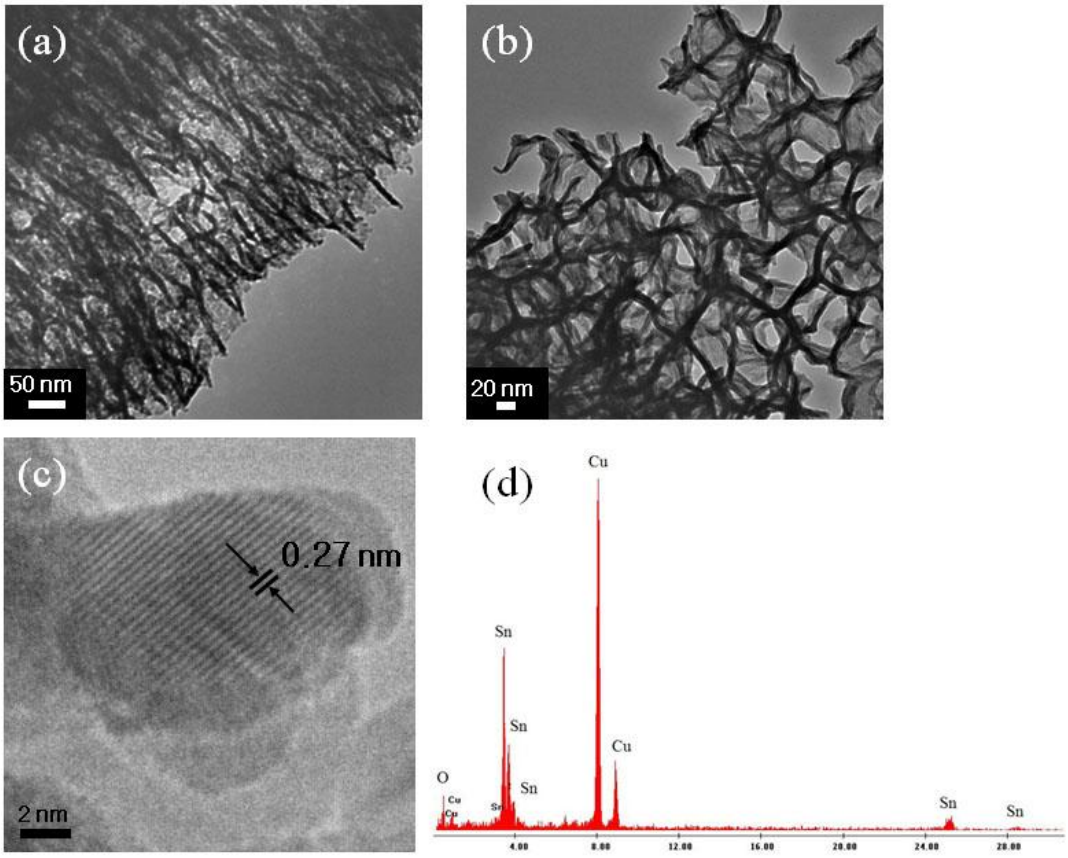

Figure B.3 (a and b) TEM images and (c) HRTEM images of porous SnO nanostructures. (d) EDS peaks of porous SnO nanostructures. Cu peaks are from TEM grid.

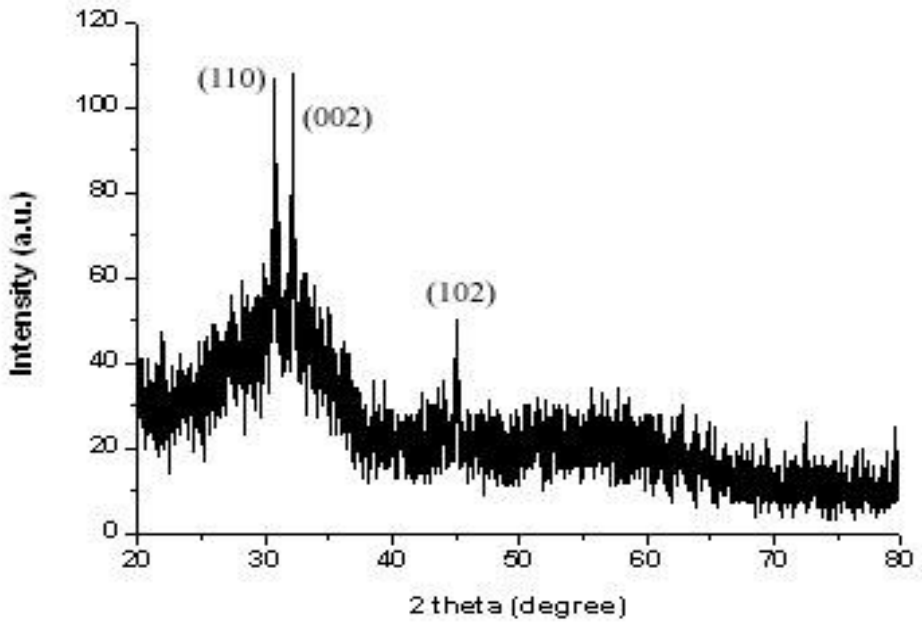

Figure B.4 XRD pattern of porous SnO nanostructures synthesized by anodization of Sn using 0.3 M $H_2C_2O_4$.

SnO_2 nanostructures could be obtained after heat treatments in air at 500 ℃ for 3h. The color of nanomaterials was changed from black to white. Figure B.5 shows the FESEM images of porous SnO_2 nanostructures. Most of the pore walls were broken into several pieces and formed chain structures as shown in TEM images (Figure B.5c). As a result, the BET surface area of SnO_2 was increased to 62.0138 m^2/g. The lattice fringe of 0.34 nm corresponds to the (110) plane of SnO_2 (see Figure B.5d). XRD peak in Figure B.6 indicates that it is SnO_2 with the cassiterite structure (space group: P42/mnm).

We also tried to change the pore size and surface area of nanostructures by changing concentration of electrolytes. Sn films were anodized in a 0.1 M $H_2C_2O_4$ solution at 90 mA and the morphology was examined by FESEM and TEM as shown in Figure B.8. The pore size was

50~75 nm and the wall thickness was increased a little to 10 nm. The surface area of SnO_2 was reduced to 37.1650 m^2/g compare to the SnO_2 nanostructures that synthesized in 0.3 M $H_2C_2O_4$. We expect the growth rate of oxide layers will be similar to the anodization in 0.3 M $H_2C_2O_4$ because of the same applied current 90 mA, but the etching ratio will be different due to the concentration of acid solutions. After heat treatments of porous SnO synthesized in 0.1 M $H_2C_2O_4$, porous SnO_2 nanostructures were obtained in Figures B.7c and B.7d. However, the oxide layer with 700 nm length was stacked and built the porous structures. As a result the porous SnO_2 nanostructures were easily separated from the substrate.

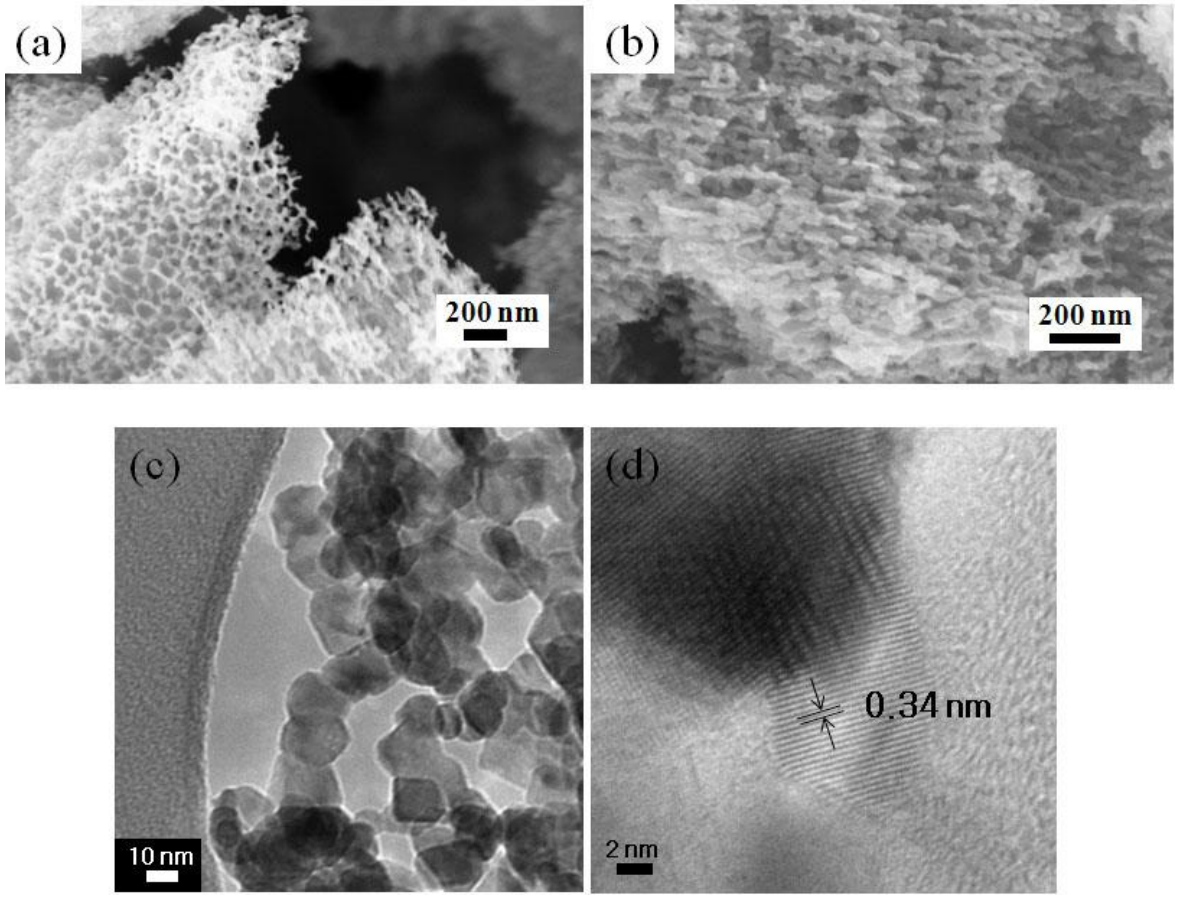

Figure B.5 FESEM images of (a) top and (b) cross-section view of SnO_2 nanostructures. (c) TEM and (d) HRTEM images of SnO_2 nanostructures, where the samples are prepared after heat treatments of SnO in Figure B.2.

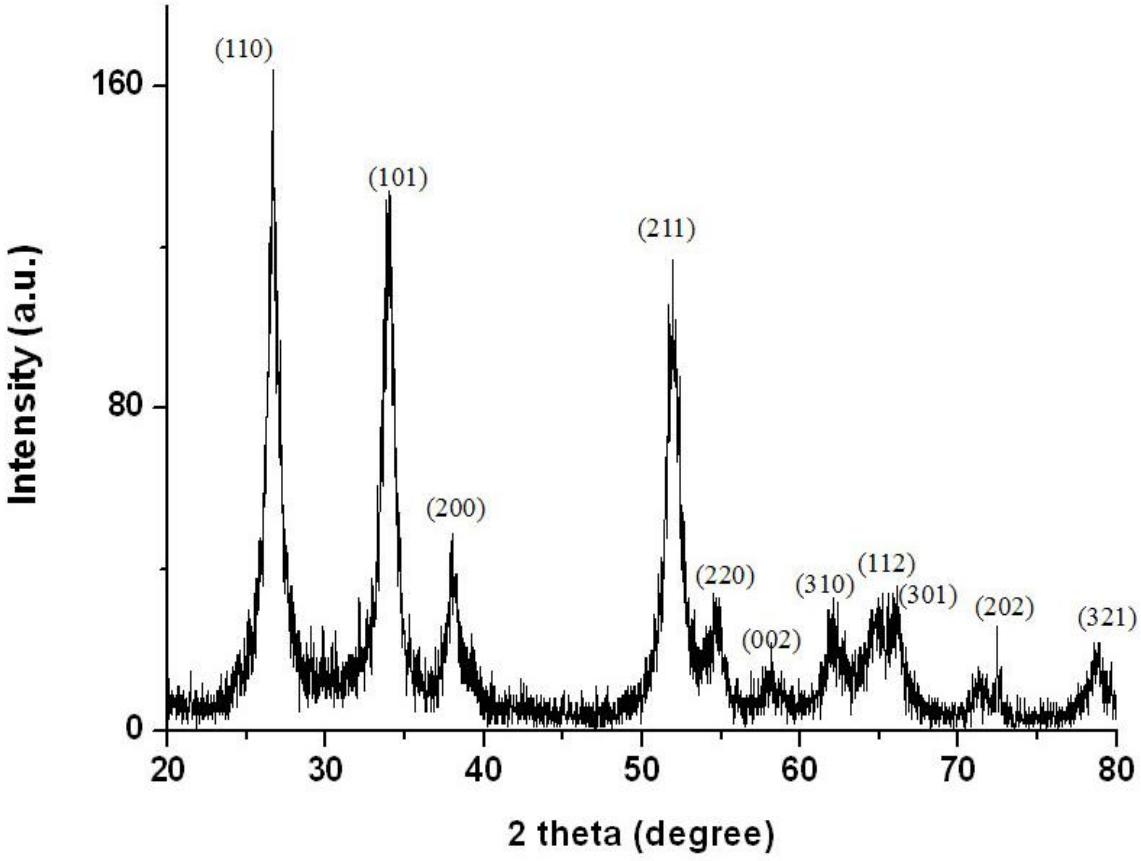

Figure B.6 XRD result of SnO_2 nanostructures obtained from the sample in Figure B.5.

When Sn film was anodized in 0.05 M $H_2C_2O_4$, the pore diameter was reduced in the range of 15~25 nm and the wall thickness was increased to 20 nm, approximately two times compared to SnO that fabricated in 0.1 M $H_2C_2O_4$. As-synthesized oxide materials were changed their color from black to white after several hours in air without heating. Samples were very sensitive to water and oxygen in air and became porous SnO_2. FESEM images in Figure B.8 show their top and cross-section view and the layered structures are stable on the substrate. XRD pattern indicates that the SnO layers were transformed to cassiterite, SnO_2 (Figure B.8c).

Porous tin oxide nanomaterials were synthesized by anodization of Sn film at constant current 90 mA in $H_2C_2O_4$. By TEM and XRD measurements, we knew that as-synthesized porous oxide layers were SnO and it was transformed to SnO_2 after heat treatments at 500 ℃. However, during the heat treatments, pore structures of SnO synthesized in 0.3 M and 0.1 M $H_2C_2O_4$ were destroyed. Porous SnO layers produced in 0.05 M $H_2C_2O_4$ was transformed to SnO_2 in air without any heat treatments. The pore diameters and wall thicknesses were controllable by changing the concentration of electrolytes. The surface area was also reduced by increasing wall thickness of porous oxide layers. We expect porous SnO_2 nanostructures can be used for applications in gas sensors, optical devices, and lithium secondary batteries.

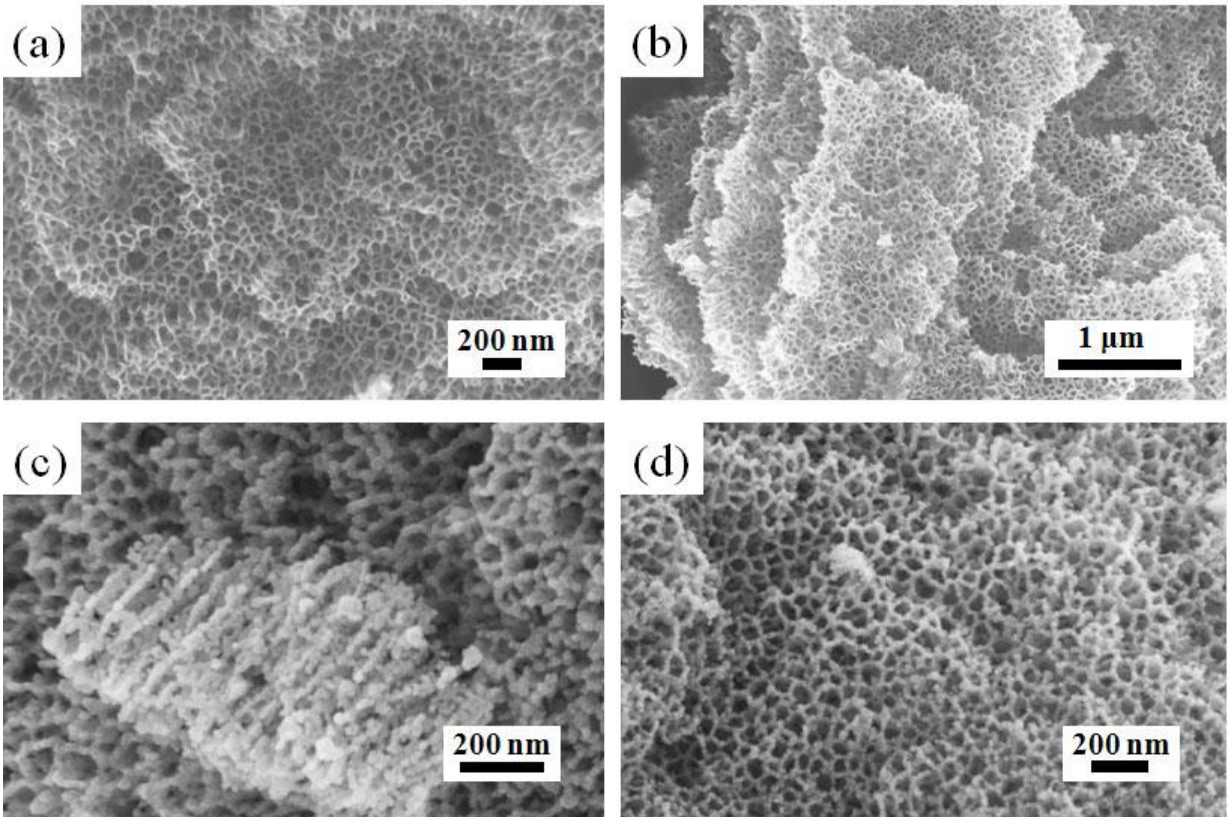

Figure B.7 FESEM images of (a and b) SnO and (c and d) SnO_2 nanostructures synthesized by anodization in 0.1 M $H_2C_2O_4$.

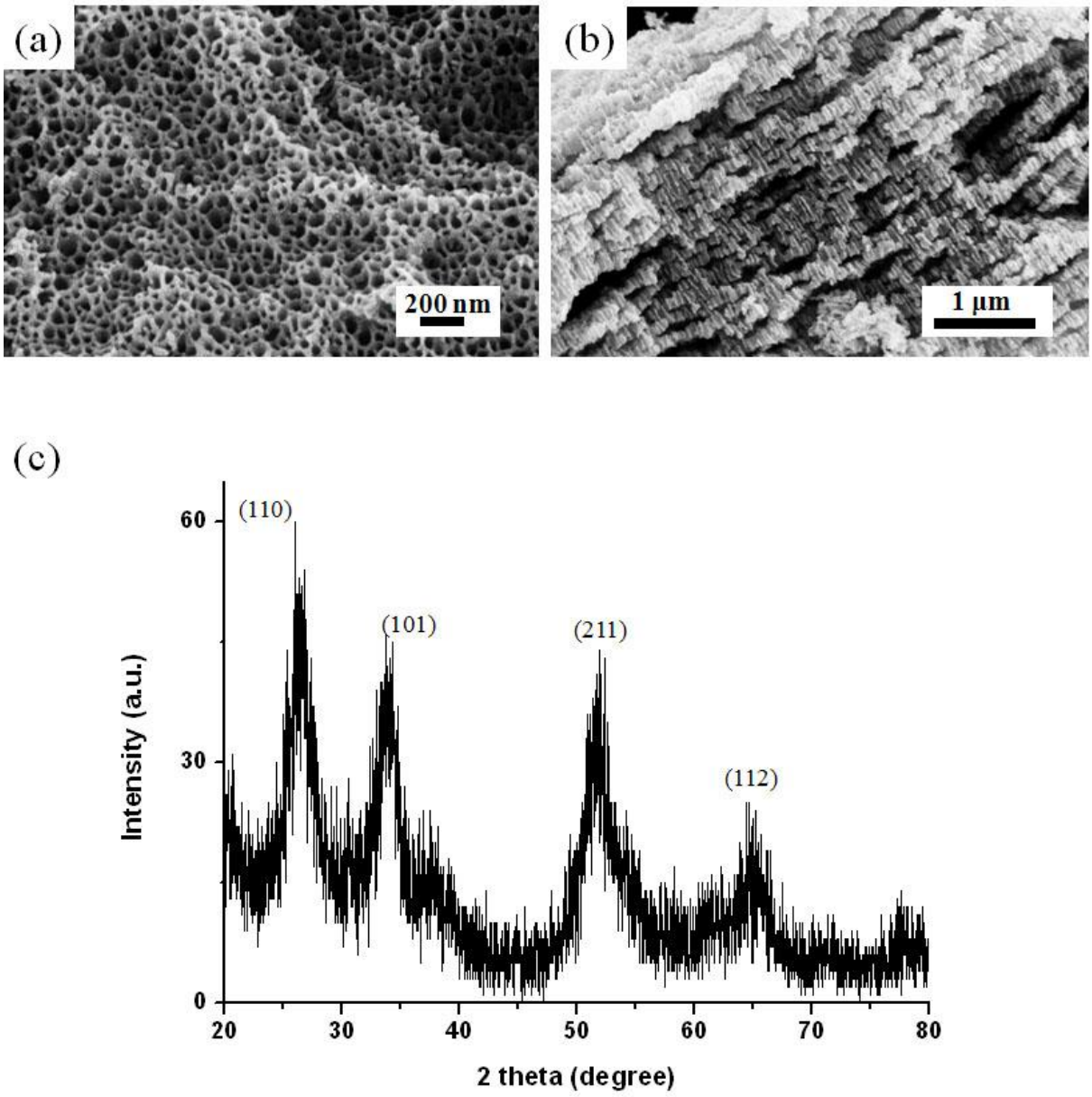

Figure B.8 (a and b) FESEM images and (c) XRD result of SnO_2 nanostructures synthesized by anodization in 0.05 M $H_2C_2O_4$, where the oxide layers were not heated at 500 ℃. SnO synthesized in 0.05 M $H_2C_2O_4$ very quickly reacted with water and oxygen in air to produce the mineral cassiterite, SnO_2.

Vita

Jin-Hee Lim was born in Pyeongchang, South Korea, in November, 1982. After completing high school in February, 2001, she went to the Department of Chemistry at Kangnung National University. She joined Dr. Jin-Seung Jung's group in December, 2002 and she was interested in inorganic porous materials and Materials Chemistry. After she obtained her Bachelor of Science degree in August, 2004, she started her Master's degree in Jin-Seung Jung's group. She studied not only porous materials and template-based electrodeposition, but also magnetic nanostructures, including nanoparticles and nanowires. She got her Master's degree in August, 2006. At the same time she had a chance to come the University of New Orleans as a visiting student; she worked in Dr. Wiley's nanomaterials group on several materials. In September, 2007, she started a Doctoral degree at UNO. Her research has focused on the synthesis and characterization of magnetic nanomaterials including nanocrystals, nanorods, nanotubes, nanowires, and patterned nanomaterials obtained by template-based electrodeposition methods.